MODELLING THE DYNAMICS OF THE ANTARCTIC SLOPE FRONT

by

Wilma Gertrud Charlotte Huneke
M.Sc., B.Sc.

Submitted in fulfilment of the requirements
for the Degree of Doctor of Philosophy

Institute for Marine and Antarctic Studies
Antarctic Gateway Partnership
University of Tasmania
November 2019

This thesis contains no material which has been accepted for a degree or diploma by the University or any other institution, except by way of background information and duly acknowledged in the thesis, and to the best of my knowledge and belief no material previously published or written by another person except where due acknowledgement is made in the text of the thesis, nor does the thesis contain any material that infringes copyright.

Signed: 

Wilma Gertrud Charlotte Huneke

Date: November 19, 2019

Signed: 

Wilma Gertrud Charlotte Huneke

Date: November 19, 2019

STATEMENT ON CO-AUTHORSHIP

The following people and institutions contributed to the publication of work undertaken as part of this thesis.

Paper 1 / Chapter 2: Deep bottom mixed layer drives intrinsic variability of the Antarctic Slope Front:

- Wilma Gertrud Charlotte Huneke, Candidate, University of Tasmania (80%)
- Andreas Klocker, Supervisor, University of Tasmania (10%)
- Benjamin Keith Galton-Fenzi, Supervisor, Australian Antarctic Division (10%)

Details of authors roles:

Andreas Klocker contributed with project development and refinement, conceptual aspects, and manuscript preparation.

Benjamin Keith Galton-Fenzi contributed with concept development, technical aspects and manuscript development.

We, the undersigned, agree with the above stated "proportion of work undertaken" for the above published and peer-reviewed manuscript contributing to this thesis:

Signed: _____

Dr. Andreas Klocker
Supervisor
University of Tasmania
Institute for Marine and Antarctic Studies
Date: November 19, 2019

Signed: _____

Prof. Neil Holbrook
Head of centre, Oceans & Cryosphere
University of Tasmania
Institute for Marine and Antarctic Studies
Date: November 19, 2019

ABSTRACT

This thesis investigates the dynamics of the Antarctic Slope Front (ASF), which controls heat exchange across the Antarctic continental slope. The motivation comes from the need to advance the understanding of oceanic heat supply to the Antarctic ice shelf cavities which impacts the stability of the Antarctic Ice Sheet. To address this question, the ocean dynamics at the Antarctic continental shelf break system is explored using the Regional Ocean Modeling System (ROMS) which has been adapted for ocean/ice shelf interactions. The ASF is examined in two different model configurations, in an idealised channel domain and in a realistic circumpolar domain, with a focus on the sensitivity to surface forcing to understand how the ASF may change in a future climate.

Firstly, an idealised model configuration of the Antarctic continental shelf break system in a zonally-symmetric periodic domain is developed. An intrinsic variability of the ASF that is driven by a deep bottom mixed layer is discussed in the case of a relatively fresh continental shelf. Secondly, the role of surface buoyancy forcing and wind for the strength and shape of the ASF is investigated by analysing sensitivity experiments using the idealised domain. Different frontal regimes and their thresholds are determined on the basis of the relative ratio between buoyancy forcing to mechanical forcing.

Thirdly, perturbation experiments with artificially increased basal freshwater are performed in a realistic circumpolar domain. This work is motivated by the projected increase in freshwater supply to the ocean due to basal melting in a warmer climate. The response to the additional freshwater in the perturbed simulations is overall non-local. Findings between the idealised and realistic model agree in that the transport along the Antarctic continental slope increases for fresher continental shelves.

ACKNOWLEDGEMENTS

This thesis was supported under the Australian Research Council's Special Research Initiative for Antarctic Gateway Partnership (Project ID SR140300001), and the Australian Research Council Centre of Excellence for Climate System Science, University of Tasmania. This research was undertaken with the assistance of resources and services from the National Computational Infrastructure (NCI), which is supported by the Australian Government.

I would like to express my gratitude to my supervisors Andreas Klocker and Benjamin Galton-Fenzi, who introduced me to the world of ocean modelling, for their support and guidance. I also thank Kaitlin Naughten for her support in setting up MetROMS-iceshelf that is used in Chapter 4. In no particular order I thank Andrew Stewart, Eva Cougnon, David Munday, Madelaine Gamble-Rosevear, Lenneke Jong, Hannes Hollmann and Svenja Ryan for useful discussions and editorial assistance.

TABLE OF CONTENTS

TABLE OF CONTENTS

LIST OF TABLES

LIST OF FIGURES

LIST OF FIGURES

LIST OF ACRONYMS

AABW Antarctic Bottom Water

ACC Antarctic Circumpolar Current

ACoC Antarctic Coastal Current

APE Available Potential Energy

ASC Antarctic Slope Current

ASF Antarctic Slope Front

CDW Circumpolar Deep Water

CICE Community Ice CodE

CPP C-Pre-Processor

DSW Dense Shelf Water

EKE Eddy Kinetic Energy

HC Heat Content

HT Heat Transport

KPP K-Profile Parameterisation

MKE Mean Kinetic Energy

PV Potential Vorticity

ROMS Regional Ocean Modelling System

LIST OF FIGURES

MCT Model Coupling Toolkit

NOAA National Oceanic and Atmospheric Administration

NSIDC National Snow and Ice Data Center

Chapter 1

Introduction

The increase of global mean sea level is one of the most threatening repercussion of climate change for humans. The two driving factors for the rise are thermal expansion due to the uptake of excess atmospheric heat (thermosteric effect), and an increase of the total ocean volume, mainly due to land ice discharge (eustatic effect). The largest land ice volumes on Earth are stored in the Greenland and Antarctic ice sheets with an equivalent of 7 m and 58 m of sea level rise, respectively (Dowdeswell, 2006; Fretwell et al., 2013). Thus, their potential to change the global mean sea level is enormous, even if only a small proportion of these freshwater reservoirs enters the ocean.

While current global sea level rise is largely caused by the thermosteric effect, the increasing negative mass balance of the large ice sheets will dominate in the centuries to come (Church et al., 2013; Rignot et al., 2019). Predictions of the exact contribution – from the Antarctic ice sheet in particular – are accompanied with large uncertainties. Most of today's Antarctic research is therefore driven by the quest for improved estimates of Antarctic mass loss and reduced uncertainties. This thesis contributes to this overall goal by investigating the dynamics of the Antarctic Slope Front (ASF).

1.1 Basal melting of Antarctic ice shelves

The ocean, with its enormous heat content, is a key player in controlling the stability of the Antarctic ice sheet. The Antarctic mass balance is set by mass gain from snow accumulation on land, and by mass loss from iceberg calving and melting. Melting occurs predominantly at the ocean-ice interface of the

numerous, with seawater filled ice shelf cavities as opposed to at the surface of the ice, where melting is negligible. Antarctica's mass balance is negative (Rignot et al., 2019) where basal melting and iceberg calving contribute each about 50 % to the total mass loss (Figure 1.1) with an increasing contribution from basal melting (Rignot et al., 2013; Paolo et al., 2015).

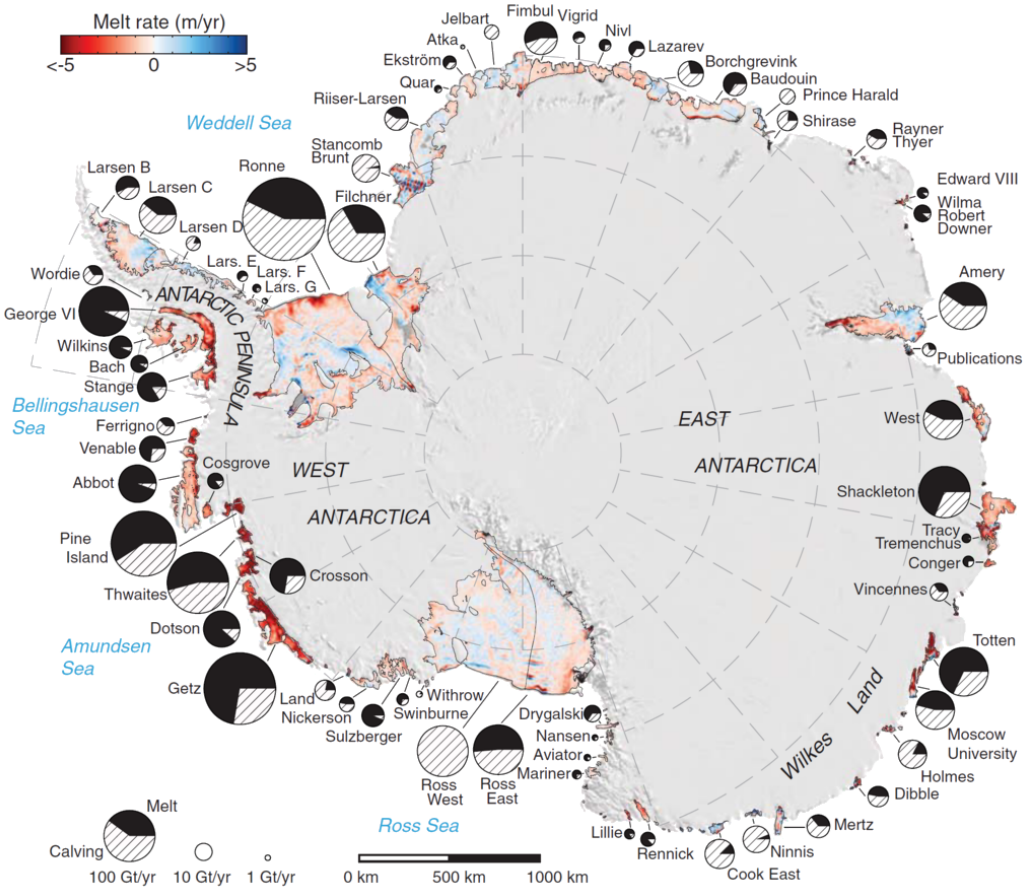

Figure 1.1: Map of Antarctic ice shelves taken from Rignot et al. (2013). Shading indicates the amount of melting and circles indicate the relative partitioning of total mass loss between melting (filled) and calving (dashed) for each ice shelf.

The melting of ice shelves does not directly affect global sea level as they are already afloat. However, ice shelves control the flow speed of the grounded ice upstream by providing a back stress in a process known as buttressing. The thinning or retreat of an ice shelf reduces the stress and leads to an acceleration of the ice discharge towards the ocean (Dupont and Al-

ley, 2005). Observational evidence of this relationship exists from the Pine Island, Thwaites, Haynes, Smith, and Kohler glaciers in West Antarctica (Rignot et al., 2014). The volume of ice draining through an ice shelf depends on the size of the catchment behind it. A few key ice shelves drain significant portions of the ice sheet. If the ice sheet is additionally susceptible to the marine ice sheet instability[1], an initial retreat of the ice shelf could lead to substantial contributions to global sea level. The Totten Glacier Ice Shelf alone, which is the main outlet of the Aurora Subglacial Basin, East Antarctica, drains a volume equivalent to 3.5 m sea level rise (Greenbaum et al., 2015) making it a striking example of the important role that ice shelves play in the stability of the grounded ice and ultimately in global sea level.

Based on their melt pattern, Antarctic ice shelves can be classified into three different modes of melting (Jacobs et al., 1992) which are schematically shown in Figure 1.2. The crucial factor distinguishing these modes is the water mass that primarily occupies the cavity.

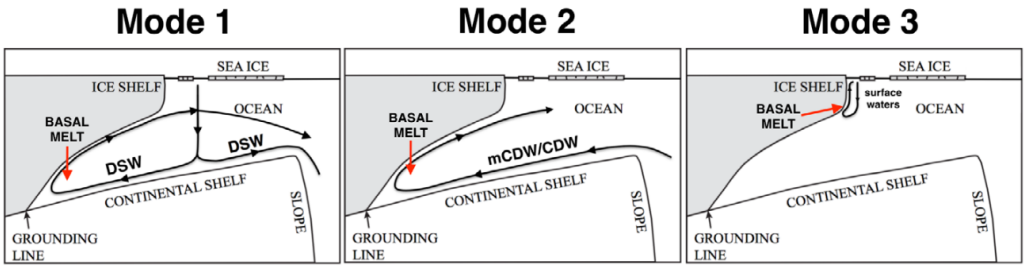

Figure 1.2: Schematic from Silvano et al. (2016) showing different modes of melting. See text for an explanation.

Mode 1: Cold ice shelves. The ice shelf cavity is filled with Dense Shelf Water (DSW) that has a temperature close to the surface freezing point at approximately -1.9°C. Melt rates are low in this mode, but due to the pressure dependence of the in situ freezing point (Millero, 1978), water at

[1]Marine ice sheet instability describes a positive feedback mechanism to basal melting for ice that is grounded on a retrograde bedrock slope (e.g., Weertman, 1974; Schoof, 2007). An initial retreat of the ice shelf exposes more glacial ice to sea water at depth. This results in further melting due to the pressure dependence of the freezing point.

surface freezing point can exceed the local freezing point at depth by a few degrees and drive basal melting. Deep ice shelves are hence susceptible to higher melt rates with strongest melting near the grounding line, the point where the grounded ice starts to float. The largest ice shelves, namely the Ross Ice Shelf, the Filchner-Ronne Ice Shelf, as well as the Amery Ice Shelf are cold ice shelves, but smaller ice shelves along the East Antarctic coastline can also be classified as mode 1 ice shelves.

Mode 2: Warm ice shelves. Warm ice shelves show the largest melt rates (Rignot et al., 2019). The ice shelf cavity is filled with relatively warm (0°C) modified Circumpolar Deep Water (CDW). On the continental shelf, modified CDW usually resides at depth. This raises the potential of the ocean to melt the base of the ice shelf, as has been described in mode 1, even more. Prominent examples for warm ice shelves are the Pine Island, Thwaites and Kohler/Smith Glaciers in West Antarctica as well as the Totten Ice Shelf in East Antarctica.

Mode 3: Shallow melting. This mode of melting is mainly limited to late summer and only affects the shallower, frontal part of an ice shelf. Melting occurs due to warmed surface water that is pushed under the ice shelf by Ekman dynamics[2]. Strong tidal mixing can also enhance melting near the ice shelf front. Elevated near-ice front melting can theoretically occur at any ice shelf, and was first observed under the Fimbul Ice Shelf in the eastern Weddell Sea (Hattermann et al., 2012).

The above classification illustrates that oceanic conditions around the Antarctic coastline vary substantially. This is because, while ocean-atmosphere and ocean-ice interactions lead to cooling of the ocean almost year-round, the circulation at the shelf break, which controls the oceanic heat supply, varies along the Antarctic coast.

[2]Ekman dynamics describe the transport of water in the surface/bottom boundary layer due to friction in the presence of the Coriolis force (e.g. Cushman-Roisin and Beckers, 2011, chapter 8). In the Southern Hemisphere, the net transport in the surface Ekman layer is oriented 90° to the left compared to the direction of the surface stress (wind). Convergence or divergence of the horizontal flow may lead to vertical velocities (upwelling or downwelling), also known as Ekman pumping.

1.2 Continental shelf circulation

The feature that sets the Southern Ocean apart from other world oceans is its circumpolar extent due to the lack of zonal boundaries between Antarctica and other continents. As a consequence, the prevailing Westerlies set up the eastward flowing Antarctic Circumpolar Current (ACC). The ACC region is characterised by isopycnals that shoal to the south as a consequence of Ekman divergence with stronger Westerlies to the north. The upwelled water is upper CDW, a salty, but relatively warm water mass, residing at mid depth of the ACC. The rise of CDW to the subsurface is an important precondition for warm water to reach the continental shelf.

The wind pattern reverses further south towards the coast. The prevailing Easterlies drive coastal Ekman convergence and promote the formation of the Antarctic Slope Current (ASC), which follows the continental shelf break such that the shallower side is to its left. The main front of the ASC is the ASF with downsloping isopycnals towards the shore. Where the ASF is strong, it helps to separate the rather cold and fresh continental shelf waters from the relatively warm and salty CDW offshore. In contrast, continental shelves that have a weak ASF and are in close proximity to the ACC, such as at the Bellingshausen and Amundsen Seas, contain modified CDW. The manifestation and variability of the ASF therefore plays an important role in controlling the heat supply to the Antarctic continental shelf.

1.2.1 The Antarctic Slope Front

The term ASF was introduced by Gill (1973) in the Weddell Sea, but it was Jacobs (1991) who first described the almost circumpolar nature of the ASF based on available observations at the time. Since then, a number of designated field (e.g., Thompson et al., 2014; Peña-Molino et al., 2016; Azaneu et al., 2017) and modelling studies (e.g., Nøst et al., 2011; Hattermann et al., 2014; Stewart and Thompson, 2015, 2016) have been conducted as recently reviewed by Thompson et al. (2018). Despite the progress in the last two decades, the authors point out that many key questions still remain.

The ASF manifests as a cross-slope density gradient with a strong signal in the temperature distribution (Figure 1.3). The front is also present in

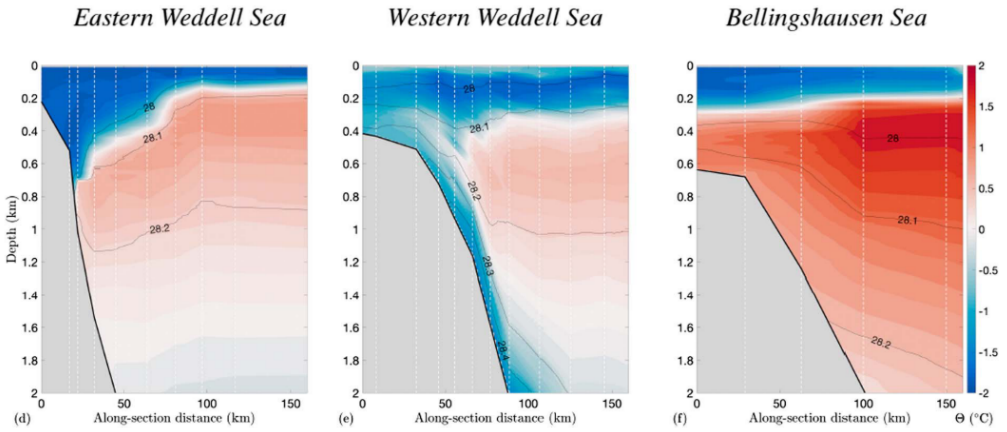

Figure 1.3: Figure 3d-f from Thompson et al. (2018) showing observations of the ASF (black contours indicate the neutral density distribution) and the temperature distribution (shading) along three different sections. The vertical, white dotted lines indicate the location of data sampling. Sections originate from Heywood and King (2002) for the eastern Weddell Sea, Thompson and Heywood (2008) for the western Weddell Sea, and Orsi and Whitworth (2005) for the Bellingshausen Sea.

chemical constituents such as oxygen, silicate and phosphate, and has been reported to be a biological hotspot (Jacobs, 1991). The ASC has average along-slope velocities between 0.1 - 0.3 m s^{-1} and exports freshwater downstream through sea ice and icebergs. Similar to the ACC, the ASC consists of multiple jets that vary in time and space (Stern et al., 2015; Stewart and Thompson, 2016). At wide continental shelves, a second, weaker current splits up from the ASC to the south. This Antarctic Coastal Current (ACoC) follows the ice shelf front and transports water from the ice shelf cavities to ice shelves downstream. The names of the two currents are sometimes used interchangeably, but to avoid confusion, this thesis equates the ASC with the slope current of the ASF.

The ASC is a geostrophically balanced flow[3] with a vertical shear and a cross-slope pressure gradient, which can be associated with the ASF. The ASC is intensified in the surface to subsurface at about 200 m and can be found as deep down as 1000 m. In agreement with the thermal wind bal-

[3]A geostrophic flow assumes a balance between pressure force and Coriolis force so that isobars act as streamlines (e.g. Cushman-Roisin and Beckers, 2011, chapter 7).

ance[4], the along-shore velocities decrease with depth and sometimes reverse sign near the bottom (Heywood et al., 1998; Chavanne et al., 2010). A bottom intensified westward flow exists in areas of DSW export where the dense plume turns westward under the influence of the Coriolis force (Foldvik et al., 2004). This westward undercurrent is therefore controlled by different dynamics and decoupled from the actual ASC.

1.2.2 Spatial and temporal variability

The ASF has an almost circumpolar extent, but its structure varies considerably along the coastline (Figure 1.3). Key factors that impact the shape of the ASF are the atmospheric wind pattern, DSW production, the bathymetry, advection and mixing, and the proximity to the ACC. Based on the currently existing hydrographic observations, Thompson et al. (2018) classify the ASF into three different regimes with different cross-slope density gradients.

At "warm shelves", the combined effect of a lack in persistent winds, DSW formation and – at the western Antarctic Peninsula – the proximity to the ACC largely inhibits the formation of an ASF (red sections in Figure 1.4). The remainder of the coastline does feature an ASF where "fresh shelves" have the strongest cross-slope density gradients. This regime is typical for East Antarctica and the eastern Weddell Sea (green sections in Figure 1.4). Here, the strong winds generate coastal Ekman convergence and downwelling, which results in tilting of the isopycnals, and limits a direct connection between water masses on the continental shelf and offshore. Finally, "dense shelves" are characterised by localised DSW export and can be found in the Weddell and Ross Seas, along the Adélie coast, and at Cape Darnley (purple sections in Figure 1.4). The export of DSW facilitates a pathway for water to move cross-slope within the same density class. A more detailed introduction to the different ASF regimes can be found in Chapter 3.1.

The ASF and ASC are also highly variable in time. Mesoscale processes, winds, coastal waves, and tides introduce variability with an associated time

[4]The thermal wind balance combines hydrostatic and geostrophic balances and explains how a horizontal density gradient can be maintained by a vertical shear of the horizontal velocity field (e.g. Cushman-Roisin and Beckers, 2011, chapter 15).

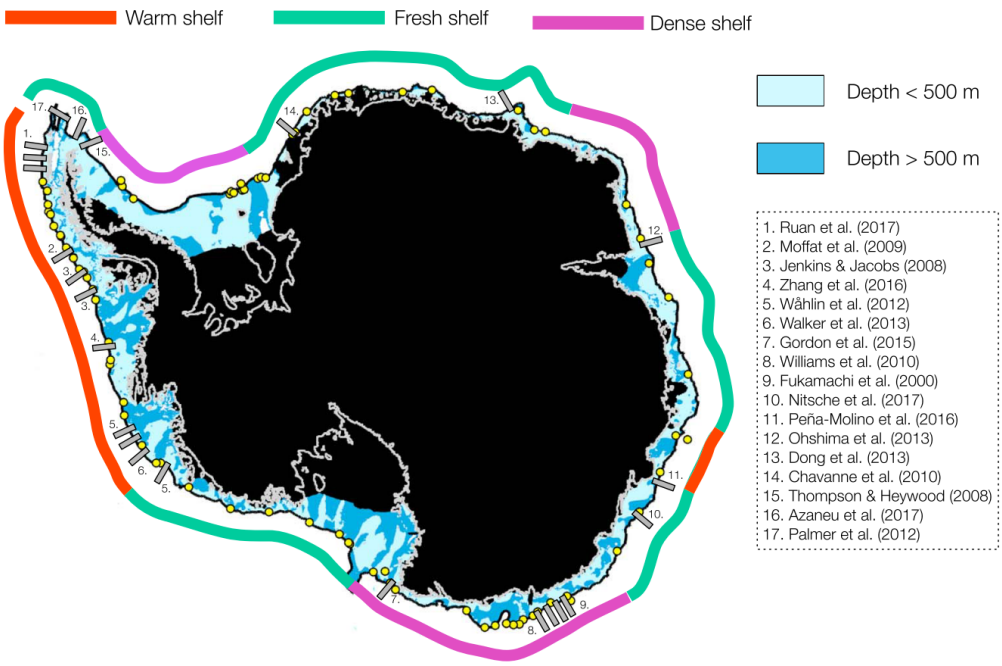

Figure 1.4: Figure 4c from Thompson et al. (2018) showing the spatial distribution of three different ASF classifications as described in the text. Sections that were used to classify the ASF are shown as grey bars. The numbers refer to the respective reference study given in the legend. Yellow dots indicate data points from Baines and Condie (1998) and Amblas and Dowdeswell (2018) that were used to infer the presence of DSW.

scale from days to weeks (Padman et al., 2009; Nøst et al., 2011; Thompson et al., 2014; Stewart and Thompson, 2015; Peña-Molino et al., 2016; Azaneu et al., 2017). These fluctuations can be crucial for cross-slope heat transport as will be described in Chapter 1.3. On a seasonal time scale, the wind is the main driver of variability in ASC transport (Aoki et al., 2010; Mathiot et al., 2011; Armitage et al., 2018), but the seasonal presence of freshwater due to sea ice melt can also drive a considerable seasonal signal (Núñez-Riboni and Fahrbach, 2009). The ASC peaks in autumn and winter and is weakest in summer, mirroring the intensity of the combined effect from winds and sea ice. The largest magnitudes exist in the Weddell Sea where the current speed doubles (Núñez-Riboni and Fahrbach, 2009), but high speeds are also observed in the Ross Sea and along the East Antarctic coastline. The seasonality in hydrography is confined to the water above the main

thermocline (Hattermann, 2018). Between the shallow summer mixed layer and the main thermocline is a layer of winter water that extends to the surface in winter. The water below the main thermocline is protected from the surface fluxes and therefore does not reveal a strong annual cycle. While this is true for the continental shelf break, the continental shelf may be subject to deep convection in winter and thus reveals a very weak vertical stratification in the entire water column during this time of the year.

Numerical models and observations further suggest that the ASC consists of multiple jets that are separated from each other by more than the Rossby deformation radius and that drift offshore (Stern et al., 2015; Azaneu et al., 2017; Peña-Molino et al., 2016; Stewart and Thompson, 2016). The jet migration occurs on times scales of years and indicates a rather transient character of the ASF system. Additionally, patterns of climate variability such as the Southern Annual Mode control the large-scale atmospheric pressure field and with it the ocean circulation on decadal time scales.

1.3 Cross-slope heat exchange

Observations of slope currents in Antarctica and elsewhere show that the local mean flow is along a topographic slope. The topographic slope inhibits to a great extent cross-slope flows and with this exchanges between the continental shelf and the deep ocean. The continental slope alters the background barotropic Potential Vorticity (PV) gradient, which is given by the ratio of the Coriolis parameter f to the water column thickness H (Cushman-Roisin 2011, chapter 7). The cross-slope gradient in H translates to a cross-slope PV gradient with larger values on the continental shelf and smaller values offshore. Because the PV must be conserved, the flow tends to follow constant values of PV, largely inhibiting a cross-slope transport. Without a geostrophic mean flow, it is the small-scale variability that plays a crucial role in cross-slope heat exchange. Due to a strong cross-slope temperature gradient, even a small exchange can effectively alter the water mass properties on the continental shelf (Heywood et al., 2014). The following reviews the most prominent mechanisms that support an exchange of heat across the ASF.

Bathymetric control

CDW, the warmest water mass in the Southern Ocean, is located in the subsurface, offshore of the continental shelf break. Where the ASF is weak, isopycnals are aligned with the horizontal and heat exchange across the shelf break is, to a first degree, a function of thermocline depth relative to the depth of the ocean.

Troughs that connect the open ocean with ice shelf cavities lower the depth of the ocean locally, allow a constant PV "pathway", and favour the inflow of the relatively warm CDW. The Marguerite Trough in the Bellingshausen Sea (Moffat et al., 2009), the trough leading to the Dotson and Getz Ice Shelves in the Amundsen Sea (Wåhlin et al., 2010), the Filchner Trough in the south eastern Weddell Sea (Ryan et al., 2017), and the trough north of the Totten Ice Shelf in East Antarctica (Nitsche et al., 2017) are examples along the Antarctic margin that show inflow of modified CDW in troughs. The inflow of the relatively warm water along a trough can also be understood as a compensation for outflow of meltwater (St-Laurent et al., 2013). While the inflow and the outflow should have the same magnitude in a steady state scenario, they are set by very different physical processes and transient changes may evolve rather independently.

Interactions of the mean flow and/or waves with troughs have additionally been identified to transport heat to an ice shelf cavity (St-Laurent et al., 2013; Daae et al., 2017). When the mean flow of a slope jet meets a cross-shelf trough, the change in water column depth leads to the formation of vortices that are advected by momentum onshore and carry heat with them. Further, wave breaking at the downstream side of a trough introduces vertical mixing and a net onshore heat transport.

Eddy-driven control

In the absence of troughs (and a net along-shore pressure gradient), mesoscale and submesoscale eddies transport CDW onto the continental shelf break (Nøst et al., 2011; St-Laurent et al., 2013; Stewart and Thompson, 2015; Stewart et al., 2018). While most of the research on mescoscale variability originates from regional or idealised numerical modelling, observational evi-

dence for eddy activity exists from the western Weddell Sea (Thompson et al., 2014; Azaneu et al., 2017) and the west Antarctic Peninsula continental shelf (Moffat et al., 2009; McKee et al., 2019).

The most energetic margins are characterised by Antarctic Bottom Water (AABW) production (Stewart and Thompson, 2015). The export of DSW, the precursor of AABW, lifts the isopycnals and establishes an isopycnal connection between the water masses on the continental shelf with the CDW offshore. Under such conditions, along-isopycnal stirring by eddies is sufficient to transport heat across the shelf break (Thompson et al., 2014; Stewart and Thompson, 2015; Daae et al., 2017). Instabilities at the AABW/CDW interface energise the eddies and set up an eddy-driven overturning circulation which counteracts the export of DSW (Stewart and Thompson, 2016).

Cold and fresh continental shelves are characterised by a strong ASF and isopycnals that intersect with the sloping bottom. There is no cross-slope connection of the water masses and the continental shelf is largely separated from the deep ocean. Instabilities of the ASF can, however, lead to diapycnal mixing by eddies near the ocean bottom and facilitate some onshore heat transport and counteract the wind-driven Ekman downwelling (Nøst et al., 2011; Hattermann et al., 2014).

Other mechanisms

Other mechanisms can cause intrusions of CDW onto the Antarctic continental shelf. Tides may have manifold effects as they (i) generate cross-slope movement of water, (ii) contribute to ocean mixing and thereby change water mass compositions, and (iii) modify circulation patterns by setting up mean (rectified) flow (see Flexas et al. (2015) as well as the review by Padman et al. (2018) and references therein). Limited onshore heat transport has also been suggested to occur in the bottom Ekman layer, if cross-shelf gradients in temperature are large (Klinck and Dinniman, 2010). Onshore transport occurs when the flow along the continental slope is to the east, however this is usually not the case. On a time scale of a year, changes in winds may lead to a drop in sea surface height, which is then transported around the

shelf break via coastal Kelvin waves[5] (Spence et al., 2017), and initiates a barotropic flow that favours onshore bottom Ekman transport (Webb et al., 2019). Lastly, variability in the surface stress, provoked by both winds and sea ice, over the Antarctic continental shelf break shows high correlation with onshore heat transport (e.g. Thoma et al., 2008; Kimura et al., 2017), which could be associated with stronger/weaker currents or upwelling of the relatively warm water in the subsurface.

1.4 Thesis objectives and outline

The ocean has a major control on the stability of the Antarctic ice sheet and global sea level. Changes in the climate system due to global warming warrant a better understanding of the physical processes that regulate the transport of heat across the continental shelf break and the water mass composition on the continental shelf. This thesis aims to address this need by investigating the dynamics of the ASF. In particular, the goals of the thesis are:

- To develop an idealised model configuration of the Antarctic continental shelf break system in a zonally-symmetric periodic domain.
- To analyse the ASF behaviour for fresh continental shelves that occupy extensive sections along the Antarctic margin.
- To investigate the role of mechanical and buoyancy surface forcing for the shape of the ASF and to define thresholds in the forcing.
- To explore the effect of increased basal meltwater on the Antarctic continental shelf circulation and to identify possible feedbacks.

The thesis is organised as follows. The remainder of **Chapter 1** summarises the challenges in studying the Antarctic continental shelf break sys-

[5]Kelvin waves are barotropic waves and constitute a balance between the Coriolis force and a lateral boundary and can be triggered by, e.g., a wind disturbance that translates to a sea surface height anomaly (Cushman-Roisin and Beckers, 2011). Kelvin waves travel along a coastline, in the Southern Hemisphere with the shallower side to its left. A Kelvin wave need approximately 1.5 days to travel around the Antarctic coastline (Kusahara and Ohshima, 2014).

tem and motivates the use of a numerical model of ocean circulation as a tool to answer the posed research questions.

Chapter 2 introduces an idealised model of the Antarctic continental shelf break system in a zonally-symmetric periodic domain. Focussing on the fresh continental shelf case, this chapter demonstrates how offshore bottom Ekman transport of shelf waters leads to the development of a deep bottom mixed layer at the lower continental slope. The elevated mixing rates drive an intrinsic variability of the ASF that allows CDW to move closer to the continental shelf. and compared against sparse observations of bottom mixed layers at the Antarctic continental slope. A modified version of this chapter is currently under review for publication in Journal of Physical Oceanography, entitled *Bottom mixed layer drives intrinsic variability of the Antarctic Slope Front.*

Chapter 3 investigates the role of mechanical and buoyancy forcing for the slope of the isopycnals and defines thresholds between different ASF regimes in the idealised domain of Chapter 2. The modelled ASF regimes are discussed with respect to their temporal variability as well as their transient versus steady state behaviour.

Chapter 4 performs perturbation experiments in a state of the art circumpolar ice shelf/ocean/sea ice model (Naughten et al., 2017, 2018a) to test the isolated effect of increased meltwater production on the continental shelf circulation. The model output is analysed with regards to changes in the dynamics along the Antarctic continental slope and to feedback mechanisms on basal melting based on selected regions to show different responses to the perturbation along the Antarctic coastline.

Finally, concluding remarks and ideas for future research are presented in **Chapter 5**.

1.5 Approach

Describing the oceanography along the Antarctic continental margin is challenging for a number of reasons. First, Antarctica is undisputedly the remotest place on Earth, where sea ice coverage, icebergs and the lack of light deny a ship-based access for most of the year. Second, while advances in

satellite measurements, autonomous underwater vehicles such as argo floats as well as the increasing number of tagged seals have greatly improved the observational data coverage in the last decade, spatial and temporal undersampling remains to be a problem (Schmidtko et al., 2014). Third, the smallness of the internal Rossby radius of deformation, which is only a few kilometres due to the weak stratification, the shallow water column depth, and the large Coriolis parameter at high latitudes (Hallberg, 2013), demands high horizontal resolution of both observations and models.

Numerical models have proven to be a valuable tool in enhancing the mechanistic understanding of Antarctic continental shelf processes. Taking computational resources into account, regional or idealised configurations can be run with a resolution that resolves the mesoscale and small-scale bathymetric features. The combined advantages of realistic governing physics together with the reproducibility of experiments and the progress in computational power have lead to a prevalence of modelling studies in the last two decades (e.g. Nøst et al., 2011; Hattermann et al., 2014; Daae et al., 2017; Stewart and Thompson, 2015, 2016; Nakayama et al., 2014b; Dinniman et al., 2012; Thoma et al., 2008). As a consequence the dynamical understanding of the Antarctic continental shelf circulation has improved. Additionally, model results can be used to inform future field campaigns by providing information on key areas to collect observations, and help to predict future changes in the climate system.

The Regional Ocean Modelling System (ROMS) (Shchepetkin and McWilliams, 2005) is one of the numerical models of ocean circulation that has demonstrated its capabilities as a tool for studying the Antarctic margin. ROMS is a three-dimensional, free-surface, primitive equation ocean model that makes use of the hydrostatic and Boussinesq assumptions[6]. Modifications of the ROMS source code allow for ocean-ice interaction (Galton-Fenzi et al.,

[6]The hydrostatic approximation assumes that the horizontal scale is larger than the vertical scale. The vertical momentum equation reduces to the hydrostatic balance (vertical pressure gradient is equal to the density times gravitational acceleration) and removes the vertical velocity as a prognostic variable in the model. The hydrostatic approximation does not hold for turbulent processes where horizontal and vertical length scales are of similar order. The Boussinesq approximation ignores density fluctuations except in the gravity term, which simplifies the continuity equation, and allows for a diagnostic equation for the vertical velocity. (e.g. Cushman-Roisin and Beckers, 2011, chapter 3)

2012). Ice shelves are introduced as static features that do not evolve in time, but allow for changes in the pressure field and interact thermodynamically with the ocean. Additionally, ROMS can be coupled to the Community Ice CodE (CICE), a dynamic-thermodynamic sea ice model that has been coupled to a range of ocean models in the past (Hunke et al., 2015). Finally, ROMS uses a stretched terrain-following coordinate system to vertically discretise the primitive equations. The terrain-following coordinate system allows for increased resolution in the surface and bottom layers, while having a lower resolution in the centre of the water column, making it suitable to simulate coastal regions. A further advantage is that the base of the ice shelf can be represented with a single layer following the ice draft as opposed to a step-like representation typical for z-coordinate ocean models (see Kimura et al. (2013) for a thorough examination of the advantages and disadvantages of different vertical coordinate systems).

This thesis uses ROMS (i) on an idealised domain of the Antarctic continental shelf break (Chapter 2 and 3) that allows for a high horizontal resolution and (ii) on a circumpolar domain that allows for interaction between different regions, but has a lower horizontal resolution (Chapter 4). All simulations include ocean-ice interaction at ice shelf bases, but only the circumpolar set-up also makes use of the CICE sea ice model. More detailed information on the model configurations used in this thesis are given in the respective chapters and Appendix A.

Chapter 2

Deep bottom mixed layer drives intrinsic variability of the Antarctic Slope Front

This chapter introduces the process model of the Antarctic continental shelf break system. It further demonstrates how offshore bottom Ekman transport leads to an intrinsic variability of the ASF for the fresh continental shelf case. Large sections of the Antarctic coastline could potentially be prone to this mechanism which allows the relatively warm CDW to move closer to the continent. The discussion compares the model results to available observations and explores the sensitivity of the results to the chosen model parameters.

Abstract

The ASF is located along much of the Antarctic continental shelf break and helps to maintain a barrier to the movement of CDW onto the continental shelf. The stability of the ASF has a major control on cross-shelf heat transport and ocean-driven basal melting of Antarctic ice shelves. Here, the ASF dynamics are investigated for continental shelves with weak DSW formation which are thought to have a stable ASF, common for regions in East Antarctica. Using an ocean process model, this study demonstrates how offshore bottom Ekman transport of shelf waters leads to the development of a deep bottom mixed layer at the lower continental slope, and subsequently determines an intrinsic variability of the ASF. The ASF variability is char-

acterised by instability events that affect the entire water column and occur every five to ten years and last for approximately half a year. During these instability events the cross-shelf density gradient weakens and CDW moves closer to the continent. Stronger winds increase the formation rate of the bottom mixed layer which causes a subsequent increase of instability events. If the observed freshening trend of continental shelf waters leads to weaker DSW formation, more regions might be vulnerable for the ASF variability to develop in the future.

2.1 Introduction

The ASF and the associated ASC are thought to be almost circumpolar. The ASF is a manifestation of the barrier to cross-slope flow posed by the topographic PV gradient and is important in regulating movement of CDW onto the Antarctic continental shelf (Jacobs, 1991; Whitworth et al., 1998; Thompson et al., 2018). CDW is a relatively warm and salty water mass that is typically found in the ACC, but once it crosses the continental shelf break and enters ice shelf cavities, usually as a modified version, it has the potential to drive strong basal melting and to influence the stability of the Antarctic ice sheet (e.g. see reviews by Dinniman et al. (2016) and Silvano et al. (2016)).

A stable ASF can isolate the colder continental shelf waters from the warmer CDW offshore (Jacobs, 1991). Warm continental shelf temperatures and high basal melt rates are consequently observed in the Amundsen and Bellingshausen Seas, where the ASF is absent or very weak due to the local atmospheric circulation pattern and the close proximity of the ACC to the shelf break (Pritchard et al., 2012; Petty et al., 2013; Rignot et al., 2013). Elevated melt rates also occur in regions characterised by submarine troughs, which connect the open ocean with ice shelf cavities, and effectively channel the warm CDW onto the continental shelf (e.g. near the Totten Glacier in East Antarctica (Rintoul et al., 2016; Nitsche et al., 2017), or the Marguerite Trough in West Antarctica (Moffat et al., 2009; St-Laurent et al., 2013)). In the absence of troughs, the export of DSW can trigger mesoscale instabilities that weaken the ASF (Stewart and Thompson, 2016). Pulses of intruding

warm water related to eddy activity have been modelled using high resolution process models (e.g. Stewart and Thompson, 2015) and observed in the northwestern Weddell Sea (Thompson et al., 2014).

Little is known about processes that may destabilise the ASF at sections around the Antarctic coastline with weak DSW production and no major troughs (e.g. along sections in East Antarctica (Thompson et al., 2018)). This study assesses the physics relevant for the Antarctic continental shelf and slope under such conditions in an ocean process model. The results show that downslope bottom Ekman transport of relatively fresh and therefore buoyant continental shelf water may lead to a deep bottom mixed layer at the lower Antarctic continental slope. The continuous freshwater input from the continental shelf region leads to bottom mixed layer instabilities that drive an intrinsic variability of the ASF. During the ASF instability events, the cross-slope density gradient relaxes and relatively warm CDW moves closer to the continental shelf break.

2.2 Process model of the continental shelf break ocean system

The numerical ocean model used in this study is the open source community ROMS version 3.6, a hydrostatic three-dimensional primitive equation finite difference model (Shchepetkin and McWilliams, 2005), which is run using a nonlinear equation of state (see Appendix A.1 for more information). The version of ROMS used here includes ice shelves and has previously been used to simulate high southern latitudes (e.g. Dinniman et al., 2011, 2012; Galton-Fenzi et al., 2012; Cougnon et al., 2013; Gwyther et al., 2014). The Coriolis parameter varies linearly on a β-plane locating the study area at about 64°S - 68°S (Appendix A.1). The model domain is 400 km (along-slope/zonal direction) by 550 km (cross-slope/meridional direction) by 3 km (depth), and is a re-entrant channel in the along-slope direction with a symmetric geometry (Figure 2.1). The bathymetry $h(j)$ for each grid cell j in cross-slope direction is a function of the cross-slope distance $y(j)$ and follows

$$h(j) = H_s + \frac{H - H_s}{2} \cdot \left(1 + \frac{2\pi \tanh(y(j) - L_{slc})}{L_{sl}}\right) \tag{2.1}$$

with the continental shelf depth H_s, the maximum depth H, the centre of the slope L_{slc} and the slope width L_{sl}. The mean slope is 1.6 % which is similar to slopes found along 110°E - 125°E in East Antarctica. The southernmost 100 km of the domain are covered by an ice shelf with depth $zice(j)$, given as

$$zice(j) = \begin{cases} -H_{ic} + \arctan\left(\frac{y(j)\pi}{2(L_{ic}-L_{icf})}\right) \cdot (H_{ic} - H_{icf}), & \text{for } 0 \leq y(j) \leq L_{ic} - L_{icf} \\ -H_{icf} + \frac{y(j)-(L_{ic}-L_{icf})}{L_{icf}} \cdot H_{icf}, & \text{for } L_{ic} - L_{icf} \leq y(j) \leq L_{ic} \\ 0, & \text{for } L_{ic} \leq y(j) \end{cases} \tag{2.2}$$

with the maximum ice shelf depth H_{ic}, the depth at the front H_{icf} and the respective cross-slope distances L_{ic} and L_{icf}. The ice shelf base is coupled thermodynamically to the ocean following Galton-Fenzi et al. (2012). The ice-shelf thermodynamics account for the effect of basal melting and related changes in water mass properties and dynamics. The cold ice shelf cavity temperature induces a melt rate of approximately 0.03 m y^{-1} which is small compared to observed melt rates of, for example, 0.6 m y^{-1} at the Amery ice shelf (Galton-Fenzi et al., 2012; Depoorter et al., 2013; Rignot et al., 2013), see also Appendix A.2. The salinity on the continental shelf is approximately 0.01 psu higher in a model run without thermodynamics under the ice shelves. Hence, the water mass composition on the continental shelf is predominantly set by the surface restoring.

The model grid has a horizontal resolution of 1 km and 30 vertical layers that are equally intensified near the surface and bottom using terrain-following vertical coordinates (Figure 2.1b). The average vertical cell thickness in the ocean interior is 34 m on the continental shelf, 121 m at the continental slope, and 205 m in the deep ocean. The thickness of the surface and bottom grid cells varies between 4 m, 11 m, and 20 m, respectively. To justify the choice of grid resolution, a resolution analysis has been performed (see Appendix A.2) with the aim to resolve mesoscale dynamics which have been identified to substantially control cross-shelf heat exchange (Dinniman et al., 2016).

The model configuration uses a fourth-order centred advection scheme, the K-Profile Parameterisation (KPP) mixing scheme (Large et al., 1994) that accounts for convective mixing due to shear instability, double-diffusive

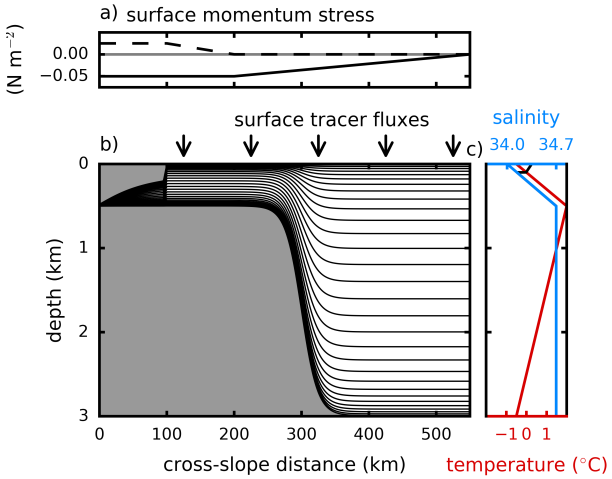

Figure 2.1: Set-up of zonally symmetric process model. a) Along-slope (solid) and cross-slope (dashed) surface momentum stress. b) Bathymetry, ice shelf draft and terrain-following vertical layers (30 levels) on a cross-slope section. c) Temperature (red) and salinity (blue) profiles prescribed at the northern boundary. The same profiles are applied to the entire domain as initial conditions with a minor adaptation to the salinity profile in the upper 100 m (black). The salinity increases at the surface to create an unstable stratification which allows instabilities to develop in the zonally symmetric domain.

mixing, and the vertical mixing of momentum and tracer in the mixed layer, and uses a quadratic bottom stress of $3 \cdot 10^{-3}$. A complete list of the specific parameter choices is given in Tables A.1 and A.2, and the applied C-Pre-Processor (CPP) options are given in Tables A.3 and A.4 in Appendix A.1.

The western and eastern boundaries are periodic while the northern boundary is clamped to salinity and temperature profiles that are representative of the Southern Ocean (Figure 2.1c), and are the source of CDW in the domain. The initial conditions use the same values as the northern boundary profiles. However, in order to develop eddies in the zonally symmetric domain, the stratification of the upper water column has been made statically unstable in the entire domain by changing the salinity profile in the upper 100 m (Figure 2.1c, black line). Additionally, three randomly distributed grid cells of the otherwise zero momentum field were initialised with a small zonal and meridional velocity of 10^{-5} m s^{-1}. Without these changes, the flow field does not

become unstable. The model is initially spun-up for 25 years to equilibrate water masses over the continental shelf region, which can be monitored by the basal melt rate of the ice shelf. The model is then restarted and run for 30 years before it is integrated for an additional 22 years (year 30 to 51) with output every three months and for another six years (year 52 to 57) with daily output to allow an analysis at higher temporal resolution. The geometric symmetry in along-slope direction allows the calculation of zonal means, which has been done for all diagnostics presented.

The applied surface forcing ensures that only weak DSW forms on the continental shelf. The surface grid cells are relaxed to a temperature of $-1.85°C$ and a salinity of 34.45 psu, modulated by a relaxation time scale of 60 days (see Appendix A.3 for a detailed description). The main component of the surface momentum stress is oriented in an along-slope direction (westward) with a smaller cross-slope component representing the northward katabatic wind (Figure 2.1a). The applied momentum stress profile is based on the COREv2 climatology (Large and Yeager, 2009) at sections along 110°E - 125°E in East Antarctica. This region is characterised by ice shelves along the margin, and no or only weak DSW production. Two additional sensitivity experiments are performed with 50% and 150% momentum stress of the control run. All simulations represent constant winter conditions.

2.3 Results

2.3.1 Simulated structure of the ASF and ASC

At the continental shelf break, the isopycnals slope down to the seabed in an onshore direction, as there is neither dense bottom water actively formed nor prescribed at the lateral boundaries which would force the isopycnals to lift and flatten, or even reverse (Figure 2.2a). An ASC is produced with a dominant along-slope westward component with maximum values of around 0.3 m s^{-1} near the surface in the ASF region (Figure 2.2a). The maximum of the ASC is located 25 km offshore from the centre of the bathymetric slope. In the presence of a cross-shelf density gradient and in agreement with the thermal wind balance, the velocity decreases towards the bottom. There is no undercurrent in an opposing direction nor upwards tilting isopycnals near

the bottom. The simulated ASC speed compares well with both observations (Bindoff et al., 2000) and realistic modelling work that has been done in East Antarctica (Mathiot et al., 2011; Gwyther et al., 2014). On the continental shelf, stratification is weak and the along-slope velocities are approximately 0.1 m s^{-1} in a westward direction.

The cross-slope velocity field on the continental shelf is an order of magnitude weaker than the along-slope velocity and consists of an onshore surface Ekman transport and an offshore bottom Ekman return flow (Figure 2.2b and 2.2c). The cross-slope circulation on the continental shelf is confined to the top and bottom 100 m, respectively, as indicated by the mean overturning stream in Figure 2.2c. The stream function,

$$\Psi = L_x \int_z^0 \bar{v}\, dz, \tag{2.3}$$

is calculated as the vertical integral of the along-slope average (overbar) of the cross-slope velocity v (positive to the north) multiplied by the domain width L_x in order to obtain an overturning transport (1 Sv = 10^6 m^3 s^{-1}).

2.3.2 Instability of the ASF

The main part of the ASF is located in a region 300-340 km from the southern boundary and extends throughout the water column (Figure 2.3c and 2.3d between blue and green line). Figure 2.3a shows the ocean Heat Content (HC) for this region which is given by

$$\mathrm{HC} = \sum_{i,j,k} T_{i,j,k}\, \rho_{i,j,k}\, c_p\, \Delta V_{i,j,k}, \tag{2.4}$$

where T (measured in degree Kelvin) is the ocean temperature, $c_p = 3974$ J kg^{-1} K^{-1} is the specific heat capacity of polar ocean seawater, ρ is the in situ density, and ΔV is the volume of each cell (i, j, k), where i is the cross-slope index and k the vertical index. Similar, Figure 2.3b shows the ocean Heat Transport (HT) which is given by

$$\mathrm{HT} = \sum_{i,k} v_{i,k}\, T_{i,k}\, \rho_{i,k}\, c_p\, \Delta A_{i,k}, \tag{2.5}$$

where ΔA is the area of a cell, across an along-slope section at 300 km and 340 km north of the southern boundary.

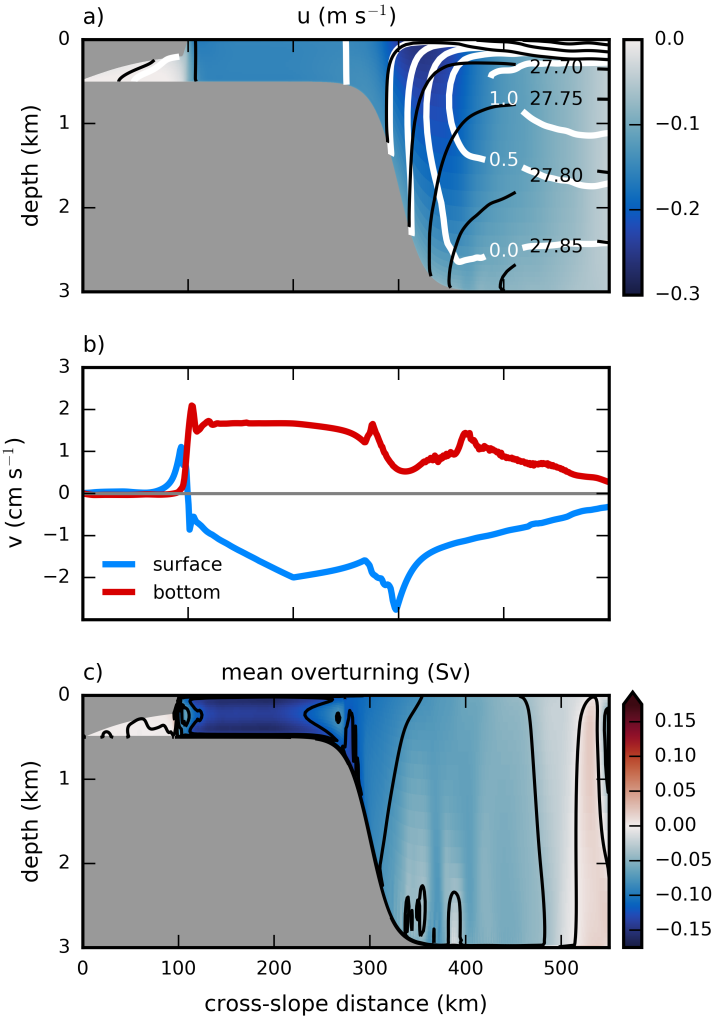

Figure 2.2: a) Cross-slope section showing zonal mean along-slope velocities at the beginning of year 55. Density contours are black and temperature contours are white. b) Associated surface (blue) and bottom (red) cross-slope velocity. Negative velocities are to the south (onshore) and positive velocities are to the north (offshore). c) Mean overturning stream function with a contour interval of 0.1 Sv, see text for the calculation. Negative values (blue) indicate an anti-cyclonic (anti-clockwise) circulation.

The HC time series reveals that the ASF contains an intrinsic variability (Figure 2.3a). During the 27 year length of output shown, four instability events occur with an aperiodic timing of approximately five to ten years. The

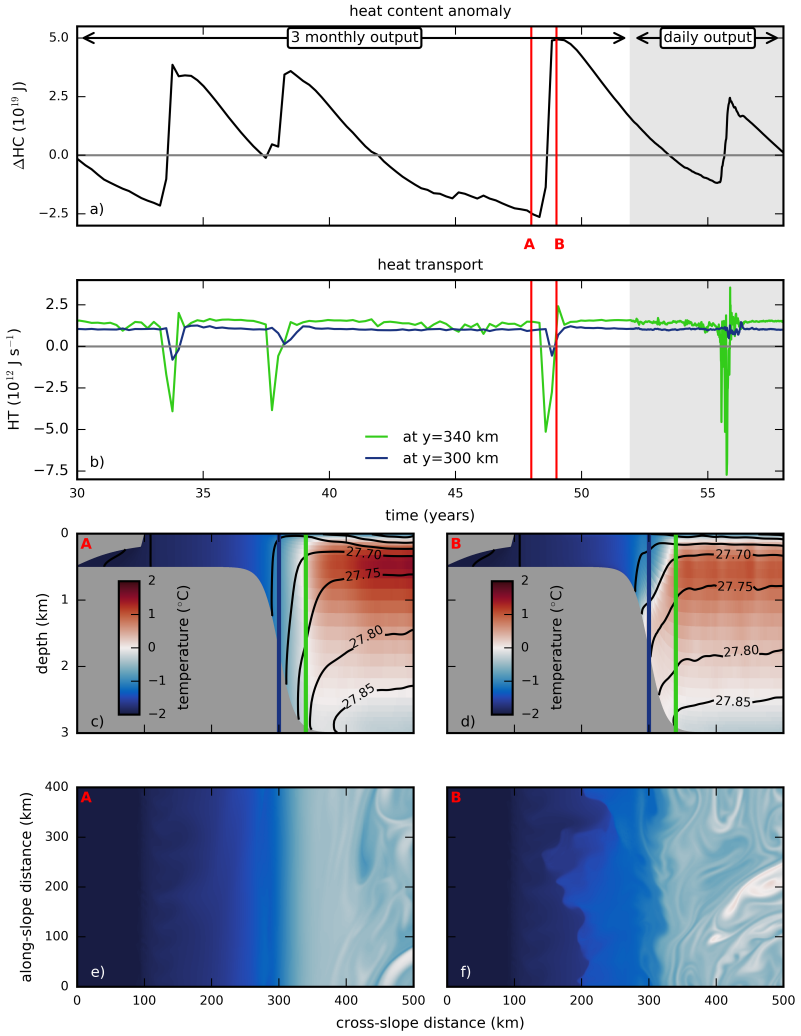

Figure 2.3: a) Time series of change (anomaly with respect to year 30) in ocean heat content for the region 300-340 km from the southern boundary as indicated by the blue and green vertical line in panel c) and d). b) Time series of ocean heat transport through the boundaries. Gray horizontal line is the zero value, gray shading indicates a time frame with higher (daily) output that is shown in Figure 2.4. c) and d) Zonal mean temperature with density contours at year 48 (red vertical line labelled *A* in panel a) and at year 49 (red vertical line labelled *B* in panel b). e) and f) Associated surface temperature distribution, colorbar as in panels c) and d).

instability events are of varying intensities and each event lasts approximately six to nine months. Between two instability events, the HC has a negative trend and the ASF strengthens: the isopycnals steepen and move offshore (see

isopycnals in Figure 2.3c and 2.3d as well as in Figure 2.5). As a consequence, the heat is also moving offshore which is indicated by the positive sign of the HT (Figure 2.3b). During an instability event phase, the southward transport of heat towards the ASF region increases (green line in Figure 2.3b) while the transport onto the continental shelf itself is almost constant (blue line in Figure 2.3b), and the HC consequently also increases.

Cross-sections of temperature and density just before (year 48, Figure 2.3c) and during (year 49, Figure 2.3d) an instability event show the change in the density field which enables CDW to move across-slope. The associated surface temperature distributions are shown in Figure 2.3e and 2.3f. The net heat transport across the continental slope averaged over the four events shown in Figure 2.3a and 2.3b is 2×10^{11} J s^{-1} in an offshore direction as surface waters (flowing onshore) are colder than the deep waters (flowing offshore). The exact value will depend on the chosen averaging time period. In this case, the net offshore heat transport is equivalent to a residual cooling of the continental slope area by 0.04°C in one year.

2.3.3 Energetics of the instability events

The intrinsic variability can be understood in more detail from Figures 2.4, 2.5 and 2.6. To begin with, Figure 2.4 shows Hovmöller diagrams (depth against time) at 340 km north of the southern boundary, because the variability is strongest in the offshore part of the ASF (Figure 2.3b and 2.5). Shown is the last instability event of Figure 2.3 (gray shaded area in panels 2.3c and 2.3d) with a daily resolution. The energy conversion terms in Figure 2.4d and 2.4e are based on a two-month running mean.

During the buildup to the instability event from year 52 to the middle of year 55, the bottom water is overall cooling and freshening over time, as indicated by the 0 °C temperature contour and the 34.6 salinity contour in Figure 2.4a. The cooling and freshening signal originates from shelf water that is advected down the continental slope in the bottom Ekman layer (Figure 2.2b and 2.2c). The flux of the relatively buoyant shelf water compared with the deep ocean leads to statically unstable conditions near the bottom and to enhanced vertical mixing and convection (Figure 2.4b, shading). The resulting convection depth, defined as the depth where the water parcels

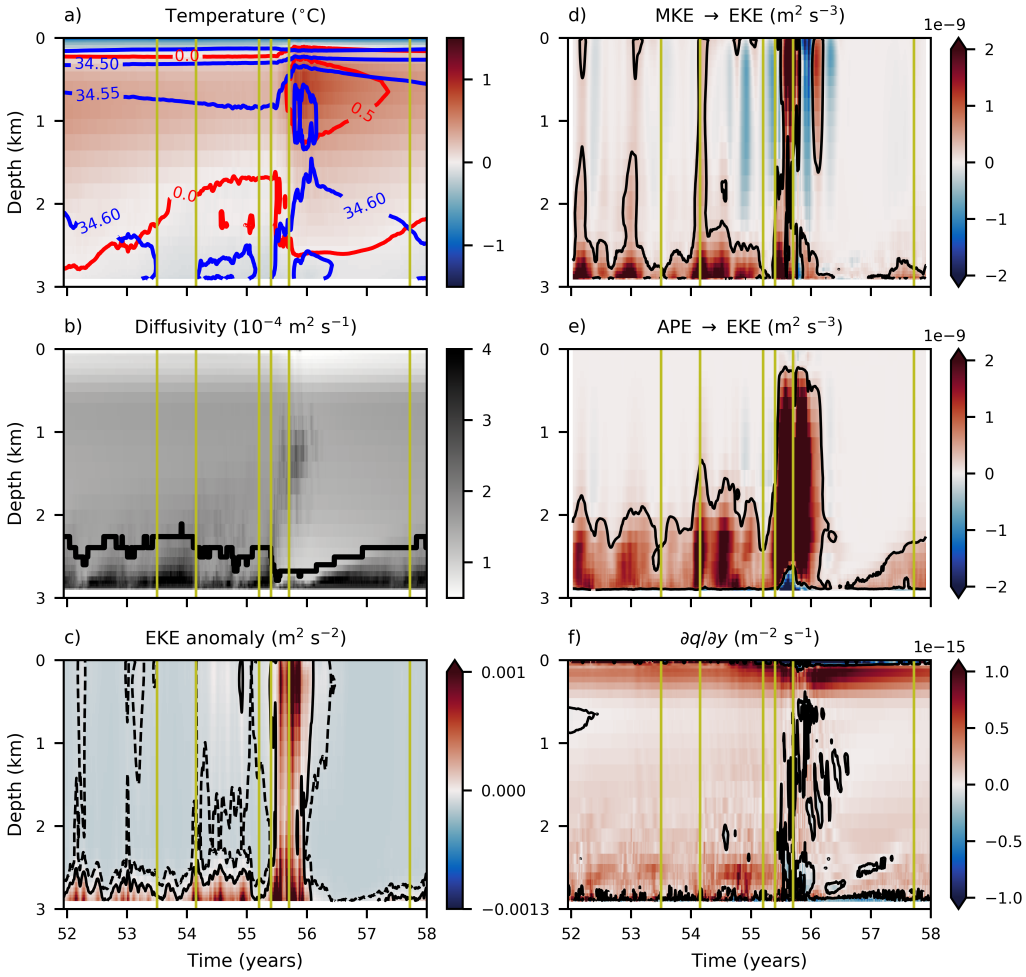

Figure 2.4: Hovmöller diagrams at 340 km from the southern boundary (green line Figure 2.3c and 2.3d). Shown are daily averages, with the exception of panel d) and e) which are two months running means. a) Temperature distribution with salinity (blue) and temperature (red) contours. b) Vertical diffusivity with convection depth measured from the bottom (thick solid line). c) EKE anomaly with zero value contour (thin solid) and -10^{-4} m^2 s^{-2} contour (thin dashed). d) Barotropic energy conversion from mean kinetic to eddy kinetic energy (positive) with 0.25·10^{-9} m^2 s^{-3} contour. e) Same as for d) but for baroclinic energy conversion from available potential to eddy kinetic energy (positive). f) Meridional potential vorticity gradient with zero contour in black. The yellow vertical lines indicate the time of the snapshots shown in Figure 2.5.

of the bottom grid cell reach their neutral buoyancy level when artificially lifted, is used here to approximate the depth of the bottom mixed layer and varies over time between 120 m and 800 m (Figure 2.4b, thick black contour). The supply of fresh continental shelf water deepens the bottom mixed layer, which is deepest just before an instability event. However, the deepening is not steadily towards the main instability event at the middle of year 55, but is disrupted by less intense instability events (an example of which is shown in Figure 2.5b) which lead to a shallowing of the bottom mixed layer (Figure 2.4b).

Figure 2.5 depicts snapshots in time of the cross-slope Eddy Kinetic Energy (EKE) field to illustrate different stages of the intrinsic variability and to give further evidence that the instability events are triggered from the bottom. The EKE is the kinetic energy associated with the time varying flow, as indicated by the prime, and calculated as

$$\begin{aligned} \mathrm{EKE} &= \frac{1}{2}\left(\langle u'^2\rangle + \langle v'^2\rangle\right) \\ &= \frac{1}{2}\left(\left(\langle u^2\rangle - \langle u\rangle^2\right) + \left(\langle v^2\rangle - \langle v\rangle^2\right)\right), \end{aligned} \tag{2.6}$$

using daily averaged model output of the horizontal velocity components $\langle u\rangle$ and $\langle v\rangle$, and their squared values $\langle u^2\rangle$ and $\langle v^2\rangle$. Maxima of EKE always exist near the sea floor at the lower continental slope (also see Figure 2.4c). The elevated EKE is confined to the sea floor when the bottom mixed layer is deep (Figure 2.5a, 2.5c and 2.5f), but extends further up in the water column during an instability event (Figure 2.5b, 2.5d and 2.5e). Figure 2.5b is an example for a less intense instability event mentioned before, where the elevated EKE does not reach all the way to the surface unlike at year 55 (Figure 2.5e). This latter "main" instability event first develops similarly (Figure 2.5d), but the elevated EKE then reaches all the way to the surface, changing the stratification noticeably at the lower continental slope and leading to a positive spike in the heat content as shown in Figure 2.3a. The EKE declines again after the instability event (Figure 2.5f).

EKE arises from conversion of energy from both Mean Kinetic Energy (MKE) and Available Potential Energy (APE). In the primitive equations, energy exchange from MKE to EKE is due to barotropic instability and energy exchange from APE to EKE is due to baroclinic instability. While

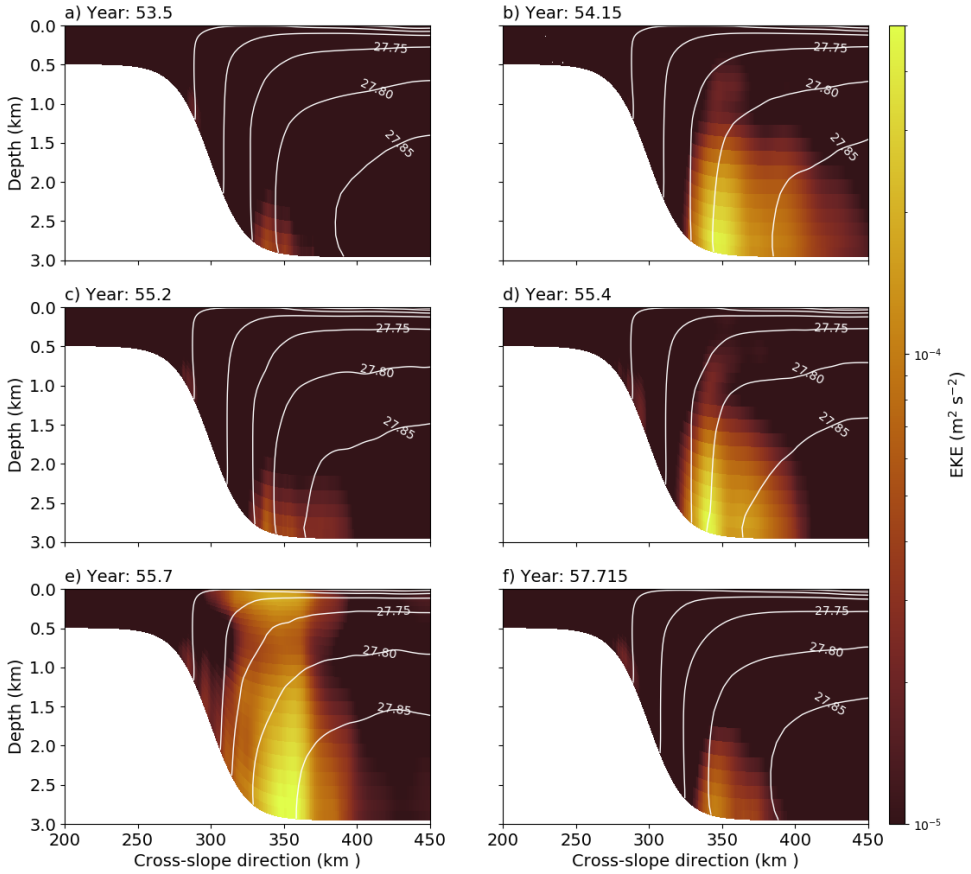

Figure 2.5: Snapshots of EKE (shaded) and contours of potential density referenced to the surface in kg m^{-3}. The time of the snapshots is indicated by the yellow vertical lines in Figure 2.4.

the barotropic instability process is associated with the lateral shear and the baroclinic instability process with the vertical shear of a flow, they often occur concurrently. Such a mixed barotropic-baroclinic instability also exists here. Barotropic energy conversion, calculated as

$$\text{MKE} \rightarrow \text{EKE} = -\langle u \rangle \frac{\partial}{\partial y}(\langle u'v' \rangle) = -\langle u \rangle \frac{\partial}{\partial y}(\langle uv \rangle - \langle u \rangle \langle v \rangle), \tag{2.7}$$

is shown in Figure 2.4d and baroclinic energy conversion, calculated as

$$\text{APE} \rightarrow \text{EKE} = \langle w'b' \rangle = \langle wb \rangle - \langle w \rangle \langle b \rangle \tag{2.8}$$

with the reduced gravity $b = -g\frac{\rho-\rho_0}{\rho_0}$, where ρ_0 is the simulated mean density and w is the vertical velocity, is shown in Figure 2.4e (for equations see Stewart and Thompson (2016) and Youngs et al. (2017), where only the advection of EKE due to the along-slope flow in cross-slope direction is of interest). The range of values for barotropic and baroclinic energy conversion is similar, pointing towards a mixed barotropic-baroclinic instability. Nevertheless, it is the baroclinic energy conversion which dominates the EKE production in the middle of the water column (Figure 2.4e), whereas the barotropic energy conversion is rather confined to the bottom and surface (Figure 2.4d). During an instability event, barotropic energy conversion dominates near the bottom which explains the existence of positive EKE anomalies during an instability event, even though EKE is also extracted and converted to APE. Accordingly, the along-slope current near the bottom is weaker during the event (not shown).

2.3.4 Barotropic and baroclinic instability criteria

Proxies for the jet's stability properties are used to analyse when conditions are favourable for barotropic or baroclinic instability. A necessary condition for barotropic instability is the zero-crossing of the PV gradient in the horizontal (here cross-slope direction). The quasigeostrophic PV gradient felt by the depth-averaged flow is calculated as

$$\beta^* = \beta + \frac{f_0}{H}\frac{\partial h_b}{\partial y} - \frac{\partial^2 \bar{u}^z}{\partial y^2}, \tag{2.9}$$

where the first term on the right hand side is the meridional gradient of the Coriolis parameter, the second term is the contribution from topography where h_b is the topographic height above H, and the last term represents the contribution from the meridional shear of the depth-averaged along-slope velocity.[1] A zero-crossing of the PV gradient therefore occurs when the shear at

[1]Equation (2.9) can be derived by taking the derivative of the potential vorticity in cross-slope direction $\frac{\partial q}{\partial y} = \beta^*$ with

$$q = \frac{f+\zeta}{h} = \frac{f_0 + \beta y + \zeta}{H - h_b} \approx \beta y + \frac{f_0}{H}h_b - \frac{\partial \bar{u}^z}{\partial y},$$

where $f = f_0 + \beta y$, $h = H - h_b$, and $\zeta = -\frac{\partial \bar{u}^z}{\partial y}$ is the relative vorticity. To obtain the approximation q has been multiplied by $(H+h_b)$ and only the large terms (using $\beta y << f_0$

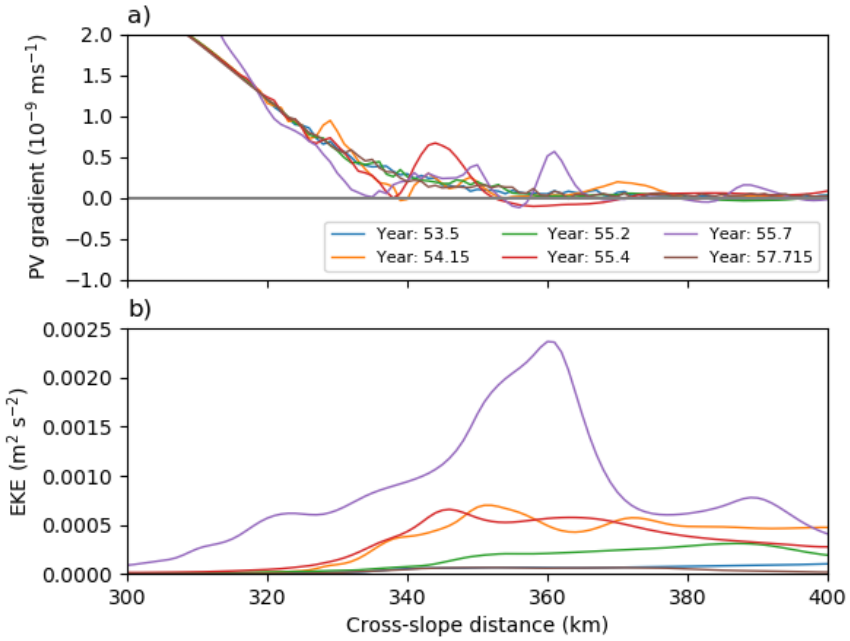

Figure 2.6: a) Depth-averaged barotropic potential vorticity gradient as a function of cross-slope distance. Zero crossings indicate barotropic unstable conditions. The topographic potential vorticity gradient is dominating at the continental slope (north of approximately 340 km from the southern boundary). b) Depth-averaged EKE as a function of cross-slope distance.

the flanks of the jet supersedes the stabilising effects of the Earth's rotation and topography. On the continental slope, the influence of the topography on the PV gradient dominates (Figure 2.6a, left part of the panel) and limits the production of EKE (Figure 2.6b and also 2.5). The influence of topography declines further north where the sea floor flattens. Barotropic unstable conditions become possible as indicated by the sign changes of the PV gradient. The position of the zero-crossings correlate with the position of local maxima of the depth-averaged EKE, demonstrating the partly barotropic character of the instability events.

A necessary condition for baroclinic instability is met when the meridional gradient of PV changes sign in the vertical (e.g. Cushman-Roisin and Beckers, 2011, chapter 17). Again, strictly speaking, the condition is only valid in the

and $h_b << H$) and terms that are relevant for the gradient calculation were kept (Pål Erik Isachsen, pers. comm.).

quasigeostrophic framework which, however, has been shown to apply beyond its formal limits (Williams et al., 2010). Here, PV is of the form

$$q = \frac{1}{\rho_0}\left(\hat{\mathbf{k}}(\langle\zeta\rangle + f)\cdot\nabla\rho\right), \tag{2.10}$$

where $\hat{\mathbf{k}}$ is the vertical unit vector and ζ is the relative vorticity (lateral terms which are relevant to the unresolved submesoscale regime are omitted). Figure 2.4f illustrates the meridional PV gradient in the water column at 340 km from the southern boundary as a function of time. Sign changes of the PV gradient are predominantly present near the sea floor and throughout the entire water column during the instability event, coinciding with the energy conversion from APE to EKE (Figure 2.4e and 2.4f). Due to very similar timing of the onset of barotropic and baroclinic instabilities, it is not possible to distinguish which of the instabilities is the trigger of the events.

2.3.5 Sensitivity to surface momentum stress

The wind-driven overturning at the continental slope is a driver for the offshore directed bottom flux of relatively fresh shelf water, which eventually leads to the thick bottom mixed layer and instabilities of the ASF. The instability events can be expected to occur more often for stronger offshore bottom transport as it is equivalent to an acceleration of the bottom mixed layer formation process. To test this hypothesis, the sensitivity of the intrinsic ASF variability to the applied surface momentum stress is now briefly presented.

Figure 2.7 shows the HC time series for three simulations with varying surface momentum stress forcing equal to 50%, 100% (control run), and 150%. The experiments indeed reveal an increase in the time between two instability events for weaker momentum stress (ten to fifteen years), and a shorter timing for stronger momentum stress (two to five years). While the timing of the intermittent variability reveals a sensitivity to the surface momentum stress, the intensity of the instability events are of comparable magnitude.

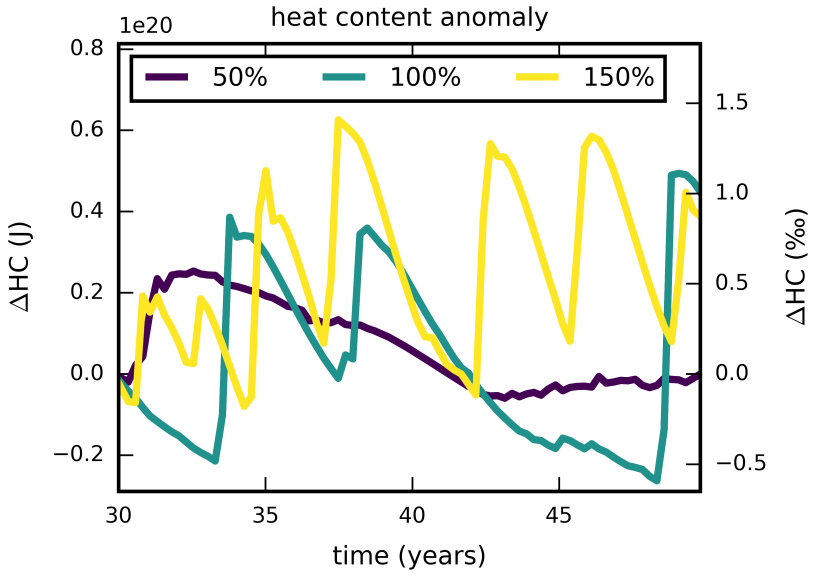

Figure 2.7: Time series of ocean heat content anomaly for three simulations with varying surface momentum stress. The 100% simulation is the control run analysed in the previous figures.

2.4 Discussion

2.4.1 Generation of a deep bottom mixed layer

The focus of this study are the ocean dynamics at the Antarctic continental slope. Under the conditions tested here, the continental shelf water is relatively buoyant as compared with the deep ocean. The wind-driven overturning circulation at the Antarctic margin, consisting of an onshore surface transport and a return flow in the bottom boundary layer (Figure 2.2b and 2.2c), enables an export of the relatively fresh shelf water down the continental slope. The resulting freshwater flux leads to a deep bottom mixed layer at the lower slope in the presence of the ASF.

The bottom mixed layer thickness in the model is largest over the lower slope with maximum values up to 800 m. Physically, the thickening can be explained by enhanced vertical mixing resulting from static instabilities in the weakly stratified bottom layer. Artificial thickening, due to decreasing vertical grid resolution offshore using a terrain-following vertical coordinate system (for the bottom grid cell from 4 m to 20 m, Figure 2.1b), is small

compared to the bottom mixed layer thickness of a few hundred meters. There are two aspects why the model might overestimate the bottom mixed layer thickness. First, the export of boundary layer water into the interior, which occurs largely along isopycnals, might be limited in the model due to the fact that the vertical grid and the isopycnals are nearly orthogonal in this region. Second, the model does not resolve the submesoscale which has been identified to sustain instabilities that promote a transport of the well-mixed bottom mixed layer waters away from the boundary and ultimately increase the stratification, and with this reduce the bottom mixed layer thickness (Naveira Garabato et al., 2019).

Observations of bottom mixed layer depths along the Antarctic margin are rare, but there exists a glider dataset from north of the Antarctic Peninsula, where there is an eastward slope current, that captures the bottom mixed layer (Ruan et al., 2017). The measurements match the model results in that the bottom mixed layer is thickening towards the lower slope. The observed maximum bottom mixed layer thickness of 250 m is less than in the model. The comparison holds when using Ruan et al. (2017)'s definition for the bottom mixed layer of a $\Delta 0.02$ kg m^{-3} density change, which results in an even deeper bottom mixed layer in the model (not shown). However, measurements at the lower slope (deeper than 1000 m), where the process model showed the thickest mixed layer depth, do not exist.

Another observation of a deep bottom mixed layer along the Antarctic continental slope originates from the Weddell Sea (Fer et al., 2016). Yet, the identified generation process in that case are internal tides, which have been neglected in the present study for reasons of simplicity. Internal tides are likely to release their energy near critical slopes (where the topographic slope equals the slope of an internal wave ray) and for the M2 constituent near the critical latitude (where the wave frequency equals the local inertial frequency). In the Weddell Sea, such conditions occur simultaneously and form bottom mixed layers at the continental slope of 100 m depth.

2.4.2 Implications

The formation of a deep bottom mixed layer has two implications for the type of ocean simulated in this study. Firstly, the bottom mixed layer in-

stabilities drive an intrinsic variability of the ASF that consists of short energetic events during which the water column becomes more stratified. The relaxation of the cross-slope density gradient goes along with a poleward transport of the relatively warm subsurface CDW. Stern et al. (2015) also investigate an aperiodic variability of an idealised slope jet in the high southern latitudes, but with an along-slope surface momentum stress in opposite direction to that of this study. Stern et al. (2015)'s results differ in that the jet becomes most unstable near the surface and subsequently drifts away in an offshore direction. Additionally, while the instability events are also of a mixed barotropic-baroclinic character, the onset of an instability event is connected to only baroclinic unstable conditions.

In this study, a threshold that might indicate the exact timing of an event was not found. However, the sensitivity analysis on the applied surface momentum stress revealed that the occurrence of the instability events responds to the strength of the wind-driven Ekman overturning. The result is in agreement with simulations performed by Nøst et al. (2011), which show larger overturning rates for a larger surface momentum stress (their Figure 14). A relationship between the Ekman overturning and the position of the maximum along-slope surface momentum stress is not expected (Stewart and Thompson, 2015). However, the buoyancy of the continental shelf water that is advected downslope should likewise have the potential to accelerate or decelerate the bottom mixed layer formation process (not tested, see also Section 2.4.3). If the observed freshening trend of continental shelf water (Schmidtko et al., 2014) continues, regions where DSW is formed today may end up with weaker or no DSW formation in the future, and be vulnerable for the intermittent instabilities to develop.

Observational evidence of the intermittent variability on interannual to decadal time scales does not exist as continuously measured time series from, for example, moorings cover typically up to three years and are therefore too short. A CTD-section from the Sabrina Coast at 120°E, East Antarctica, obtained during the BROKE campaign in austral summer 1996 though reveals a temperature snapshot (Bindoff et al., 2000; Williams et al., 2011, Figure 5 and Figure 2, respectively) similar to the modelled temperature distribution during the instability event of Figure 2.3d. Two existing measurements from

the continental slope at a similar longitude from 2007 (Williams et al., 2011) and 2015 (Nitsche et al., 2017) confirm the existence of CDW near the bottom at different years. The two observations, however, do not represent a full transect across the slope. The closest full transect across the slope is at 118°E from 2015, but it only covers the upper 700 m. It is therefore questionable to imply constant hydrographic conditions from the existing observations. A transect further downstream at 110°E, which was also obtained during the BROKE campaign in 1996, indicates that this part of the Antarctic coastline is characterised by steeply downward sloping isopycnals in an onshore direction (Bindoff et al., 2000; Williams et al., 2011, Figure 4 and Figure 2, respectively). The hydrographic conditions thereby match the situation modelled in the present study between two instability events. A CTD-section conducted in 2012 along 113°E confirms the strong temperature gradient across the shelf break with downward sloping isotherms at a different year (Peña-Molino et al., 2016).

Secondly, the findings contradict the hypothesis that all of the lower CDW is eventually converted into AABW as part of the lower overturning cell (Marshall and Speer, 2012). The strong vertical mixing in the boundary layer can lead to water mass transformation of the overlying water to a lighter density class. Observations from the Antarctic Peninsula show that such a water mass transformation is indeed active in the ocean (Ruan et al., 2017). The fact that the water mass can gain buoyancy away from the surface by enhanced bottom mixing suggests that significant amounts of deep water can be incorporated into CDW and be part of the Southern Ocean's upper overturning cell (Ruan et al., 2017).

2.4.3 Key parameters affecting the intrinsic variability

There are many physical and numerical parameters affecting the dynamics of the ASF that have not been explored in this study. A brief discussion of selected parameters that are most relevant to the problem is presented now. Firstly, the surface buoyancy forcing is important in setting the conditions for the continental shelf water that is critical for the development of a deep bottom mixed layer at the lower continental slope. The process model of the Antarctic continental shelf break developed here is similar to the model

setup by Stewart and Thompson (2015), but their model differs in that strong DSW production is prescribed on the continental shelf. In their case, near-bottom isopycnals shoal to the south due to the export of DSW down the continental slope, and strong bottom mixed layer instabilities are inhibited. Their finding is in agreement with baroclinic instability theory that predicts stable conditions (suppression of baroclinic instability) if isopycnals are parallel to the bottom slope (e.g. Isachsen, 2011; Pennel et al., 2012; Stewart and Thompson, 2013, 2016). However, for a case of weak DSW production, Stewart and Thompson (2015) observe an intrinsic variability of the ASF similar to the present study (Andrew Stewart, pers. comm.), supporting its physical robustness under the given boundary conditions.

Secondly, the slope of the continental shelf is critical for the topographic PV gradient that stabilises the along-slope flow (Figure 2.6a and Isachsen (2011)). The continental slope of the present domain is steep and therefore also able to maintain very steep isopycnals until baroclinic unstable conditions are met, manifested by the instability events. Less steep topographic slopes may allow instabilities to develop for less steep isopycnal slopes as well as closer to the continental shelf break, potentially leading to a larger onshore transport of CDW.

Thirdly, the intensity of the instability events varies according to the amount of energy that is resolved with the model grid. The intrinsic variability is found for all tested horizontal resolutions, but the change in along-slope velocity during an instability event decreases for a horizontal resolution of less than 3 km to approximately 50% (not shown).

Finally, energy is extracted from the system at the bottom, in the model facilitated by the applied quadratic bottom stress. Using a coarser horizontal grid resolution of 3 km, sensitivity tests of the quadratic bottom drag ($3 \cdot 10^{-4}$, $1.5 \cdot 10^{-3}$, $3 \cdot 10^{-3}$ (control run), $6 \cdot 10^{-3}$, and $3 \cdot 10^{-2}$) have been conducted to support this discussion on the effect of the bottom drag on the intrinsic variability of the ASF. For smaller bottom drags less energy is dissipated and the ASC consequently speeds up. The instability events are more intense and there is a tendency towards a longer period of time between two events. To analyse effect of the presence of submarine troughs on the development of the intrinsic variability was out of scope for this dis-

cussion. Numerical simulations by St-Laurent et al. (2013), however, suggest that troughs introduce a three dimensional circulation pattern that breaks up the zonally-symmetric configuration of the present domain. It would be interesting to test in future work the effect of a trough on the generation of a deep bottom mixed layer.

2.5 Concluding remarks

This study focussed on the dynamics of the ASF in an ocean process model for Antarctic continental shelves. Using instability theory, this study introduced a mixed barotropic-baroclinic instability of the ASF. A deep bottom mixed layer develops at the lower continental slope near the transition from sloping to flat bathymetry as a result of offshore bottom Ekman transport of relatively fresh continental shelf waters. The bottom mixed layer instabilities drive an intrinsic variability of the ASF. During instability events that last for approximately half a year, the stratification increases, which weakens the ASF and the associated barrier between the cold continental shelf and the warmer CDW offshore.

The deep bottom mixed layer is a region of EKE production. High eddy activity and related onshore heat transport has so far only been connected to regions with elongated bathymetric features (St-Laurent et al., 2013; Daae et al., 2017) or where the export of dense bottom water drives an interior return flow (e.g. Thompson et al., 2014; Stewart and Thompson, 2015). The mechanism discussed in this study, however, could be active in vast areas of the continental shelf around Antarctica where neither of the other two dominate.

To conclude, the intrinsic variability is a robust feature in the simulations, but warrants further investigation regarding the degree to which the mechanism changes in a submesoscale regime or is captured in realistic models, and regarding to how it translates to the ocean. Observations from the entire continental slope from shelf break to deep ocean would be valuable in order to confirm the maintenance of very steep isopycnals at the slope over several years.

Chapter 3

Sensitivity of the Antarctic Slope Front to mechanical and buoyancy forcing

The previous chapter focused on the fresh continental shelf case. It discussed the development of a deep bottom mixed layer that forms under such conditions at the lower Antarctic continental slope. This triggers an intrinsic variability of the ASF which allows relatively warm CDW to move temporally closer to the continental shelf break. Chapter 3 adds some complexity to the process model by employing a seasonal signal to the forcing, by having a lateral border to the ice shelf embayment, and most of all by applying a range of different combinations of mechanical and buoyancy forcing at the surface. As a result of the varying surface forcing, the shape of the ASF changes. The relative ratio between the applied buoyancy and mechanical forcing is used to define the thresholds between the ASF regimes.

Abstract

The ASF has an almost circum-Antarctic extent. However, the frontal structure, and with it its ability to maintain a barrier between the colder continental shelf waters and the warmer Southern Ocean, varies around the coastline. Recent process studies have focused on the leading-order mechanisms responsible for cross-shelf heat transport for various frontal regimes. The precise role of mechanical forcing (by a combination of wind stress and sea ice movement) and buoyancy forcing in setting the shape of the ASF is less understood. This study performs sensitivity experiments with an ocean

process model to explore the respective contribution. The ratio of buoyancy forcing on the continental shelf relative to the mechanical forcing is used to classify different regimes and their thresholds. The experiments reveal that the double-sided ASF, a regime that has been repeatedly observed, is very sensitive to the surface forcing and may be a transient feature between a fresh and a dense continental shelf. Furthermore, the response time of the ASF to changes in the surface forcing is faster for the onset of a polynya than vice versa. With regard to the local freshening trend of Antarctic continental shelf waters in the Ross and western Weddell Seas, the findings suggests a rather slow deviation of the present-day dense-shelf regime to a fresh-shelf regime and towards larger cross-slope density gradients in the decades to come.

3.1 Introduction

The ASF regulates onshore heat transport to the Antarctic coastline leading to basal melting of the floating ice shelves (e.g. review by Thompson et al., 2018), affecting sea ice formation, and setting local water mass formation (e.g. Gill, 1973). All of these processes have global importance and highlight the key role of the ASF for the climate system. The shape of the ASF, and with it the separation of the colder continental shelf waters from the warmer CDW residing at mid-depth in the Southern Ocean, however, varies along the Antarctic coastline (Jacobs, 1991; Thompson et al., 2018). Unveiling the role of atmospheric forcing for the different shapes of the ASF and their sensitivity to a future climate is the objective of this study.

The ASF can be connected to a broad, generally westward flowing current, the ASC. Here, the ASC is defined as the slope jet that follows the Antarctic continental shelf break. At wider continental shelves, such as at the Weddell Sea, a second jet has been observed that follows the ice shelf front and is referred to as the ACoC (Jacobs, 1991; Heywood et al., 2004). The ASC is observed to be surface intensified, but undercurrents which are decoupled from the surface jet, can occur near the bottom (Heywood et al., 1999; Peña-Molino et al., 2016). The ASC is strongly guided by potential vorticity constraints and therefore follows constant values of f/H (f is the

Coriolis parameter and H is the water column depth), limiting markedly cross-slope flow and with it cross-slope heat transport. An increasing number of observational and modelling studies agree in that heat transport across the Antarctic continental slope is facilitated by (i) local troughs that channel warm water onto the continental shelf (Klinck and Dinniman, 2010; Schodlok et al., 2012; St-Laurent et al., 2013; De Rydt et al., 2014; Daae et al., 2017), (ii) eddy activity (Nøst et al., 2011; Hattermann et al., 2014; Stewart and Thompson, 2015, 2016; Graham et al., 2016; Azaneu et al., 2017), as well as (iii) residual tidal flow (Stewart et al., 2018).

These potential mechanisms may act together or separately and vary with the shape of the ASF. Following the findings of Stewart and Thompson (2015, 2016), the working hypothesis is as follows: The deflection of the isopycnals from the horizontal, which manifests the shape of the ASF, is controlled by the interplay between mechanical surface forcing (by a combination of wind stress and sea ice movement) and buoyancy forcing. Coastal Easterlies provoke onshore Ekman transport and downwelling which deepens the isopycnals in an onshore direction. The loss of buoyancy on the continental shelf, on the other hand, causes the isopycnals to shallow in an onshore direction. As a result, buoyancy adds APE to the system while eddies and surface stresses act to remove APE. The relative contribution of the two determines the isopycnal shape. Four different regimes are conceivable and are illustrated in Figure 3.1:

(i) No front. Both the mechanical and the buoyancy forces are either weak or cancelling each other out so that the isopycnals predominantly align with the horizontal. Due to the absence of a slope front, onshore heat transport is solely a function of thermocline depth relative to the continental shelf (Dutrieux, 2014) and possibly weak eddy mixing that acts to homogenise PV. This is true for the Bellingshausen Sea in West Antarctica, where the relatively warm CDW (or a modified version of it) flushes the continental shelf. Here, the continental shelf temperatures mirror the signal of the southward shifting ACC and with it of the relatively warm CDW (Schmidtko et al., 2014). As a response to the warming shelf waters, basal melt rates of West Antarctic ice shelves have increased resulting in their thinning and retreat

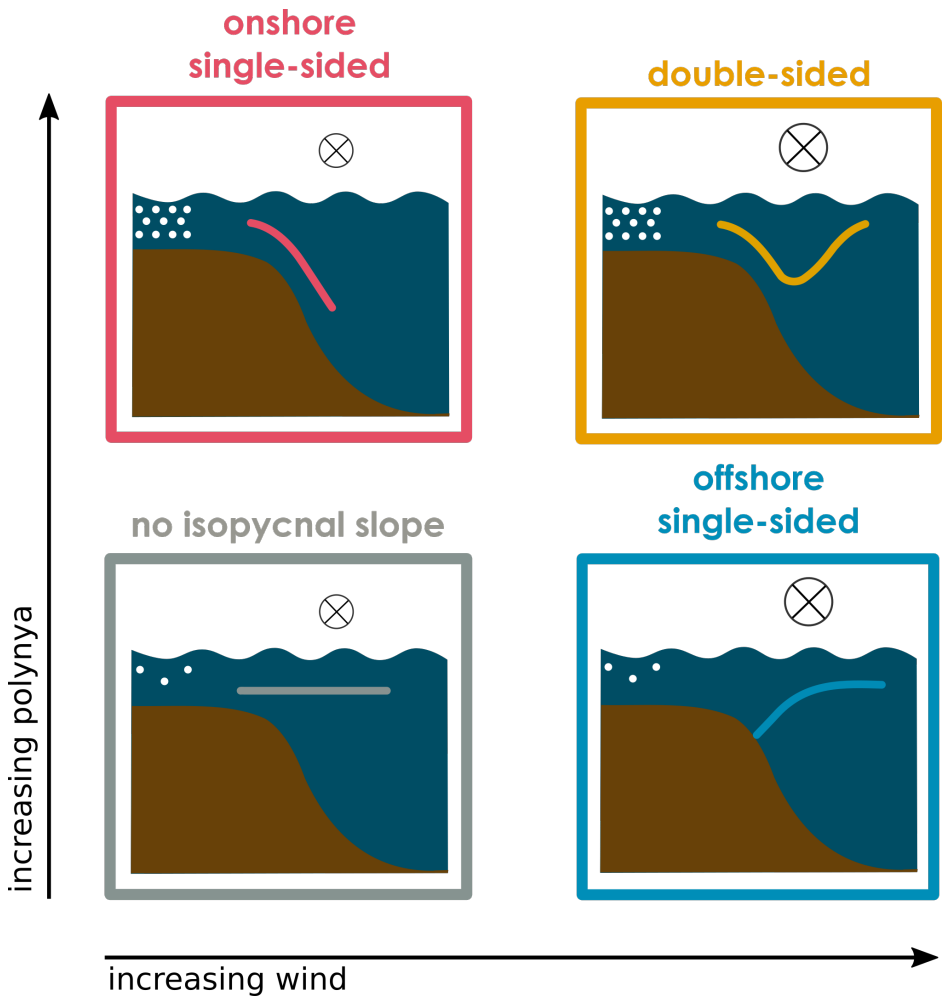

Figure 3.1: Schematic of four different ASF regimes with a varying cross-slope shape of the isopycnals (coloured line). White dots indicate the amount of brine rejection on the continental shelf and with this the buoyancy forcing in the polynya region. The cross denotes the dominant wind direction oriented such that the shallow Antarctic continental shelf is to its left (into the page). The size of the cross translates to the wind speed.

(Pritchard et al., 2012).

(ii) Offshore single-sided front. The isopycnals deepen in an onshore direction due to coastal Ekman convergences created by the dominating easterlies. The offshore single-sided ASF is typical for regions with no or only weak AABW formation as a result of little DSW production and export, such as most of the coastline in East Antarctica (Bindoff et al., 2000; Peña-Molino

et al., 2016; Thompson et al., 2018). The downsloping isopycnals of the ASF are very effective in protecting the continental shelf and marine terminating Antarctic glaciers from the CDW. The ASC in this regime is very stable and inhibits cross-slope heat transport. Continental shelves in East Antarctica are hence cold and basal melt rates are comparably small (Pritchard et al., 2012; Rignot et al., 2013). Noticeable onshore heat transport is confined to areas with submarine troughs (Nitsche et al., 2017).

(iii) Double-sided front. The increase of APE input due to buoyancy loss (salt input) on the continental shelf results in a second, onshore branch with isopycnals that shoal to the south. The double-sided ASF is often described as a "V-shape" with a freshwater lens in between (Gill, 1973; Jacobs, 1991). It occurs in regions of AABW formation such as at the Weddell Sea, the Ross Sea, and near Prydz Bay and is with this a unique feature to the polar continental shelf breaks (Thompson et al., 2018). Eddies that are primarily sourced from baroclinic instabilities at the AABW/CDW interface dissipate much of the APE input and the increase of the eddy-driven overturning enhances onshore heat transport in the subsurface (Stewart and Thompson, 2015, 2016). Ice shelf cavities could be subject to modified CDW intrusions.

(iv) Onshore single-sided front. Isopycnals shoal to the south and deepen to the north when the buoyancy loss dominates and only the shoreward side of the slope front remains. The mechanical forcing is not strong enough to release the APE and to deepen the isopycnals as in the case of (ii) and (iii). This regime has so far not been described for the ASF, but as will be argued in Section 3.4.2, could possibly exist at regions of enhanced AABW formation.

This chapter investigates the sensitivity of the ASF on the surface forcing. It defines thresholds between the different regimes, as a lack of understanding has been highlighted in a recent review by Thompson et al. (2018). The results will contribute to the identification of susceptible regions and promote the question of how the ASF, and hence cross-slope heat transport, will potentially change in a future climate. A process model of the Antarctic

continental shelf break is used to perform a set of experiments with varying combinations of mechanical and buoyancy forcing. The different ASF regimes will be analysed with a focus on the density structure, the associated slope jet and basal melt rates, as well as their temporal variability.

3.2 Experimental design

In order to eliminate other local environmental factors such as a varying geometry along the coastline, the sensitivity experiments are conducted using a numerical ocean model on an idealised domain (Figure 3.2). The model configuration is the same as in Chapter 2 with three differences: (i) a laterally bounded ice shelf, (ii) a seasonal surface forcing, and (iii) a horizontal grid resolution of 2 km. St-Laurent et al. (2013), Stewart and Thompson (2015), and Appendix A.2 show that to resolve mesoscale features in the study region requires a horizontal resolution of 1 km. The present resolution captures only 85% the eddy kinetic energy of the 1 km grid used in Chapter 2, but computational expenses for the full set of experiments in this study inhibit a higher resolution.

The experiments comprise a suite of different combinations of mechanical forcing and buoyancy forcing (in a polynya) with a focus on the latter (Table 3.1). Each experiment is spun-up for 30 years using a coarser resolution of 4 km. The output is then interpolated onto the 2 km grid and the model run for an additional 15 years. Monthly output for the last 10 years are presented in the result section. In addition to the equilibrated experiments, two transient experiments (P100P-16 and P-16P100) investigate the temporal response of the density structure to changes in surface forcing. Experiment P-16P100 (P100P-16) is initialised using the final state of the weakest polynya experiment W100P-16 (strongest polynya experiment W100P100), but has the surface forcing of the strongest polynya experiment W100P100 (weakest polynya experiment W100P-16).

The seasonality is introduced via the applied surface momentum stress and buoyancy fluxes. Each model year consists of 360 days with a summer (60 d), followed by autumn (90 d), winter (120 d), and spring (90 d) (Figure 3.3). The momentum stress profiles for the along-slope and cross-

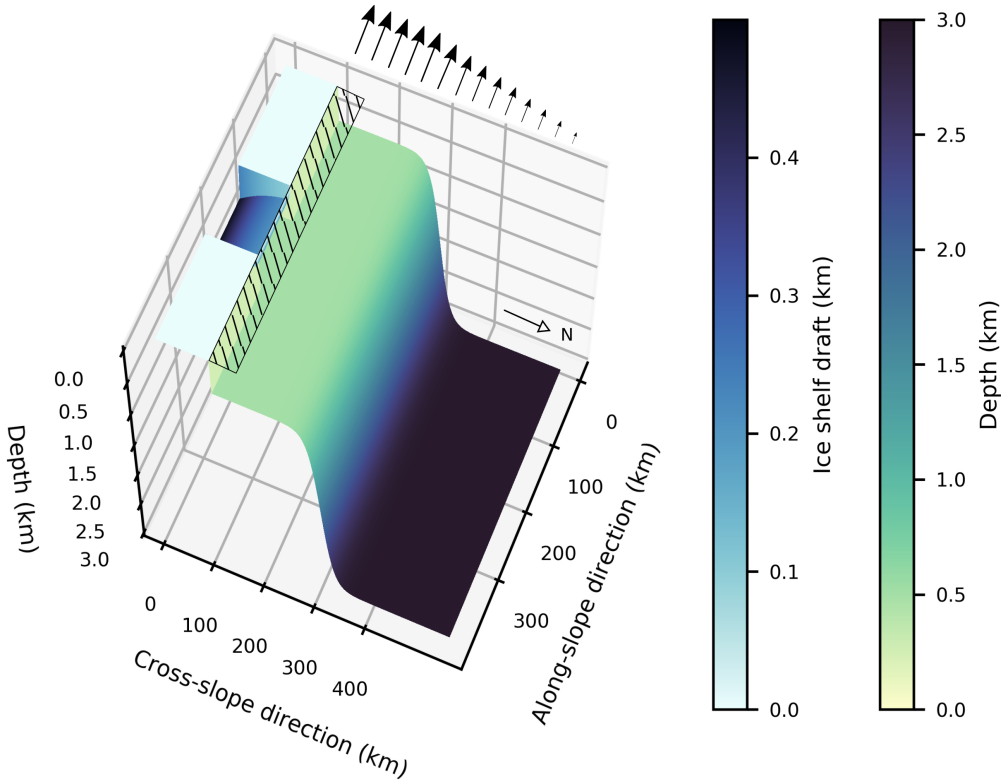

Figure 3.2: Geometry of the idealised Antarctic continental shelf break. The hatched area in front the ice shelf/coastline shows the polynya region. The arrows at the top indicate the applied along-slope wind profile.

slope components represent the mechanical forcing and increase linearly from summer time to winter by a third (Figure 3.3a and 3.3b). The experiments use a range of summer values for along-slope surface momentum stress on the continental shelf: 0.025 N m^{-2} (50%), 0.05 N m^{-2} (100%), and 0.1 N m^{-2} (200%) (Table 3.1, columns). The surface momentum stress accounts for the combined effect of direct atmosphere-ocean momentum transfer and atmosphere-sea ice-ocean momentum transfer, and must therefore not be equated with wind stress only, but the chosen profiles are representative of the expected surface stress due to winds.

Similarly, because the model is not coupled to a sea ice component, the buoyancy fluxes mimic the combined effect of direct atmosphere-ocean

Table 3.1: Overview of sensitivity experiments. The polynya activity is controlled by changing the relaxation time scale as indicated by t_{relax}. The names consist of the mechanical forcing (W as for "wind", in percent) and the polynya activity (P, in percent). The ratio r between polynya activity and mechanical forcing for each experiment is the value in brackets (using the percentage of each forcing), see text for more explanation. The experiments in the lower two columns have both a mechanical forcing of 100%, but the buoyancy forcing is swapped. The polynya activity changes from 100% to -16% (P100P-16) and from -16% to 100% (P-16P100).

t_{relax}	polynya activity	mech. forc. 0.025 N m^{-2} 50%	mech. forc. 0.5 N m^{-2} 100%	mech. forc. 0.1 N m^{-2} 200%
1 d	100%	W50P100 (2.0)	W100P100 (1.0)	W200P100 (0.5)
2.5 d	53%		W100P53 (0.53)	
5 d	45%	W50P45 (0.9)	W100P45 (0.45)	W200P45 (0.225)
10 d	1%		W100P1 (0.01)	
20 d	-16%		W100P-16 (-0.16)	
1 d $\rightarrow$ 20 d	100% $\rightarrow$ -16%		P100P-16	
20 d $\rightarrow$ 1 d	-16% $\rightarrow$ 100%		P-16P100	

interaction as well as sea ice-ocean interaction. The intention is to represent primarily the heat loss and brine rejection that occur in polynyas. During summer, the entire surface is subject to a constant freshwater flux (-10^{-6} psu m s^{-1}) and a temperature relaxation to -1.0°C allowing the surface ocean to stratify. During autumn, winter, and spring, the surface ocean divides into an "open ocean" and a "polynya" region. The polynya covers 50 km along the southern end of the continental shelf (hatched area in Figure 3.2). During this time of the year, the freshwater flux is set to zero in the open ocean, but can be non-zero in the polynya region if the surface temperature is close to the surface freezing point (colder than -1.8°C for the equilibrated experiments and -1.7°C for the transient experiments P-16P100 and P100P-16) and with this represents brine rejection during sea ice growth. The salinity relaxation value is 35 psu in winter and varies between 34 psu and 35 psu in autumn and spring (Figure 3.3c, solid blue line). The temperature is relaxed to either -1.85°C (open ocean region) or -1.9°C (polynya region) to approximate the freezing temperature (Figure 3.3c, red line). The

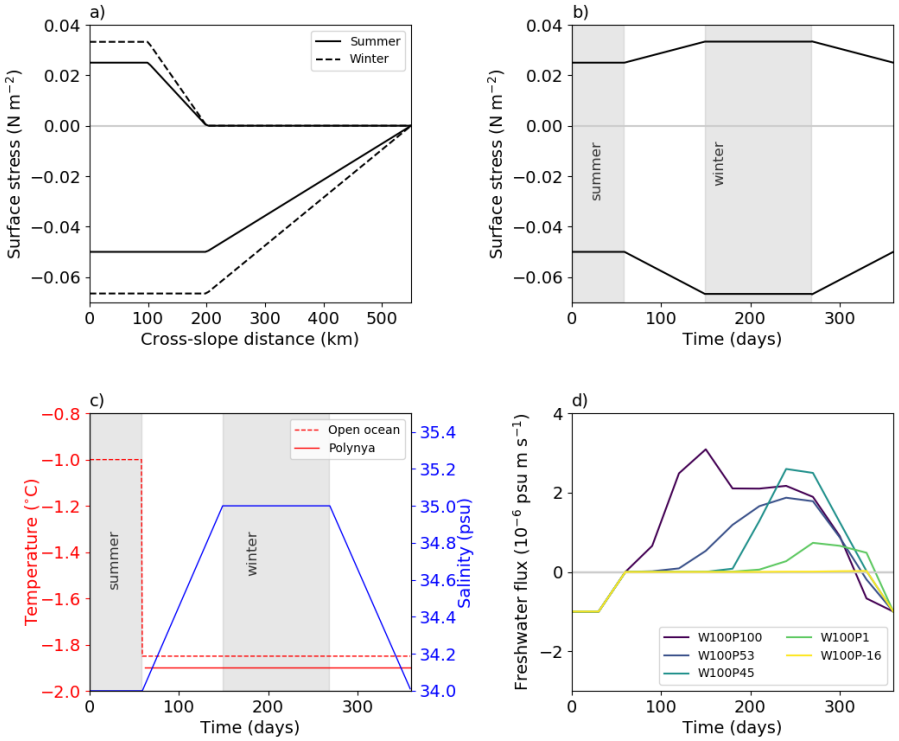

Figure 3.3: a) Cross-slope (positive) and along-slope (negative) surface momentum stress as a function of cross-slope distance for summer (solid) and winter (dashed). b) Seasonal cycle of cross-slope (positive) and along-slope (negative) surface momentum stress at 100 km from the southern boundary. c) Seasonal cycle of temperature and salinity relaxation values in the polynya region (solid) and in the open ocean (dashed, for temperature only). d) Area-averaged freshwater flux in the polynya region (positive: increase in salinity, negative: freshening) for five experiments with constant wind forcing, but different polynya activity. Shown is the last year of the model run (year 14). The yearly integrated salt flux is used to express the polynya forcing in percent for each experiment, where the W100P100 is defined as 100%.

water mass produced in the polynya region during winter is the densest in the domain and results locally in convection to the seafloor.

The relaxation time scale is the same for temperature and salinity, but varies accordingly to the respective sensitivity experiment in the polynya region (Table 3.1, first column). Five experiments test the sensitivity for

relaxation time scales between 20 days (same as in the open ocean region) and 1 day. The smaller the relaxation time scale is, the larger is the resulting buoyancy flux and with this the modelled polynya activity. Figure 3.3d shows the seasonal freshwater flux for each polynya sensitivity experiment as a proxy for the actual buoyancy flux[1].

The polynya activity is for the remainder of the study expressed in percentage, where the W100P100 experiment with a relaxation time scale of 1 day is defined as 100%. This way, the effect of mechanical and buoyancy forcing can both be expressed by relative changes. The result section makes use of this by employing a non-dimensional ratio r, where r = polynya activity/mechanical forcing, in order to express the relative contribution of the surface forcing for the development of different isopycnal slopes. Note that r allows only a qualitative description of the occurring changes as it compares the forcing parameters rather than physical processes.

3.3 Results

3.3.1 Modelled regimes of the ASF

Annual averages of along-slope velocity and density for the full set of sensitivity experiments are considered first (Figure 3.4). A comparison of the modelled ASF with Figure 3.1 allows a classification of the former into three groups, namely the onshore single-sided front (W50P100, W100P100), no front (W200P100, W100P53, W50P45), and the offshore single-sided front (W100P45, W200P45, W100P1, W100P-16). The double-sided front schematically shown in Figure 3.1 is not reproduced in the steady state simulations.

The onshore single-sided front occurs for a strong polynya with a polynya to mechanical forcing ratio of $r \geq 1$ (Table 3.1, number in brackets, and

[1]Following Cerovečki et al. (2011), the total buoyancy flux B is the sum of a heat and freshwater component B_{H} and B_{FW} and can be calculated as

$$B = B_{\mathrm{HF}} + B_{\mathrm{FW}} = \frac{g}{\rho_0}\left[\frac{\alpha Q_{\mathrm{HF}}}{c_p} - \rho_0 \beta S(E-P)\right],$$

where $\alpha = \frac{1}{\rho}\frac{\partial \rho}{\partial T}$ and $\beta = \frac{1}{\rho}\frac{\partial \rho}{\partial S}$ are the thermal expansion and saline contraction coefficients, Q_{HF} is the net heat flux (in W m^{-2}), and $S(E-P)$ with evaporation E and precipitation P is the freshwater flux (in psu m s^{-1}) as given by ROMS.

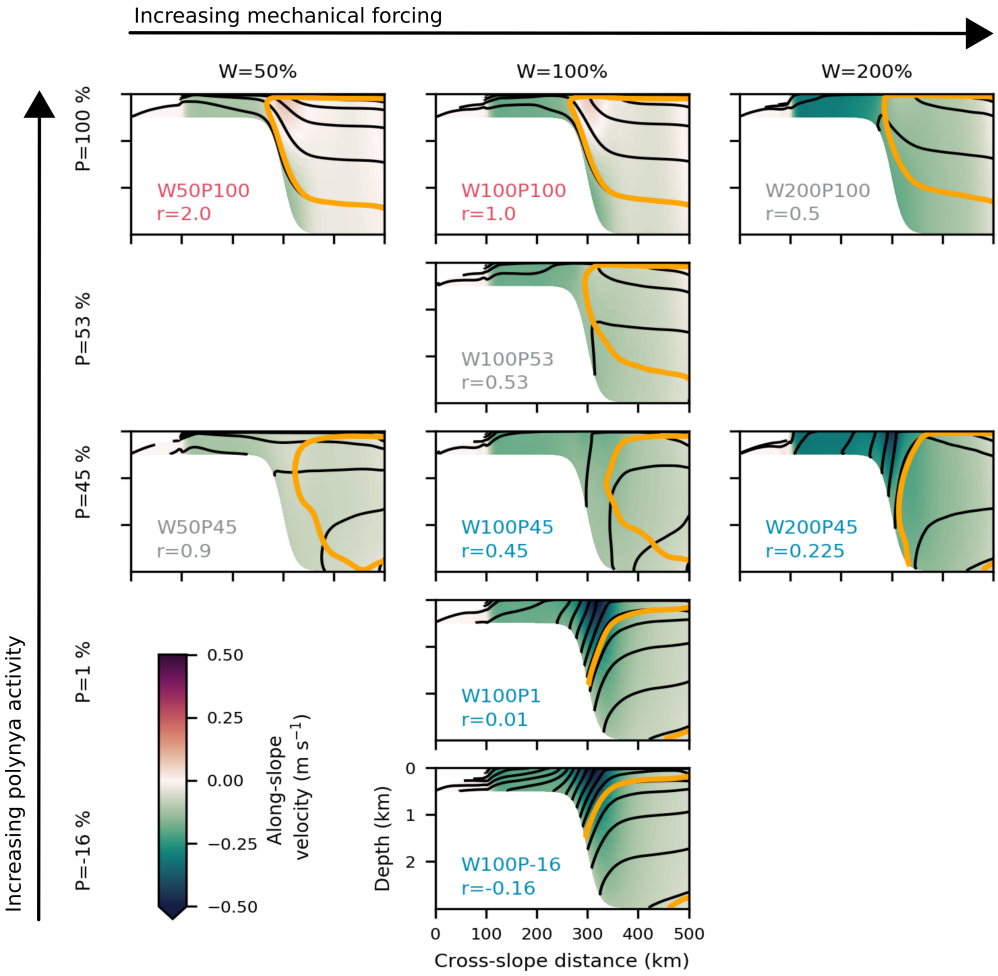

Figure 3.4: Ten-year averaged along-slope velocity field for all sensitivity experiments as listed in Table 3.1. The experiment names are given in the bottom left corner of each panel and are colour-coded accordingly to the shape of the isopycnals as defined in Figure 3.1. Mechanical forcing increases from left to right and polynya activity increases from bottom to top. Green shaded water flows into the page (shallow continental shelf on its left) and red shaded water flows out of the page (shallow continental shelf on its right). Black contours indicate lines of constant density (σ_{500}) with 0.05 kg m^{-3} increments and the yellow line shows the 0°C-temperature contour.

Figure 3.4). The large buoyancy flux in the polynya region increases the density on the continental shelf, forming a positive density gradient in an onshore direction. The density field changes the hydrostatic pressure and supports a geostrophic current in the order of 0.1 m s^{-1} that is oriented to

the east and thus opposite to the effect of the mechanical forcing (such an eastward slope current also exists when the winds are turned off, not shown). The density field and surface Ekman transport work against each other, thus the weaker the mechanical forcing the stronger the eastward current. Additionally, a westward undercurrent appears at the lower slope, which originates from DSW that moves down the continental slope and is deflected to the west by the Coriolis force.

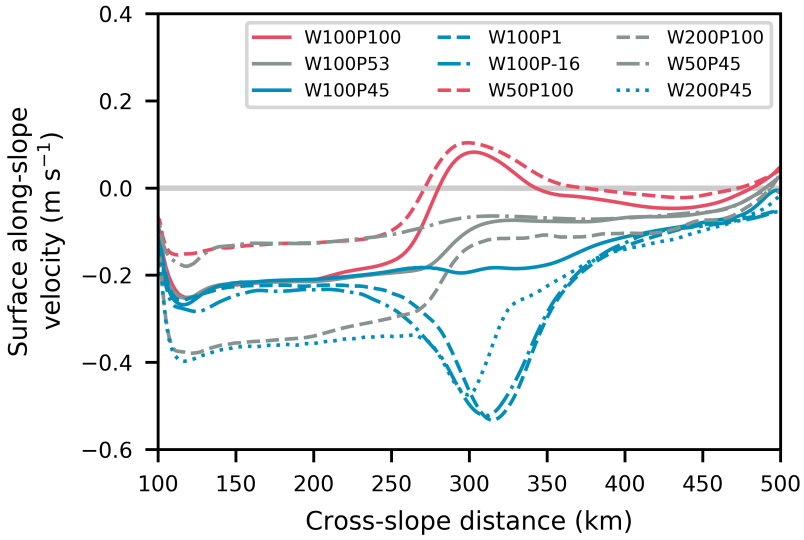

Figure 3.5: Along-slope mean and time mean of surface along-slope velocity as a function of cross-slope distance. Colour-coding follows the classification of Figure 3.1.

When the mechanical and buoyancy forcing cancel each other the isopycnals are almost horizontal and the front ceases (Figure 3.1 and Figure 3.4). The no-front regime exists in multiple states with a polynya to mechanical force ratio between $0.5 \leq r < 1$. An increase in polynya activity requires an increase in surface stress in order to maintain the no-front regime, and the experiments hence align on a diagonal in Figure 3.4. There is no slope jet, but a general westward flow that mirrors the applied surface stress profile and drops at the shelf break.

The offshore single-sided ASF appears when the mechanical forcing increasingly dominates over buoyancy (polynya to mechanical forcing ratio of

$r < 0.5$). This frontal shape occurs for the sensitivity experiments located in the bottom right corner of Figure 3.4. The velocity field shows the typical surface-intensified jet structure at the continental slope (see also Figure 3.5). Experiment W100P1 and W100P-16 show the fastest velocities of -0.5 m s^{-1} and their velocity maximum is shifted approximately 20 km offshore compared to W200P45. The experiment W100P45 is at the threshold between the offshore single-sided front and no front (polynya to mechanical forcing ratio of $r = 0.45$). It shows downsloping isopycnals in an onshore direction, but the velocity field exhibits neither an acceleration nor deceleration at the continental slope (Figure 3.5).

Sensitivity to polynya activity

Shown in the left panels of Figure 3.6 are the five polynya sensitivity experiments with 100% mechanical forcing (W100P100, W100P53, W100P45, W100P1, W100P-16). The experiments capture the three ASF shapes previously discussed. These shapes vary from the offshore single-sided front, to no front, to the onshore single-sided front from a weak to a strong polynya.

The surface velocities reveal a strong sensitivity to the polynya activity, but do not mirror the regime behaviour. The weaker the buoyancy flux in the polynya region, the faster the westward jet (Figure 3.6a). The jet accelerates because coastal Ekman convergence driven by the surface stress is the only force creating a cross-slope pressure gradient that subsequently leads to a geostrophic current. For increasing polynya activity, the surface pressure gradient changes (not shown) and the jet weakens and eventually reverses (flowing eastward) for the W100P100 experiment. Be aware that the maximum velocity might vary due to a shift in the jet position (compare Figure 3.5).

Figure 3.6c shows the depth-mean temperature at the continental shelf break (250 km from the southern boundary). Unlike for the slope jet, the continental shelf break temperature does not follow a continuous increase with a more active polynya. The temperatures are low (less than 0.2 °C above surface freezing point) for all but the onshore single-sided regime (W100P100). The density structure of the latter allows a connection of the water masses across the continental slope enabling eddies to mix heat along isopycnals

(high eddy kinetic energy, not shown). The 0°C-temperature contour in yellow in Figure 3.4 shows correspondingly an onshore deflection near the shelf break. For the no-front regime a similar pattern could be expected, but the absence of eddy kinetic energy inhibits significant onshore heat transport (not shown). The cold temperatures in the offshore single-sided simulations demonstrate the strong dynamical barrier that the slope front represents.

The stratification at the continental shelf break varies with the changing polynya activity (density contours of Figure 3.4, middle panels). The weak polynya experiments (W100P-16, W100P1) have the highest stratification due to strong buoyancy gain in summer and no buoyancy loss in winter. The weakest stratification occurs when winter buoyancy loss equals the summer buoyancy gain (W100P45, W100P53). The stratification increases with a stronger polynya as dense water export enhances the near-bottom stratification.

Figure 3.6e investigates the sensitivity of basal melting in the ice shelf cavity to the applied buoyancy flux in the polynya area. All melt rates are low as cavity temperatures never exceed more than 0.25°C above the local freezing point (not shown). This means that the cavity is always in the "cold regime" (or "mode 1" following Jacobs et al. (1992) and Silvano et al. (2016)) no matter the polynya activity and frontal shape. The process model seems to miss a mechanism for enhanced onshore transport of modified CDW into the cavity. Likely, this is because the domain does not have a submarine trough that connects the cavity with the Southern Ocean, the continental shelf is flat rather than retrograde, and the polynya covers the entire domain preventing an asymmetry of the inflow/outflow circulation on the continental shelf.

Being always a cold cavity, the melt rate is not a function of the cross-shelf heat transport and therefore cannot be related to a specific shape of the ASF. Instead, it depends on the cavity circulation itself, and the DSW characteristics which are set in the polynya in front of the ice shelf (Jacobs et al., 1992). The dense DSW sinks and spreads out into the cavity and towards the shelf break. Therefore, melt rates are low, but increase with a more active polynya and cavity circulation. In agreement with other modelling studies (e.g. Gwyther et al., 2014; Naughten et al., 2018a) and observations (Jacobs

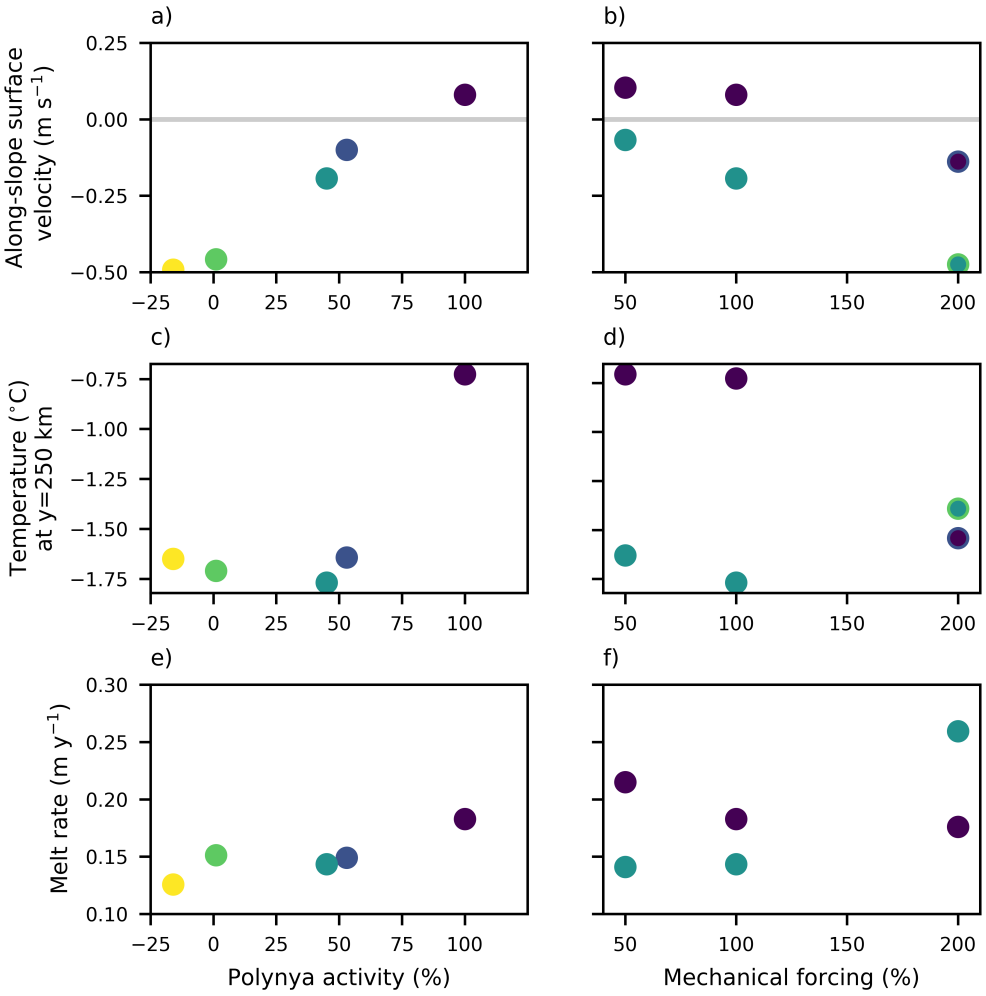

Figure 3.6: Experiments testing the sensitivity on polynya activity (left) and wind intensity (right) for a), b) along-slope surface velocity at 300 km from the southern boundary, c), d) depth-mean temperature at 250 km from the southern boundary, and e), f) melt rate in the ice shelf cavity. Colours indicate the polynya activity following the colour coding of Figure 3.1. Left panels show the sensitivity to polynya activity for a 100% wind forcing. Right panels show the sensitivity to a varying wind intensity for 100% (purple) and 45% (turquoise) polynya activities..

et al., 1992; Rignot et al., 2013), the melt rates in the process model are highest near the grounding line (not shown).

Sensitivity to mechanical forcing

The sensitivity on the mechanical forcing is tested for two polynya activities (right panels of Figure 3.6). The strong polynya experiments (100%, purple) incorporate the ASF regime shift from an onshore single-sided front (W50P100, W100P100) with an eastward flow (Figure 3.6b, positive values) to no front (W200P100) with a westward flow (Figure 3.6b, negative values). The experiments with a weaker polynya (45%, turquoise) show a much more linear relationship and a higher amplitude between the simulations with the weakest and strongest mechanical forcing (W50P45, W100P45, W200P45).

The temperature at the continental shelf break clearly reflects the regime behaviour in the 100% polynya experiments (Figure 3.6d). The temperatures are highest for the onshore single-sided ASF and drop for the strong-mechanical forcing experiment (W200P100). The pattern is less obvious for the 45% polynya experiments. Here, the temperatures are all below -1.4 °C (less than 0.5°C above surface freezing point) and are highest for the strong-mechanical forcing experiment which exhibits the largest values of EKE (not shown).

Similar to the surface velocity, the sensitivity of the melt rate to mechanical forcing differs for the background polynya activity (Figure 3.6f). The strong polynya simulations show a decrease of the melt rate with increasing mechanical forcing. An explanation for this might either be the increase in the kinetic energy on the continental shelf itself (not shown) or the stronger dynamical barrier of the ASF at the continental slope. The simulations with a weaker polynya show a very different sensitivity. While the melt rates of experiments W50P45 and W100P45 are insensitive to the surface stress, experiment W200P45 has the highest melt rates of all simulations. The higher melt rates are mainly driven by warmer cavity temperatures and a stronger cavity circulation that allows for a replenishment of the meltwater. Note again that the simulations are always in a cold regime and that melt rates are low. The simulations therefore do not show a strong sensitivity to meltwater.

3.3.2 Temporal variability

The temporal variability varies qualitatively for the different ASF shapes. Figure 3.7 shows, representative for the different regimes, the time evolution of surface velocity for the polynya sensitivity experiments. The mean value for each experiment corresponds with Figure 3.6a. A seasonal signal appears for each of the westward flowing slope jets with a consistent drop in summer to 88% of the maximum winter value. This result implies that the mechanical forcing is the major driver of ASF seasonality in the idealised simulations and that the varying buoyancy flux in the polynya region throughout a year is subservient (Figure 3.3d). In fact, the hydrography shows an increase in summer-time surface stratification in the upper 100 m only (not shown). The slope of the isopycnals, and with it the shape of the ASF, consequently hardly changes within a year. Note, that the mechanical forcing drops from winter to summer by 75%, hence the response in the surface velocity is attenuated by 88%.

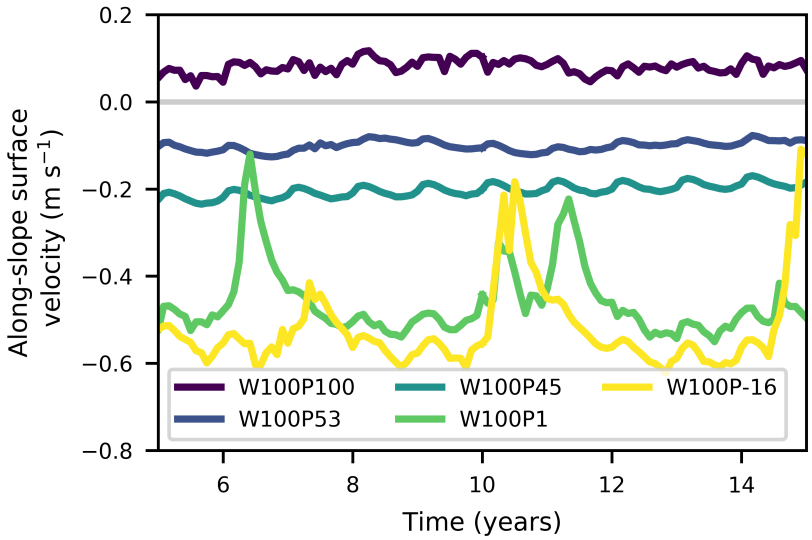

Figure 3.7: Time series of the along-slope surface velocity at 300 km from the southern boundary for the five sensitivity simulations with 100% wind forcing.

The experiments W100P53 and W100P45 are examples for a weak westward slope jet and manifest a seasonal variability only. Additionally to the

seasonal cycle, a non-periodic intrinsic variability occurs approximately every 5 years for the simulations with a fresher continental shelf and stronger westward flowing jets (W100P1, W100P-16). This mode of variability is the same as described in Chapter 2. It originates from relatively buoyant shelf water that is transported down the continental slope by Ekman dynamics. The shelf water destabilises the near-bottom water column at the lower slope resulting in elevated vertical mixing that eventually leads to a strong instability event that re-stratifies the entire water column.

A non-periodic variability on shorter time scales (weeks to months) dominates the eastward slope jet (W100P100). With this, the ASC shows a very different behaviour compared to the other simulations, where seasonal to interannual variability supersedes any high-frequency variability. Likely, these instabilities originate from the opposing mechanical and buoyancy forces acting on the ocean.

Additionally, an ACoC develops in summer for all experiments but W100P-16 (not shown). The geostrophic current is driven by a strong density gradient with low salinity surface water in the polynya region and denser surface water farther on the continental shelf. The density gradient during summer emerges due to the export of fresh meltwater from the ice shelf cavity (the melt rate increases in summer because the produced DSW is warmer) and due to buoyancy gain from the applied surfaced fluxes.

3.3.3 Transient double-sided ASF

The original set of experiments does not reproduce the double-sided ASF (Table 3.1 and Figure 3.4) although observations suggest its existence (see review by Thompson et al. (2018) and citations within). The findings of the process model indicate that the formation of the double-sided ASF only occurs under particular surface forcings. In order to show that the double-sided ASF exists as a transient feature, two additional experiments with a swapped surface forcing are now presented (initial state of weakest/strongest polynya and surface forcing of strongest/weakest polynya (P-16P100/P100P-16)). These experiments represent a transient in time in the model, but translate in the Lagrangian framework to water that flows along a coastline with changing conditions.

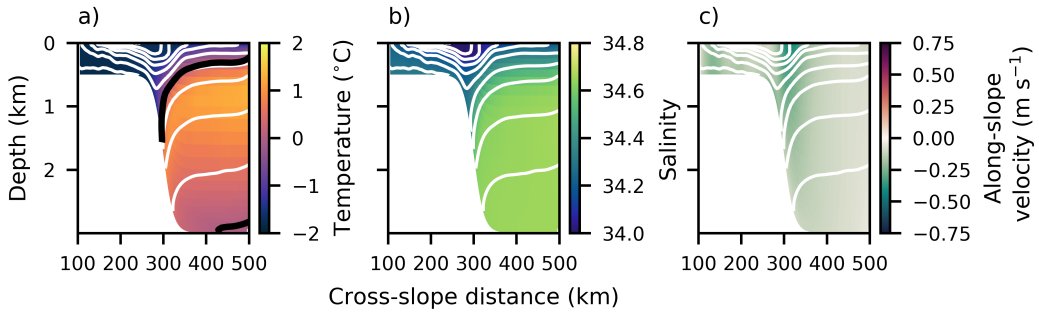

Figure 3.8: Snapshot of a) temperature, b) salinity, and c) along-slope velocity (shading) with σ_{500}-contours (white) and 0°C-contour (black) after 13 months for experiment P-16P100.

Figure 3.8 shows a snapshot in time of temperature, salinity, and the along-slope velocity field together with potential density contours of the P-16P100 simulation after 13 months. The experiment commences with an offshore single-sided front (fresh continental shelf) and concludes with an onshore single-sided front (dense continental shelf). The isopycnals in Figure 3.8 depict the double-sided ASF as a transient feature that will last for another 2.5 years before the frontal shape changes to the onshore single-sided front. The isopycnals close to the continental shelf shoal as a result of AABW formation due to increased buoyancy loss in the polynya region. The surface stress is sufficient to deepen the isopycnals in an onshore direction farther offshore, creating the double-sided ASF with a characteristic local salinity minimum at the surface (Figure 3.8b). The deep Southern Ocean is still unaffected and has not yet reacted to the changes in the surface forcing. Eventually, the density increase throughout the water column on the continental shelf dominates and leads to the transition to an onshore single-sided ASF. The fact that the double-sided ASF occurs first after 13 months explains why this regime is not captured as a seasonal feature in one of the steady-state experiments.

The ASC is westward flowing when the double-sided ASF first occurs (Figure 3.8c), but then starts to weaken and to move offshore (Figure 3.9a). Simultaneously, the onshore upwards sloping isopycnals strengthen and an eastward jet develops close to the shelf break that eventually replaces the westward jet (Figure 3.9a). The cross-slope distance between the final posi-

tion of the maximum velocities of the eastward and westward ASC is 65 km (Figure 3.9a, black scatter points). The jet disturbance just after the change of the surface forcing at year 15 is one of the intermittent instability events discussed in Chapter 2 that occurs at this moment, and is independent of the change in the applied surface forcing.

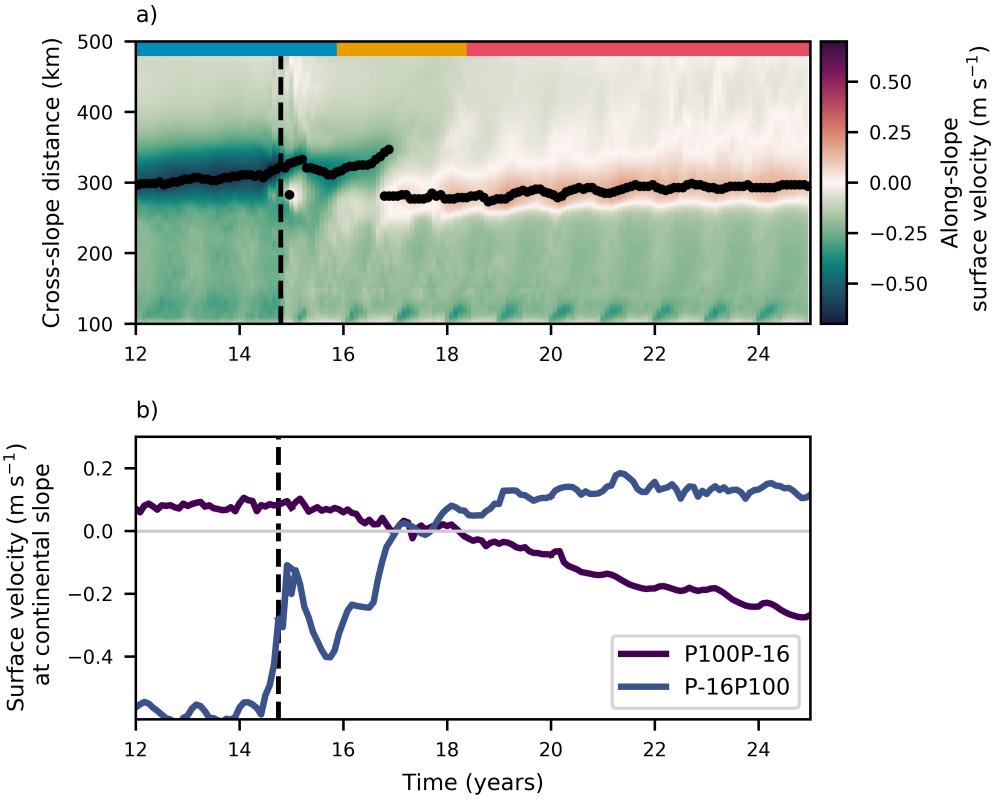

Figure 3.9: a) Hovmöller diagram (cross-slope distance against time) of along-slope surface velocity for experiment W100P-16 (left of dashed line) and P-16P100 (right of dashed line). Green (negative) velocities flow to the west and red (positive) velocities flow to the east. Black scatter points indicate position of maximum/minimum ASC velocity. The dashed line thus indicates the change in surface forcing from a weak polynya to a strong polynya. Shading at the top indicates the shape of the ASF following the colour coding of Figure 3.1. Figure 3.8 shows the hydrographic conditions at the beginning of the yellow line. b) Time series of along-slope surface velocity at 300 km from the southern boundary.

Lastly, consider the asymmetric response of the two transient experiments to the applied changes in surface forcing (Figure 3.9b). The along-slope sur-

face velocity for experiment P-16P100 reaches after approximately 1.5 years (year 18) the start value of P100P-16, whereas P100P-1 takes approximately 10 years. The response of P-16P100 to the changes in surface forcing is much faster, because the onset of a strong buoyancy forcing in the polynya region affects the entire water column on the continental shelf via DSW production. After the first winter season, the bottom hydrography is influenced by the increase in salt flux. Changing the surface forcing from a strong to a weak polynya on the other hand (P100P-16) results in a much slower response. Instead of a fast propagation of the signal to deeper levels, the surface stratification increases and decouples the deep ocean from the surface forcing. The result implies that the transition is quicker (shorter distance in a Lagrangian framework) for a jet that enters an area of DSW compared to when it leaves such a region.

The observation-based map of the spatial distribution of the different ASF regimes (Figure 1.4) indicates that the result is consistent with the evolution of the double-sided ASF along the Weddell and Ross Seas and Prydz Bay. Essentially, to realise the double-sided frontal regime, a source of DSW on the continental shelf is required together with a stratified surface (weak convection). This situation is given downstream of the main DSW formation regions, where the continental shelf is – away from the source region – filled with DSW. Only when the influence of DSW in the water mass composition ceases, the frontal regime changes to be offshore single-sided. The change in the frontal structure occurs earlier in the real ocean compared to the process model, likely due to factors such as rough topography and unsteady surface forcing.

3.4 Discussion

3.4.1 Regime behaviour

The ASF has an almost circumpolar extent, but as observations suggest, varies in shape and strength along the coastline (Jacobs, 1991; Gill, 1973) and with it the associated leading order mechanisms responsible for cross-slope heat transport. Here, using an ocean process model, sensitivity experiments were performed to explore the sensitivity of the different ASF regimes to

atmospheric forcing. The non-dimensional ratio r, which compares the relative intensity of buoyancy forcing to mechanical forcing, is employed to define thresholds between different ASF regimes. No front forms when the input of APE on the continental shelf by surface buoyancy fluxes in a polynya is balanced by surface stress-driven coastal Ekman convergence. This situation occurs for a buoyancy to mechanical forcing ratio in the process model between $0.5 \leq r < 1$. If the ratio drops below $r = 0.5$, the coastal downwelling signal dominates and an offshore single-sided ASF forms. If the polynya activity is larger than the mechanical forcing ($r \geq 1$), the isopycnals shoal in an onshore direction and the onshore single-sided front develops.

The simulations suggest that the relative forcing thresholds governing the shape of the ASF are narrow. The regime shift from an offshore single-sided front to no front lies between $r = 0.45$ (W100P45) and $r = 0.5$ (W200P100), and from no front to the onshore single-sided front between $r = 0.9$ (W50P45) and $r = 1$ (W100P100). The exact values that set the thresholds depend on the definition of the control run (here W100P100) and are thus valid only within the present framework. Note, the configuration of some of the forcings is unrealistic in that the polynya activity is usually not completely decoupled from the surface stress. Other factors not included in the model and that impact the DSW production are freshwater supply from melting ice shelves upstream and the influence of varying sea ice extent. Adding these contributions, which influence the lateral and vertical stratification, would be an interesting extension for future work.

An important outcome is that each frontal regime can develop for multiple states as long as the ratio of buoyancy to mechanical forcing coincides. Conversely, this means that it is possible to change regimes by varying only one parameter, as has been shown with the five polynya sensitivity experiments that cover three ASF regimes. However, the sensitivity to changes in surface stress or buoyancy forcing varies with the intensity of the other. The two sets of experiments testing the sensitivity to mechanical forcing indicate, for example, that doubling the surface stress can, but must not result in a regime shift (Figure 3.4). This result is in agreement with sensitivity experiments performed by Hattermann (2018) which test the effect of wind stress and the cross-slope density gradient on the thermocline depth in an idealised

two-layer system of the Antarctic continental shelf break.

The sensitivity of the density distribution changes because the effect of the buoyancy and mechanical forcing varies with the background stratification. The stratification in the model is set by the northern boundary conditions which are the same for each simulation, and by the surface fluxes which vary by definition for each simulation. The buoyancy forcing has to work against stratification. A weaker stratification therefore favours an onshore shoaling of the isopycnals whereas a stronger stratification works in concord with the mechanical forcing and favours an onshore deepening of the isopycnals.

The above discussion on mechanical force versus buoyancy force argues that both are relevant in shaping the steady state of the ASF. The modelled variability of the ASC on a seasonal time scale, however, is dominated by the seasonal cycle in the surface stress field. The increase in wind in autumn and winter changes the sea surface height via Ekman dynamics (not shown) and the response is hence the same for all regimes that exhibit a westward slope jet. This conclusion agrees with other modelling work (Aoki et al., 2010; Mathiot et al., 2011) and observation-based studies (Núñez-Riboni and Fahrbach, 2009; Peña-Molino et al., 2016; Armitage et al., 2018; Hattermann, 2018), although they suggest together with the increase in along-slope velocity in winter a deepening of the pycnocline. Such a change in the subsurface density structure is missing in the present process model (not shown). A further limitation of the modelled seasonality is the lack of sea ice that has been shown to contribute to a seasonal cycle of the ASC (Núñez-Riboni and Fahrbach, 2009). The presence of sea ice alters the surface freshwater flux and the momentum transfer from the atmosphere to the ocean. The effect of sea ice can weaken or strengthen the surface momentum flux depending on the sea ice concentration, the drag coefficient, and the ice and ocean velocity, and thus poses a complex problem in formulating an accurate parameterisation for numerical models (Connolley et al., 2004; Lüpkes and Birnbaum, 2005; Lu et al., 2011; Cole et al., 2014; Manucharyan and Thompson, 2017). The applied idealised surface momentum flux field therefore simplifies the seasonal variability.

3.4.2 Dense continental shelves

The double-sided ASF is neither captured as a steady state nor as a seasonal feature in the process model. Instead, the simulations suggest for dense continental shelves the existence of an onshore single-sided slope front which has, however, never been described in the literature. The model results hence raise the question of how realistic the two regimes are.

Firstly, consider the option that the double-sided ASF is a seasonal (summertime) feature only that the process model is not able to replicate. An indicator for this is that all observational examples of the double-sided ASF have a summertime bias and that the double-sided ASF is characterised by a freshwater lens at the surface (Gill, 1973). The low density surface water displaces the isopycnals to both sides creating together with the acting mechanical force and DSW export the double-sided ASF. The surface freshwater is likely the result of melting sea ice in summer, a component that is not represented in the process model where the summertime buoyancy gain is homogeneously distributed in the entire domain. Note, using a parameterisation for the thermodynamics acting at the ocean/sea ice interface, Stewart and Thompson (2015, 2016) reproduce a steady state double-sided ASF in a process model. Their forcing is constant over time, but allows low salinity surface water to exist along and offshore the continental shelf break while DSW is produced in a polynya area at the southern boundary of the domain.

Secondly, consider the option that observations of the double-sided ASF are seeing a constant feature throughout the year, but a transient feature in space, which is suggested indirectly by the process model. This means that the double-sided ASF occurs as an intermediate shape between a fresh continental shelf (single-sided ASF) and a dense continental shelf (onshore single-sided ASF). The fact that the onshore single-sided ASF has not been observed in the Southern Ocean would imply that most dense Antarctic continental shelves are not long enough (in an along-slope direction) to allow the onshore single-sided ASF to fully develop. At this point, however, it is worth mentioning that the local deepening of the isopycnals is only a weak signal in the observations and leave room for interpretation. For example, hydrographic observations from the northwestern Weddell Sea could arguably also be interpreted as an onshore single-sided frontal shape (Thompson et al.,

2014; Azaneu et al., 2017), and with this support the here proposed hypothesis that the double-sided ASF is a transient feature.

3.5 Concluding remarks

This study illustrates how mechanical and buoyancy forcing (in a polynya region) control the shape of the isopycnals at the Antarctic continental slope that set the ASF. While the ratio of the two fluxes manifest the isopycnal slope, the sensitivity to changes in one forcing parameter varies with the background stratification set by the respective surface fluxes. The response time to varying atmospheric fluxes is shorter for mechanical forcing and it hence dominates the seasonal variability of the ASC. The ACoC on the other hand occurs only in summer for all simulations that show a pronounced seasonal cycle in surface salinity in the polynya region. The response time in the swap experiments to changes in the polynya activity is asymmetric. The onset of a strong polynya leads to a faster adjustment of the ASF shape than vice versa. With regard to the freshening trend of Antarctic continental shelf waters in the Ross and western Weddell Seas (Schmidtko et al., 2014), the result suggests a rather slow (if at all) deviation of the present-day dense-shelf regime to a fresh-shelf regime and towards stronger cross-slope density gradients in the decades to come.

The double-sided ASF is frequently discussed in the literature due to the fact that it has been observed. It is unique to the Antarctic shelf seas and is the most energetic regime. This study discusses whether this specific regime is a summertime feature only and/or whether it must be understood as a transient characteristic between the offshore single-sided and the onshore single-sided ASF. The sensitivity experiments performed here are not sufficient to form a conclusion on this point, but it remains to be emphasised that the double-sided ASF is very sensitive to the surface forcing and not necessarily a clear signal in observations. Additionally, this study argues for observational evidence of an onshore single-sided frontal regime in the northwestern Weddell Sea (Thompson et al., 2014; Azaneu et al., 2017).

Finally, note that the modelled ice shelf cavity is always characterised by shelf waters close to the surface freezing point resulting in low melt rates.

The result highlights that the shape of the ASF is not the only control on heat supply required for basal melting. The ice shelf front itself, where a large gradient in water column depth exists, poses a second dynamical barrier that lacks sufficient representation in the literature. Tides, as well as the continental shelf and cavity geometry, are other factors which are not considered in the present model configuration, but affect basal melting. Feedbacks between the processes will further impact the evolution of the ASF.

Chapter 4

Impact of basal freshwater on the dynamics of the Antarctic Slope Front

The final result chapter employs a state of the art circumpolar ice shelf/ocean/sea ice model and performs perturbation experiments to explore the sensitivity of the Antarctic continental shelf circulation to additional freshwater supply from under the ice shelves in a realistic domain. Motivated by the insights from the idealised model presented in the previous chapter, the focus lies on the shape of the ASF, the associated ASC, and on the identification of possible feedback mechanisms for basal melting.

Abstract

Basal meltwater of Antarctic ice shelves serves as a freshwater source to the shelf seas. This impacts the density field and in turn alters (among others) the ocean circulation. As the ocean warms, basal melt rates are expected to increase in the decades to come, and so is the freshwater input. Here, a coupled ocean/sea-ice/ice-shelf model with a circumpolar domain is used to explore the effect of increased basal freshwater supply on the dynamics of the ASF. It is the dynamics of the ASF that have a major control on heat transport across the Antarctic continental slope and hence on the basal melting of ice shelves. A present-day control run is compared to two perturbation experiments in which the ice shelf basal freshwater flux is artificially increased by a factor of two (2SSFLUX) or four (4SSFLUX). The trend between the experiments and the control run suggests a non-linear response of

the system to the perturbation. Detailed analysis of 4SSFLUX reveals that as a response to the additional basal freshwater input, the cross-slope density gradient becomes stronger everywhere along the Antarctic margin and the threshold for a regime shift of the ASF is met in East Antarctica, the Ross Sea and parts of the Amundsen Sea. The enhanced cross-slope density gradient also manifests in an increase of the along-slope transport of on average 22%. Two scenarios emerge regarding the cross-slope heat transport, as discussed in an exemplary way for the East Antarctic margin and the Amundsen Sea. In East Antarctica, cross-slope heat exchange reduces and continental shelf waters cool, which constitutes a mechanism that protects the ice shelves from further basal melting. In the Amundsen Sea on the other hand, faster coastal and slope jets advect relatively warm water from upstream resulting in warming continental shelf waters and a positive feedback mechanism with respect to basal melting.

4.1 Introduction

The Antarctic ice sheet and the Southern Ocean interact at the ocean-ice interface of numerous ice shelves, which are the floating extension of the grounded ice sheet. The ice shelves serve as a freshwater source into the oceans locally via basal melting and remotely via iceberg calving. The relative contribution to the freshwater input is on average approximately half each, but varies significantly around the coastline (Depoorter et al., 2013; Rignot et al., 2013). Basal melting predominates on continental shelves where relatively warm CDW has access to the ice shelf cavities and delivers the heat content required for the melting process (Pritchard et al., 2012). Observations suggest a positive trend in both near-bottom continental shelf temperatures and basal melt rates, leading to an increase in the ice discharge (Pritchard et al., 2012; Schmidtko et al., 2014; Paolo et al., 2015). The question arises as to how the additional freshwater input from basal melting in return impacts Southern Ocean dynamics, a topic currently not understood in detail (see review by Asay-Davis et al., 2017).

The freshwater input from basal melting occurs at depth, but can rise as a buoyant plume along the ice shelf base and can enhance stratification

of the water column Hellmer (2004). The increase in oceanic stratification may drive sea ice growth via a reduction in the vertical heat flux, and serves as a possible explanation for the positive trend in Antarctic sea ice extent (Hellmer, 2004; Bintanja et al., 2013, 2015; Merino et al., 2018). The strength of the relationship is under debate (Pauling et al., 2017) because not all models confirm a significant response in sea ice growth to the additional freshwater forcing (Swart and Fyfe, 2013; Pauling et al., 2016; Naughten et al., 2018b). Furthermore, in warm cavities, such as on the Amundsen Sea continental shelf, the available heat today already exceeds what is consumed in the basal melting process (Jourdain et al., 2017). Instead, warm water is entrained into the buoyant meltwater plume (Jenkins, 1999) and exported to the surface in front of the ice shelf where it can reduce sea ice formation. Increasing basal melt rates will enhance the cavity circulation and potentially accelerate sea ice melting.

The increase in ocean stratification on the continental shelf may not only affect sea ice growth, but also result in reduced full-depth convection and DSW production, the precursor of AABW (Hellmer, 2004; Fogwill et al., 2015; Phipps et al., 2016). The reduction in vertical mixing protects the relatively warm near-bottom waters from the overlying cold surface, leading to a warming signal at depth. A positive feedback loop forms when the warmer sub-surface water drives increased basal melt rates that further stratify the water column (Nakayama et al., 2014a; Fogwill et al., 2015; Bronselaer et al., 2018). Silvano et al. (2018) discuss this mechanism in a two-ice shelf system based on observations and a simple model. The cold, but buoyant meltwater from the upstream (eastward) ice shelf hinders deep convection at the ice shelf downstream (westward), even in the presence of a strong polynya, and thus isolates the warm water close to the ocean floor that can potentially drive substantial basal melting at the downstream ice shelf.

Most of the sensitivity studies mentioned above use climate system models that lack the horizontal resolution required to represent ice shelf cavities and the continental shelf circulation in a sufficient manner. As such, they are informative on large-scale Southern Ocean feedbacks on time scales relevant to ice sheets, but fail to capture smaller scales that dominate coastal ocean dynamics which in turn control ice shelf basal melting. Basal meltwater is

often parameterised as a uniform freshwater flux along the Antarctic margin (at the surface or at depth) without incorporation of regional variability. Using higher-resolution ocean models that take into account ocean-ice interaction at the base of the ice shelves, Nakayama et al. (2014a) and Kusahara and Hasumi (2014) demonstrate, however, that basal meltwater pathways greatly differ around the coastline and impact the strength of coastal currents. Similarly, Naughten et al. (2018b) trace back an acceleration of the coastal current in a future climate simulation, using a coupled ocean-ice-sea ice model, to a larger cross-slope density gradient due to freshening shelf waters.

The conclusion about the relationship between the cross-slope density gradient and current strength agrees with the sensitivity experiments performed in the process model of the Antarctic continental shelf break system in Chapter 3. Motivated by these results and given the manifold impacts basal freshwater may have, the role of basal freshwater on the Antarctic continental shelf ocean is further assessed in this chapter. A set of perturbation experiments with increased freshwater supply at the base of ice shelves is performed using a circumpolar state-of-the-art coupled ocean/sea-ice/ice-shelf model that allows for ocean-ice interaction in ice shelf cavities. The approach taken here isolates the increase in basal freshwater from a cause (such as a warming ocean or changes in the atmospheric surface fluxes) and reveals how basal freshwater as a single driver affects the Antarctic continental shelf seas. The focus of the analysis lies on the structure of the ASF and the associated ASC and aims to unfold differences in the response to the perturbation between regions.

4.2 Numerical model and perturbation experiments

4.2.1 Model description

This study uses the coupled ocean/sea-ice/ice-shelf model MetROMS-iceshelf, the details of which are described in Naughten et al. (2017) and Naughten et al. (2018a). The model consists of a modified version of the ROMS (Shchepetkin and McWilliams, 2005) with implemented ice-shelf thermody-

namics (Galton-Fenzi et al., 2012), and the sea-ice model CICE (Hunke et al., 2015). The coupling uses the Model Coupling Toolkit (MCT) (Larson et al., 2005; Jacob et al., 2005) and was conducted by the Norwegian Meteorological Institute (Debernard et al., 2017).

The circumpolar domain covers the Southern Ocean with a northern boundary at 30°S, but the analysis focuses on the Southern Ocean south of 60°S. The horizontal resolution is a 1/4° scaled by the cosine of the latitude and has a relocated South Pole to achieve a more equal resolution along the Antarctic margin. The mesh translates to resolutions of approximately 5 km at the southernmost ice shelf cavities, 8-10 km on the continental shelf, and 15-20 km in the ACC region (compare Figure 1a in Naughten et al. (2018a)). The vertical terrain following coordinate system has 31 layers and allows for an adequate representation of ice shelf cavities. The bathymetry and the static ice shelf draft derived from the RTopo-1.5 dataset (Timmermann et al., 2010) are smoothed to reduce pressure gradient errors which occur at steep slopes in terrain-following coordinate ocean models (Haney, 1991; Galton-Fenzi, 2009).

The model's control run is initialised with ocean temperature and salinity fields from the ECCO2 reanalysis product for January 1992 (Menemenlis et al., 2008; Wunsch et al., 2009) and the National Oceanic and Atmospheric Administration (NOAA)/National Snow and Ice Data Center (NSIDC) Climate Data Record for Passive Microwave Sea Ice Concentration (Meier et al., 2013). The model is integrated for a total of 20 years (1992-2011) driven by the ERA-Interim atmospheric reanalysis product (Dee et al., 2011) and an additional surface freshwater flux that accounts for iceberg melt (Martin and Adcroft, 2010). The ocean state after ten years of spin-up (1992-2001) is used to initialise two perturbation experiments that are integrated for an additional ten years. The first seven years (2002-2008) are the spin-up (Figure 4.1a, white background), and the final three years (2009-2011) are averaged and used to represent mean fields (Figure 4.1a, grey background). Note the spin-up is long enough to equilibrate ice shelf basal melt rates and the Antarctic continental shelf which is the region of interest (Naughten et al., 2018a).

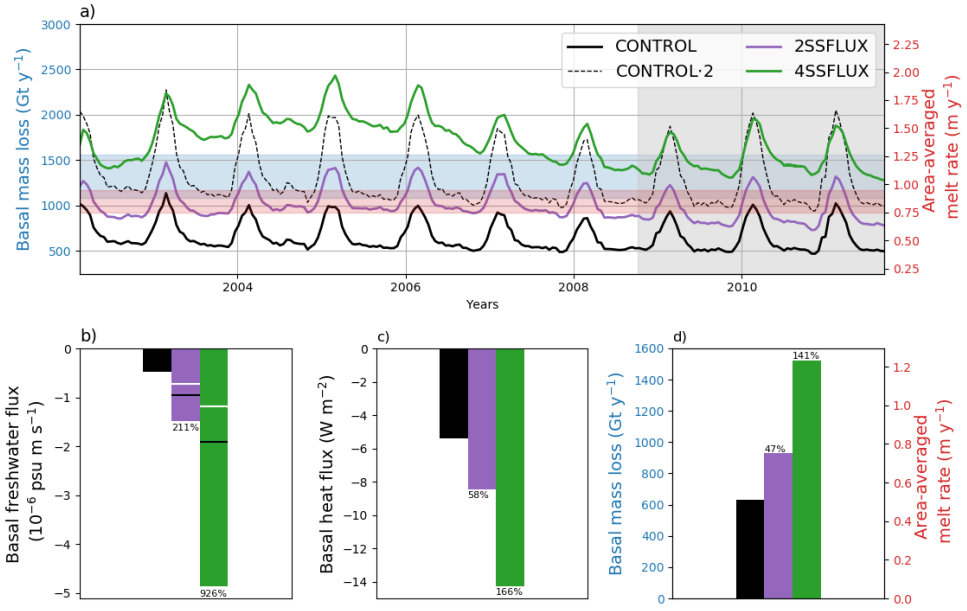

Figure 4.1: a) Time series of area-averaged basal mass loss (left ordinate) and ice shelf melt rate (right ordinate) for the control run (CONTROL) and the two perturbation experiments (2SSFLUX, 4SSFLUX). The dashed black line indicates the doubled melt rate of the control run and was added to help the reader to conceive where the melt rate of the perturbation experiments align relative to the control run. The shaded area indicates the observational values from Rignot et al. (2013). The grey shading marks the considered time period for the analysis of the simulations. b)-d) Time- and area-averaged surface freshwater flux (panel b, negative freshening), heat flux (panel c, negative cooling) and mass loss/melt rate (panel d) for all ice shelves and each simulation. The colour-coding is the same as in panel a). The numbers show the percentage increase of the perturbation experiments relative to the control run. The horizontal black lines in panel b) indicate the doubled and quadrupled freshwater flux value of the control run, and the horizontal white lines indicate 50% and 150% increase approximating the increase due to higher melt rates.

4.2.2 Experimental design

The reference run (CONTROL) is the same as presented in detail by Naughten et al. (2018a), where it was found to compare well with existing observations. The two perturbation experiments are designed to test the effect

of an artificially increased basal freshwater flux on the ocean system. In all three simulations, the melt rate is calculated at each time step using a three-equation formulation for the conservation of heat and salinity (Hellmer and Olbers, 1989; Holland and Jenkins, 1999). For the two perturbation experiments, the resulting salt flux is subsequently multiplied by a factor of two (2SSFLUX) or four (4SSFLUX). As the salt flux is negative in most of the domain due to the production of basal meltwater, this approach effectively results in a larger freshwater flux into the oceans. The resulting freshwater flux exceeds on average the expected value of either double and quadruple the freshwater flux of CONTROL (Figure 4.1b, black line). This is because the extra freshwater initiates internal feedback mechanisms that lead overall to higher melt rates (Figure 4.1d). One such mechanism is enhanced convection in the ice shelf cavity driven by the more buoyant surface layer, which may subsequently lead to a larger heat supply from the ambient ocean (Jenkins, 1999). Hence, the final freshwater flux is not double and quadruple the freshwater flux of CONTROL, but double and quadruple the freshwater flux of the higher basal melt rates (Figure 4.1b, white line).

The area-averaged melt rates of the three simulations reveal a non-linear response of the system to the applied perturbation. While the regional pattern of the response is similar (e.g. Figure B.1), the rate of change between 4SSFLUX and CONTROL is tripled compared to the change between 2SSFLUX and CONTROL, based on averaged values of melt rate (Figure 4.1d), along-slope transport, and sea ice area and extent. The remainder of the study concentrates on the comparison of the 4SSFLUX experiment with the control run. The CONTROL run produces melt rates that are lower than observations (Figure 4.1a), which Naughten et al. (2018a) explain by an insufficient grid resolution, but missing physical processes such as tides also play a role (Mueller et al., 2018). Additionally, Nakayama et al. (2014a) have shown for the Amundsen Sea that a bias in the atmospheric reanalysis product of ERA-Interim results in a colder continental shelf and in lower melt rates. While the 2SSFLUX experiment still lies below the observed melt rate, the 4SSFLUX experiment exceeds it and compares better with simulated melt rate projections for the end of the century (Naughten et al., 2018b).

4.3 General response to basal freshwater forcing

The following describes the general response to a perturbed ice shelf basal freshwater flux (i) on the continental shelf hydrography, (ii) on the ASF's structure and transport, and (iii) on sea ice to the additional freshwater supply. The focus of the analysis lies on the difference between 4SSFLUX and CONTROL, but where the consideration of the absolute values of CONTROL is beneficial for understanding the results, these are shown as well. The figures are introduced in the sections where they are most relevant, cross-referencing to later sections and figures is inevitable. The subsequent Section 4.4 aims to highlight links between different mechanisms at work at two individual example sectors, the East Antarctic margin and the Amundsen Sea, as they are representative for two different feedback loops that emerge as a response to the freshwater forcing.

4.3.1 Continental shelf hydrography

The additional freshwater introduced under the ice shelves in the perturbation experiment leads to changes in the hydrography on the Antarctic continental shelf. The salinity in 4SSFLUX (2SSFLUX) decreases on average by approximately 0.5 psu (0.2 psu) compared to CONTROL (Figure 4.2a). Observations from 1980 to the early 2010s suggest that the Antarctic shelf seas freshened in some areas by approximately 0.2 psu (Schmidtko et al., 2014). 4SSFLUX therefore exceeds observed values from the past, but may be a realistic scenario for future climates. Under the ice shelves, the freshening is confined to the surface layer which reflects the perturbation in the experiment. Nevertheless, the freshwater forcing is introduced to the open ocean environments at depth, which is why away from the cavities, the freshening signal can be found evenly distributed throughout the water column (Figure 4.3). This is an important result as the impact of ice shelf meltwater on the system critically depends on its vertical distribution.

Observations from the front of a fast melting ice shelf (Pine Island Glacier) show that buoyant meltwater is indeed exported laterally away from the ice shelf at depth (Garabato et al., 2017). The mechanism regulating the

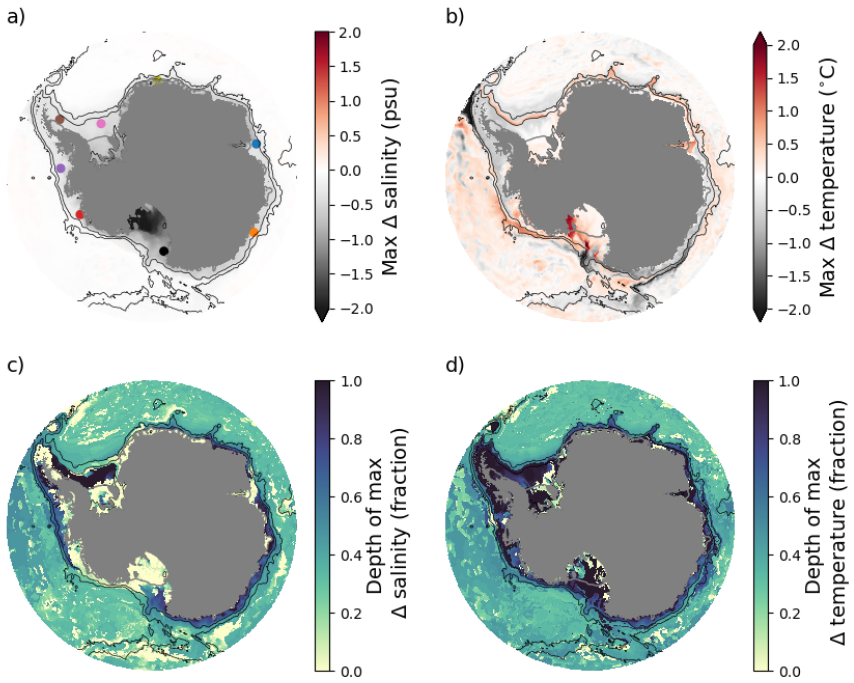

Figure 4.2: Magnitude of largest change and the fractional depth of that change where zero is at the surface/ice shelf base and 1 is at the sea floor for a), c) salinity and b), d) temperature. Black contours show the 1000 m and 3000 m isobaths, grey contours follow the ice shelf front. Coloured points in a) indicate the location of selected vertical profiles shown in Figure 4.3.

depth of the freshwater incorporates gravitational instability (due to unstable vertical stratification) and centrifugal instability (due to lateral shear). In the model, the process is not inevitably resolved and the mixing is expected to be sensitive to the chosen vertical mixing scheme (Timmermann and Beckmann, 2004). MetROMS employs the KPP boundary layer parameterisation (Large et al., 1994) with modifications as in Dinniman et al. (2011) to avoid extreme stratification during sea ice melt. While the KPP mixing scheme does not specifically parameterise the mixing processes near the ice shelf front, it aids to mix and export of the freshwater at depth in the model. Note, tides are not included in the model, but they drive additional mixing in the ice shelf cavity and on the continental shelf (Padman et al., 2018).

Only in the Amundsen Sea and near Prydz Bay is the freshening intensified in the upper water column leading to a stronger pycnocline (Figure 4.3d and 4.3g). The finding supports results from similar freshwater experiments performed for Amundsen Sea sector by Nakayama et al. (2014a) and Fogwill et al. (2015).

Temperature shows a more ambivalent response to the freshwater perturbation (Figure 4.2b). Most regions cool by approximately 0.5 °C in 4SSFLUX (0.2 °C in 2SSFLUX). However, the magnitude of the change is largest at depth (Figure 4.2d) with smaller expressions at the surface because surface waters are close to the surface freezing point in the CONTROL run (black vertical lines in Figure 4.3). The colder temperatures at depth indicate that the continental shelves are protected from intruding modified CDW from offshore (also compare Figure 4.8c). Conversely, the Amundsen Sea, Western Ross Sea, and Prydz Bay are warmer in 4SSFLUX (Figure 4.2b). The warming is confined to the subsurface and near the sea floor and shows a signature of modified CDW (warming and, compared to other profiles, little freshening) suggesting that in the perturbed simulation, these regions exhibit larger onshore heat and salt transport (see Section 4.4), where the latter compensates the larger freshwater input. As a response to the warmer shelf temperatures, basal melt rates and with this the freshwater flux are larger in these areas (Figure 4.6b and B.1).

4.3.2 ASF regime shifts

Following the definition of Chapter 3, the modelled ASF is classified into four different regimes: (i) no front exists when the isopycnals align with the horizontal, (ii) the offshore single-sided ASF has isopycnals that deepen in an onshore-direction, (iii) the double-sided ASF has additionally shoaling isopycnals to the south near the shelf break, and (iv) the onshore single-sided ASF has only the onshore part of the double-sided ASF. The inner band of Figure 4.4 shows the geographical classification for CONTROL and the outer band for 4SSFLUX. The band was constructed by using cross-slope density sections, a selection of which are shown in Figure 4.5, with a spacing of approximately 10° longitude. This allows a description of the frontal structure's approximate regional pattern, but withholds rather local varia-

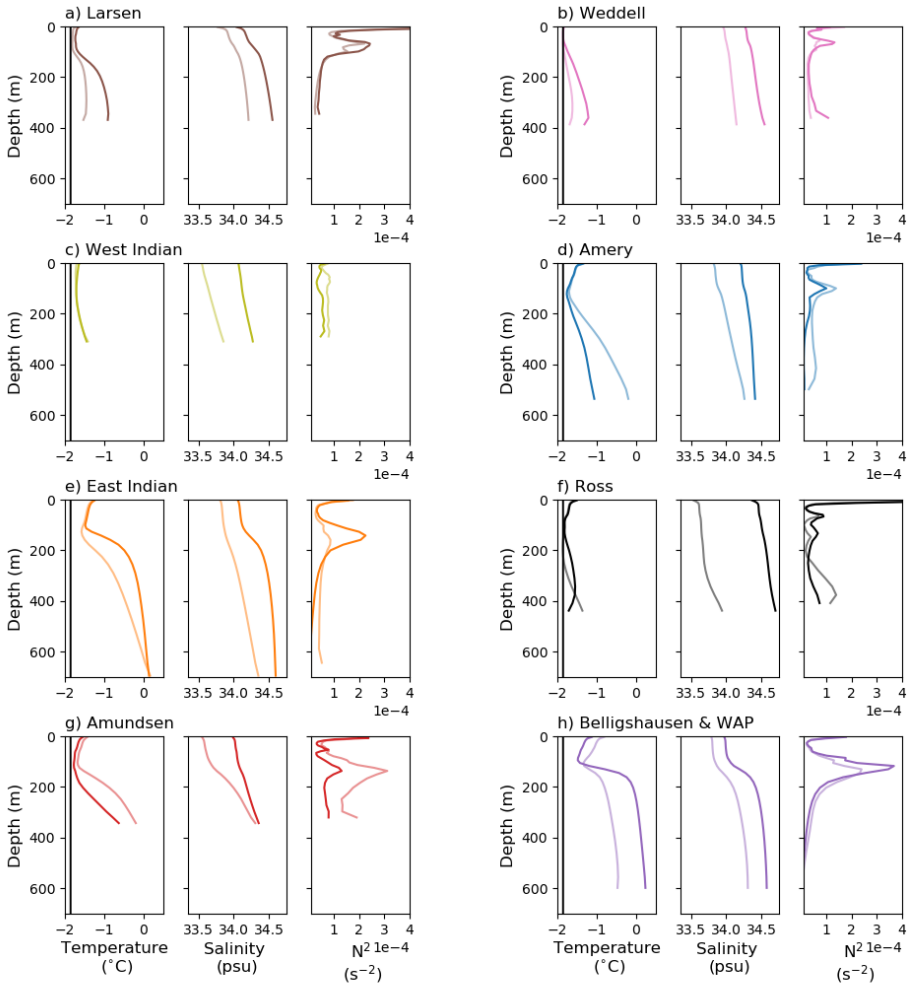

Figure 4.3: Vertical profiles of temperature (left), salinity (middle), and buoyancy frequency (right) for selected locations around the Antarctic coastline as indicated in Figure 4.2a. The darker profile refers to the CONTROL run and the transparent profile to the perturbation experiment 4SSFLUX. The black vertical lines in the temperature panels aid for orientation and indicate the respective surface freezing points.

tions that exist in reality, e.g., near submarine troughs or bounded regions of DSW export.

The CONTROL run captures all four regimes and can be compared to

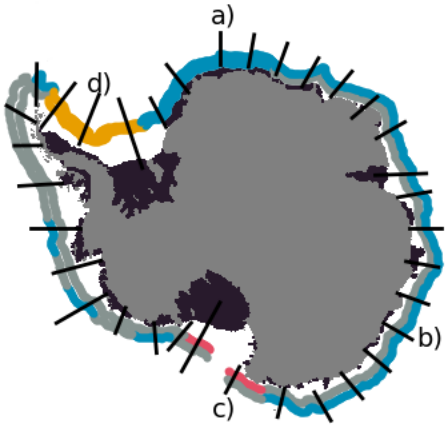

Figure 4.4: Classification of the ASF into different regimes based on the isopycnal shape at different cross-slope sections as indicated by the black lines. The inner band refers to the CONTROL run and the outer band to the perturbation experiment 4SSLFUX. Colours indicate the individual ASF regime of Figure 3.1: grey indicates no front, blue indicates the offshore single-sided ASF, red indicates the onshore single-sided ASF, and yellow indicates the double-sided ASF. Gaps represent areas that are not classified. The labels a), b), c) and d) correspond to the sections shown in Figure 4.5.

the observation-based classification from Thompson et al. (2018) shown in Figure 1.4. For most of the continental shelf slope of the CONTROL run, no front or a very weak front (also classified here as 'no front') exists. The result is in agreement with observations of the Bellingshausen and Amundsen Seas in West Antarctica. Observations in East Antarctica are sparse, but indicate the presence of a more diverse pattern in the frontal structure. Reasons for the discrepancy may be of numerical nature (e.g., horizontal grid resolution) and due to the fact that the data analysed here are temporal means that tend to smear out the frontal structure whereas observations reveal an explicit snapshot in time and are often biased to summertime. The offshore single-sided ASF occurs in the CONTROL run only in the Atlantic sector around the Prime Meridian. The double-sided ASF develops in the western Weddell Sea where the export of DSW lifts the isopycnals in an onshore direction. Other known regions of DSW export and a double-sided ASF are the Ross Sea and downstream of Prydz Bay near the Amery Ice Shelf. In the Ross Sea sector, the present study classified the frontal structure to be onshore single-

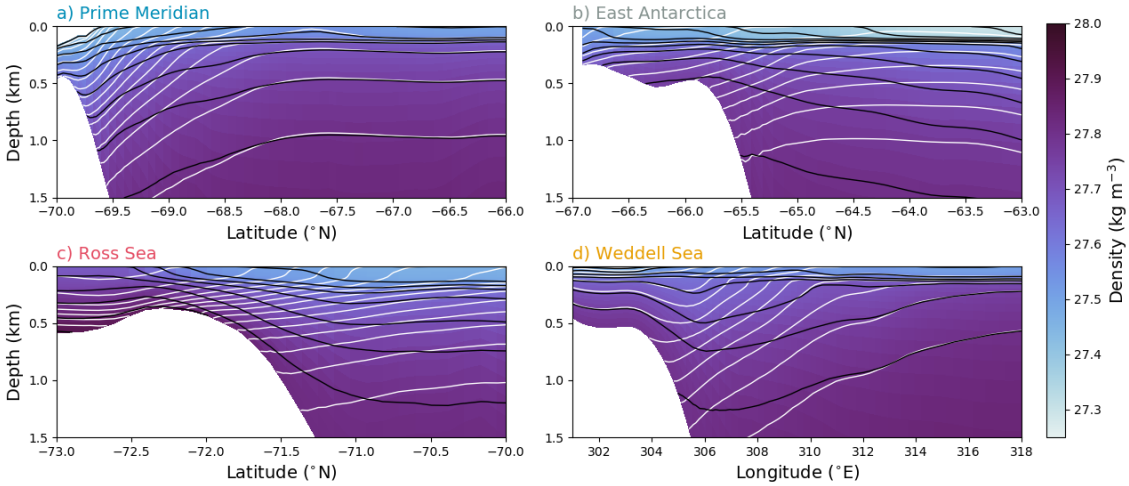

Figure 4.5: Cross-slope sections as labelled in Figure 4.4 of potential density (referenced to the surface). Shading and black contours are the CONTROL run and white contours show the density distribution of the perturbation experiment 4SSFLUX. The contour intervals are 0.05 kg m^{-3}. Each panel represents a different frontal structure of the ASF in the CONTROL run as defined in Chapter 3: a) has a offshore single-sided ASF, b) has no front, c) has an onshore single-sided ASF, and d) has a double-sided ASF. Colour-coding of the titles as in Chapter 3 and Figure 4.4.

sided, a category that does not exist in Thompson et al. (2018)'s review paper. As argued in Chapter 3, this regime appears for dense continental shelves when the onshore shoaling of the isopycnals due to the presence of DSW dominates. Near Prydz Bay, the frontal structure has a weak expression in the CONTROL run which can be explained by the fact that the model does not produce AABW in this region (Naughten et al., 2018a).

The shape of the ASF changes in 4SSFLUX and a regime shift occurs along most of the Antarctic coastline (Figure 4.4, outer band). The lower salinity on the continental shelf (Section 4.3.1) leads to a stronger cross-slope density gradient which manifests by downsloping isopycnals in an onshore direction (Figure 4.5, white contours). Even in regions where no regime shift occurs, such as in the Weddell Sea, the Bellingshausen Sea and parts of the Amundsen Sea, the cross-slope density gradient is stronger in 4SSFLUX. The entire East Antarctic sector is characterised by an offshore single-sided ASF, while it has no front in CONTROL. In the Ross Sea, the prevailing onshore

shoaling of the isopycnals in CONTROL is less apparent in 4SSLFUX so that no prominent frontal feature exists at the shelf break. The Amundsen Sea develops a distinct offshore single-sided ASF in 4SSFLUX in some of the analysed sections. The Bellingshausen Sea is in the no front regime for both CONTROL and 4SSFLUX. At the tip of the Antarctic Peninsula, which is in the no front regime in CONTROL, the single-sided ASF occurs in 4SSFLUX, whereas the western Weddell Sea has a double-sided ASF in both simulations, but with a more pronounced offshore half in 4SSFLUX (Figure 4.5d).

4.3.3 Increase in ASC transport

The previous paragraphs established that the additional freshwater of the perturbation experiment results overall in a colder, but also fresher and ultimately a less dense Antarctic continental shelf. The larger cross-shelf density gradient subsequently strengthens the ASF which has downsloping isopycnals in an onshore direction along most of the Antarctic coastline. The findings from the idealised domain of Chapter 3 suggest that the change in the frontal structure goes along with an accelerated ASC. Figure 4.6 demonstrates that the result holds in the realistic domain. The along-slope transport is calculated for a band of ten grid cells centred around the 1000 m isobath. The 1000 m isobath coincides approximately with the position of maximum ASC speed (not shown) and has a circumpolar extent. The velocity vectors at each grid cell are rotated to a local along-slope/cross-slope coordinate system in order to obtain the true along-slope velocity component.

The along-slope transport in the CONTROL run is – despite a few very localised points in the Ross and Weddell Seas – oriented such that the shallow Antarctic continental shelf is to the left of the flow, which usually means in a westward direction (negative values in Figure 4.6a). The transport is on average -8.57 Sv, but varies around the Antarctic coastline with maximum values of approximately -20 Sv. The variability is larger on small scales, but overall, large along-slope transports occur in East Antarctica at around 140° - 170°E and at the tip of the Antarctic Peninsula. Lowest along-slope transport occurs near the Prime Meridian and in West Antarctica at parts of the Ross Sea, and in the Amundsen and Bellingshausen Seas.

Estimates of ASC transport in the literature can vary significantly. Rea-

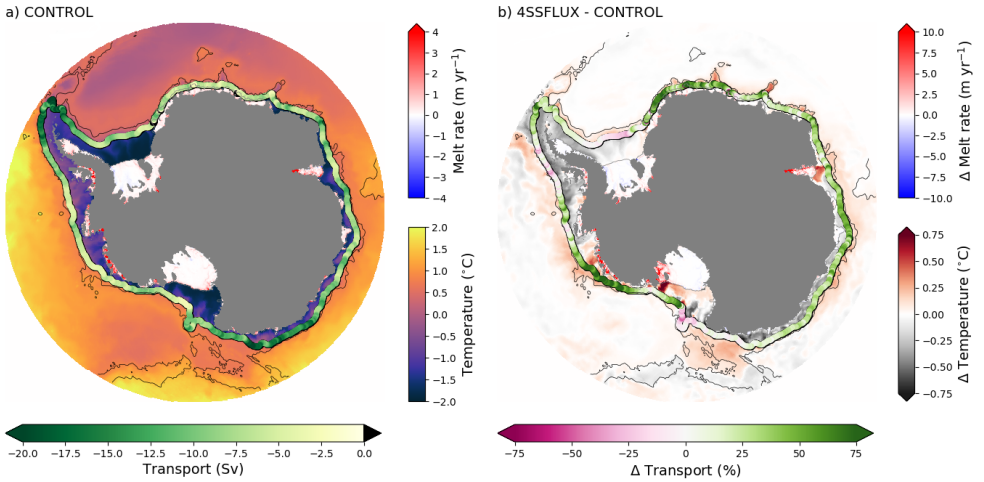

Figure 4.6: a) Depth-averaged temperature, ice shelf basal melt rate (positive is melting, negative is refreezing) as well as along-slope transport at the 1000 m isobath for the CONTROL run (negative is in counter-clockwise direction). The black contour indicates the 3000 m isobath. b) Same as in a), but showing the difference between the perturbation experiment 4SSFLUX and the CONTROL run. Positive values indicate higher temperatures, higher melt rates and larger along-slope transport in a counter-clockwise direction.

sons for the wide spread are (i) different approaches to define and calculate the ASC transport, (ii) the varying grid resolution in the case of numerical models, and (iii) the high spatial and temporal variability of the ASC. Especially the latter makes it difficult to compare the sparse observational estimates with model output or observations from up-/downstream or with data obtained at a different time in the year. The ASC transport in this model seems to overall underestimate the full transport, possibly due to the lack of tides (Flexas et al., 2015; Stewart et al., 2018) and horizontal grid resolution, but the large-variation along the coastline agrees qualitatively with what is presented in the literature (Heywood et al., 1998; Aoki et al., 2010; Meijers et al., 2010; Mathiot et al., 2011; Peña-Molino et al., 2016). An exception is the western Antarctic Peninsula, where the proximity of the ACC should result in an eastward rather than westward transport.

In 4SSFLUX, the mean ASC transport increases by 22% (in 2SSFLUX

by 8%), which satisfies the hypothesis developed in Chapter 3. Hence, the perturbation experiment is not only a better representation for the observed melt rates (Figure 4.1), but also for the along-slope transport. The transport is larger everywhere along the continental slope, despite confined areas in the Ross and Weddell Seas as well as along the Western Antarctic Peninsula where the along-slope transport does not change or is weaker (Figure 4.6b). In the Ross Sea, the decrease occurs along the northward extension of the continental shelf at the Iselin Bank. The increase in along-slope transport by approximately 70% is most pronounced in the Amundsen Sea and in the Western Indian Ocean. Especially in the Bellingshausen and Amundsen Seas, the ASC intensifies predominantly in the west in response to the increased freshwater flux. This is likely related to the channelling of the outflow along the western side of the major bathymetric troughs in each region (see also Figure 4.10).

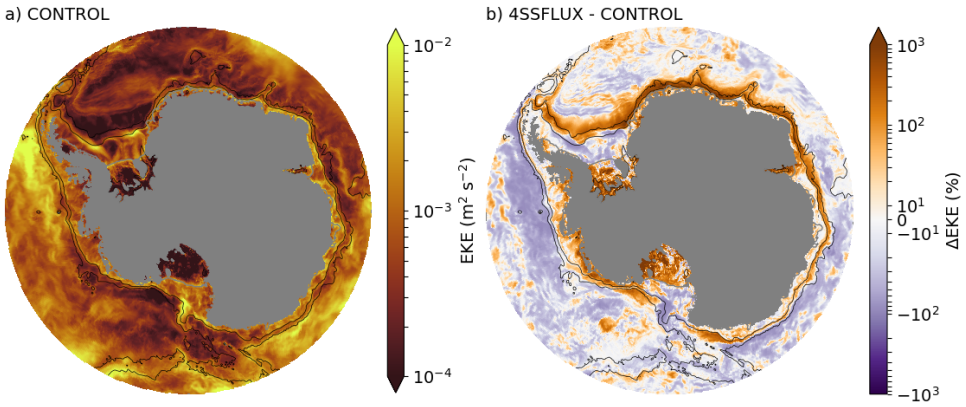

Figure 4.7: a) Depth-averaged eddy kinetic energy for the CONTROL run on a logarithmic colour scale and b) changes in eddy kinetic energy in percent between the perturbation experiment 4SSFLUX and the CONTROL run. A change of 1000% corresponds to a change of one order of magnitude. Black contours show the 1000 m and 3000 m isobaths, grey contours follow the ice shelf front.

The position of the ASC reveals itself also as a local maximum in the EKE field (Figure 4.7a). The magnitude of the EKE maxima in CONTROL is between 0.01 m^2 s^{-2} and 0.001 m^2 s^{-2} which agrees reasonably well with

estimates from a high resolution (1/48°) global model presented by Stewart et al. (2018) for the East Antarctic sector. Nevertheless, the grid resolution of the present model configuration at the continental shelf of 8-10 km is not high enough to resolve the Rossby deformation radius which approximates the horizontal scale required to capture baroclinic instabilities and is only a few kilometres on the continental slope. The modelled EKE field is thus expected to emerge from mostly barotropic instabilities and to underestimate the full EKE field. Especially in East Antarctica, where the frontal structure is too weak in the model, there is the potential that the modelled EKE does not reflect present conditions.

The EKE on the continental shelf break is higher in 4SSFLUX. Areas of higher EKE appear to have a larger baroclinic velocity component (Figure B.2) which suggests that baroclinic instabilities may, at least in part, be the cause for the increased EKE production. The baroclinic instabilities then act to flatten the isopycnals and reduce the transport driven by thermal wind. For example, the increase in EKE is largest in East Antarctica (order of magnitude). Here, the relative baroclinic along-slope velocity component changes from approximately 5% in CONTROL to 25% in 4SSFLUX.

4.3.4 Changes in sea ice

The sea ice in 4SSFLUX (2SSFLUX) increases by 2.5% (1%) in area and 4.5% (3.7%) in volume with large regional differences (Figure 4.8a and 4.8b). These changes have a similar pattern throughout the year which is why an annual average is sufficient for this analysis, even though the sea ice itself has a strong seasonal cycle (Figure B.3). The modelled changes in sea ice area and sea ice thickness match in that thinning sea ice corresponds to lower sea ice concentration and vice versa. The differences are largest on the continental shelf (a weak surface salinity restoring in the open ocean might dampen sea ice changes in these areas) and generally mirror the anomalies of the surface temperature field which are induced by the freshwater anomalies under the ice shelves (Figure 4.8c). As such, the Bellingshausen and Amundsen Sea sector, the eastern Weddell Sea, as well as the Indian sector show a decrease in sea ice near the continental shelf. The Ross Sea, parts of the western Pacific sector and the West Antarctic Peninsula show an increase in sea ice.

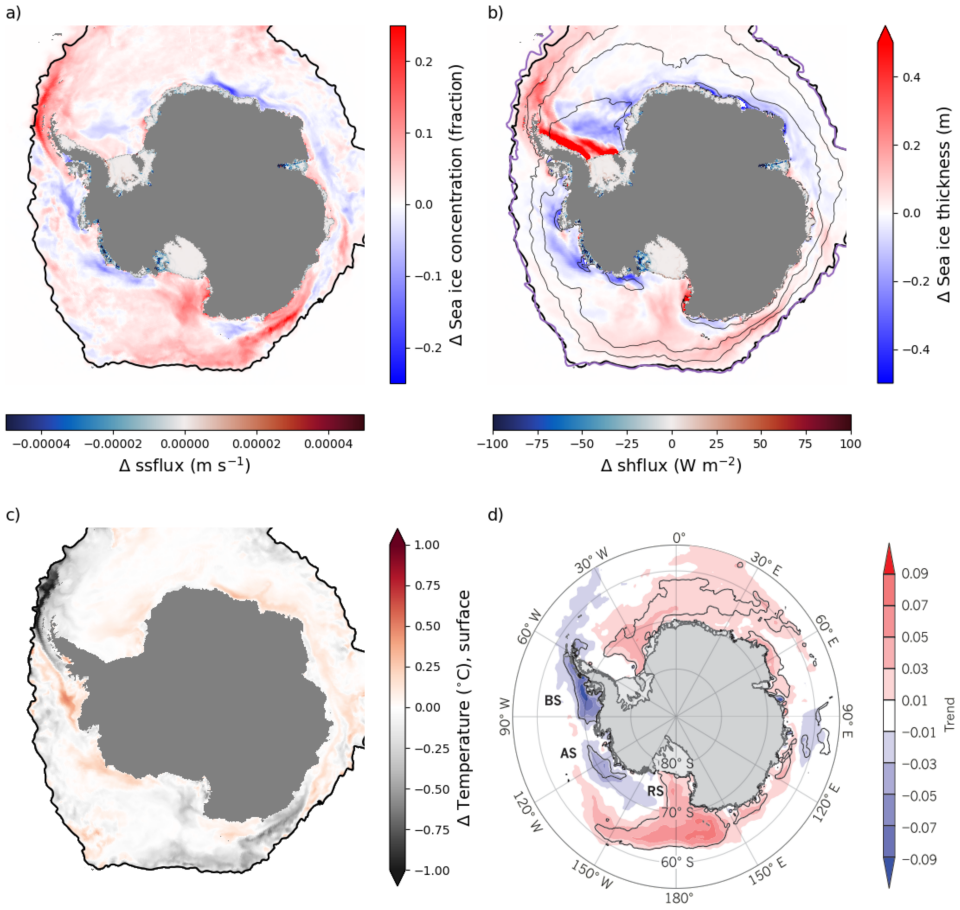

Figure 4.8: Changes between the perturbation experiment 4SSFLUX and the CONTROL run for a) sea ice concentration, b) sea ice thickness, and c) surface temperature. The thick black contour shows the sea ice extent of the CONTROL run. Panel b) additionally shows the sea ice thickness of the CONTROL run in 0.25 m contours (thin black) as well as the sea ice extend of the perturbation experiment 4SSFLUX (purple). d) Figure 1 of King (2014) showing the observed trend (fractional ice coverage per decade) in sea ice concentration from 1979-2012. Areas enclosed by the black contours have a trend that is statistical significant on the 5% level.

A comparison of the modelled differences in sea ice concentration with the observed trend over the period from 1979-2012 (Figure 4.8b and 4.8d) reveals that the trend in the Amundsen and Ross Seas can, at least in part, be

attributed to hydrographic changes due to larger freshwater supply from basal melting. With this, changes in the freshwater supply together with changes in the surface wind stress, which have previously been suggested as the driver for sea ice tends in this sector (Zhang, 2007), serve as an explanation for the observed sea ice trend. As melt rates and with it the freshwater flux are expected to increase, it is likely that the pattern in the sea ice trend will be the same in the future. Freshwater perturbation experiments performed by Merino et al. (2018) in a circumpolar configuration of NEMOv3.5 (without ice shelves, freshwater forcing is implemented at the surface to represent ice berg calving and at depth to represent ice shelf basal melting) confirm the pattern of freshwater induced sea ice changes in this sector.

Agreement in the modelled pattern of sea ice change between Merino et al. (2018) and the present perturbation experiment also exists in other regions around the coastline. However, in the Bellingshausen and Weddell Seas as well as in East Antarctica between the Weddell Sea and Prydz Bay, the modelled freshwater induced changes do not match the observed trends. This suggests that freshwater forcing counteracts other drivers, such as the surface wind stress, and that a larger freshwater input in the future may either dampen or intensify sea ice loss, making it harder to make projections of the evolution of sea ice in these regions.

An anomaly in the western Weddell Sea shows pronounced thickening of more than 1 m without changes in sea ice concentrations, which does not go along with cooler surface temperatures that may favour sea ice growth. The result is, however, consistent with Kusahara and Hasumi (2014) who find thicker sea ice in the western Weddell Sea and Weddell Gyre for a simulation that takes thermodynamics under the Filchner-Ronne Ice Shelf into account compared to a simulation without basal melting. They also find thicker sea ice in the Amundsen and Bellingshausen Seas and downstream of Prydz Bay, and correlate these locations with pathways of basal meltwater that escapes the ice shelf cavities in the thermodynamic runs.

The findings highlight the consistency but also differences between the models and different areas, underpinning that sea ice is very sensitive as to how the freshwater perturbation is applied and to the vertical mixing parameterisation. These two factors in particular determine the vertical strat-

ification and vertical heat transport that is so crucial for sea ice growth. For example, the basal meltwater always stratifies the ocean surface and leads to positive sea ice anomalies in Kusahara and Hasumi (2014) in the Bellingshausen and Amundsen Seas and downstream of Prydz Bay, unlike for MetROMS which shows a reduction in sea ice in these areas. More work needs to be done to achieve greater consensus between the circumpolar models and to eventually improve future climate simulations by low resolution global climate models.

4.4 Insight into individual regions

To discuss the response to the applied freshwater forcing two different sectors are defined: the East Antarctic margin near the Totten Ice Shelf (Figure 4.9f) and the Amundsen Sea (Figure 4.10f). These sectors are chosen because they show in an exemplary way different feedback loops, a negative and a positive feedback, that come into play and that are illustrated in Figure 4.11. Note that in other regions differing local factors may alter the mechanisms at work.

On the East Antarctic margin, a negative feedback dominates the response to the freshwater forcing (Figure 4.11, black arrows). The basal freshwater results in a lower continental shelf salinity (Figure 4.2a and 4.3e) and the larger cross-slope density gradient steepens the isopycnals of the ASF (Figure 4.5b) and the ASC speeds up (Figure 4.6b and 4.9b). At the lower continental slope, the isotherms move upwards and intersect with the bathymetry at shallower depth which results in warmer temperatures at depth (Figure 4.9c, 4.9d and 4.9e). Note that the warming at depth of the lower continental shelf is a circumpolar feature (Figure 4.6b). At the upper continental shelf, the isotherms move offshore and the continental shelf waters cool as they are isolated from the warmer offshore waters. The negative feedback loop closes as the colder shelf temperatures offset an increase in basal melting which is driven by a larger cavity circulation. The basal melt rates in this region are consequently almost the same in CONTROL and 4SSFLUX (Figure 4.9a).

With this, a feedback mechanism is presented that can dampen the projected warming of the Antarctic shelf region and ice shelf cavities (Goddard

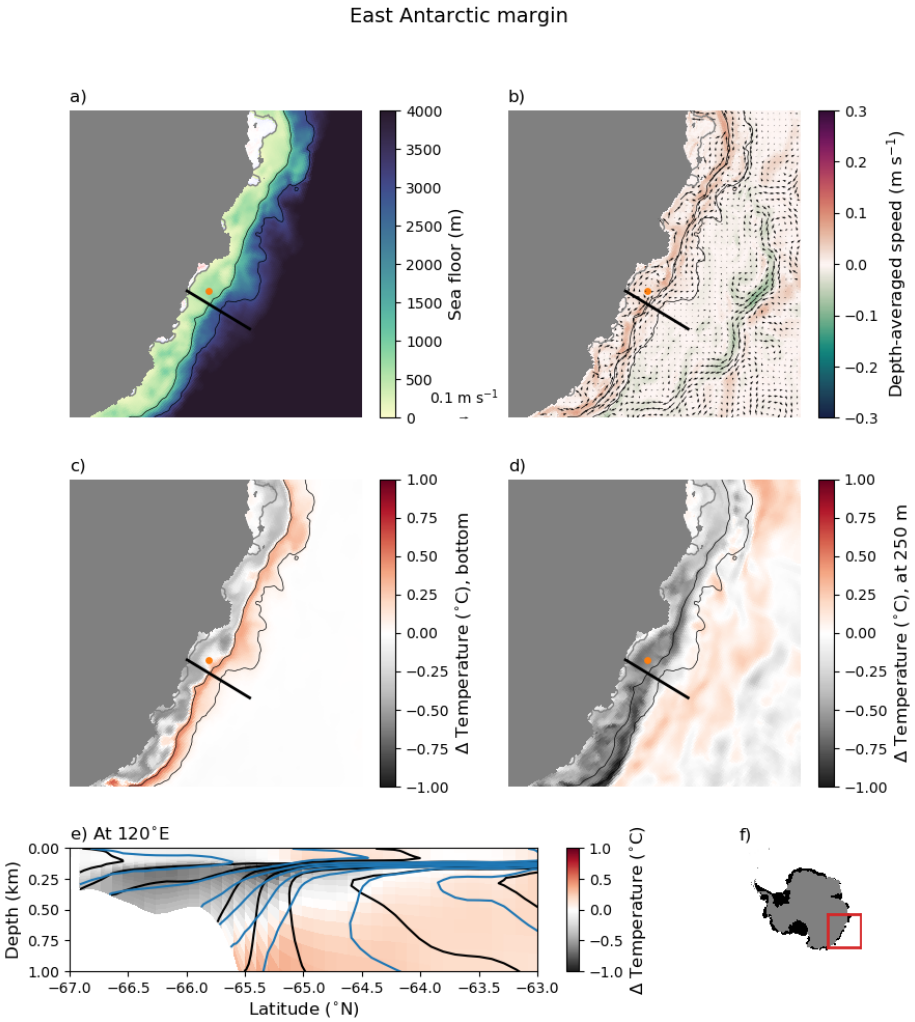

Figure 4.9: a) Bathymetry of the Amundsen Sea sector together with the change in melt rate between the perturbation experiment 4SSFLUX and the CONTROL run (as in Figure 4.6b). b) Change in depth-averaged velocity, c) change in bottom temperature, and d) change in temperature at 250 m depth. The arrows in panel b) show the direction of the currents of the CONTROL run. Grey contour indicates the ice shelf front, black contours the 1 km and 3 km isobath. The orange marker indicates the location of the vertical section shown in Figure 4.3. e) Differences in temperature on a cross-section as indicated by the black line in panels a)-d). The black contours correspond to the CONTROL run and the blue contours to the perturbation experiment 4SSFLUX. The contour spacing is 0.5°C. f) Map indicating the zoomed area shown in panels a)-d).

et al., 2017; Naughten et al., 2018b) and that acts to protect the ice shelf cavities from enhanced heat supply. The mechanism is also active in the western Antarctic Peninsula and in the Weddell Sea. Whether this process is more important than, e.g., wind-driven changes in the velocity field which have been suggested to favour onshore heat transport in a future climate (Hellmer et al., 2012), remains to be explored.

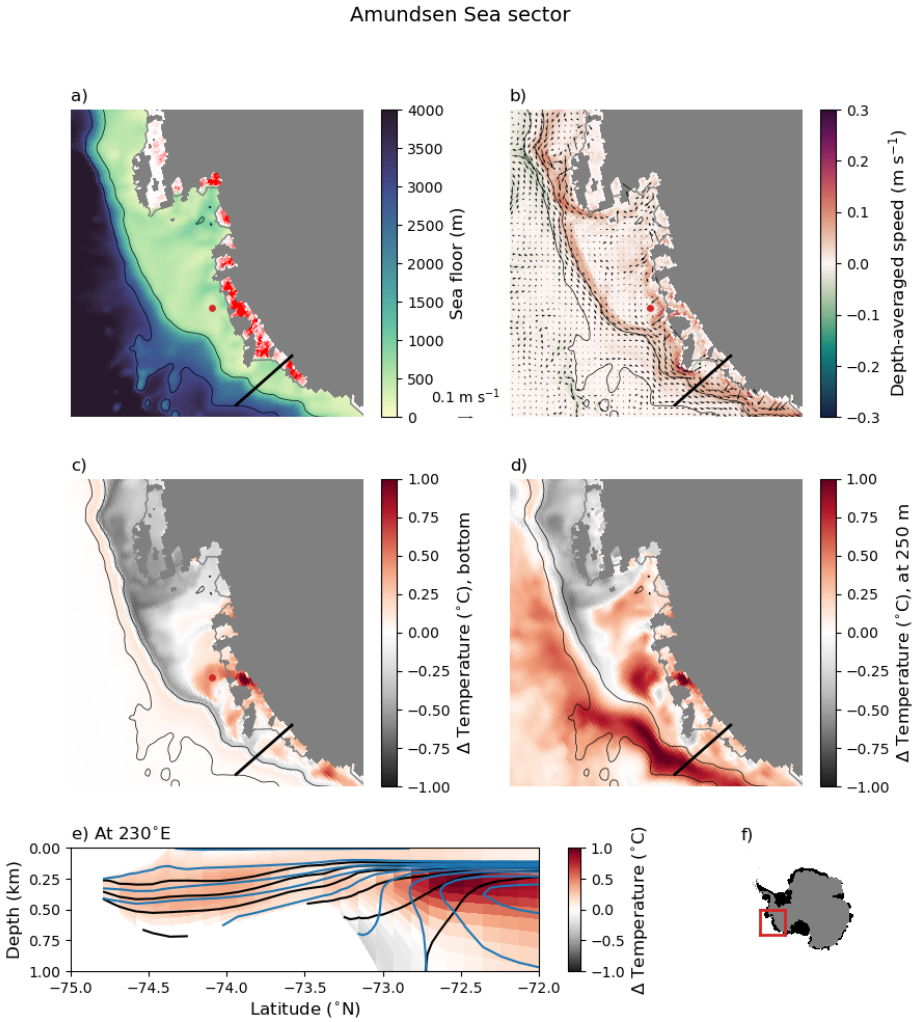

Figure 4.10: As in Figure 4.9, but for the Amundsen Sea sector.

In the Amundsen Sea sector, similar to the East Antarctic margin, the cross-slope density gradient and along-slope velocities increase as a response to the freshwater forcing (Figure 4.4, 4.6b and 4.10b). While the eastern Amundsen and Bellingshausen Seas cool, a positive feedback loop (Figure 4.11,

red arrows) emerges west of Pine Island Glacier, where continental shelf waters warm (Figure 4.10c, 4.10d, 4.10e). Here, melting drives a stronger continental shelf circulation and with this increases the cross-slope advection of CDW. The continental shelf warming is thus most pronounced in the subsurface near the Thwaites and Dotson Ice Shelves where the westward ASC intensifies most (Figure 4.10b and 4.10d). Figure 4.10e shows how, at the continental shelf break, the isotherms in the subsurface at approximately 250 m depth move onshore. To reiterate the finding from Section 4.3.1 (Figure 4.3g), the warming reflects the increased onshore CDW transport as opposed to a warming of the CDW itself. Additionally, the melting drives a stronger cavity circulation and replenishment of the cavity water, which results in warmer temperatures near the ice shelf fronts of the Crosson, Dotson and Getz Ice Shelves. The stronger ACoC in 4SSFLUX transports the warmer waters (compared to CONTROL) downstream. The warmer temperatures together with a larger cavity circulation (caused by the perturbation) increase the basal melt rates (Figure 4.10a), which in turn further increase the freshwater flux.

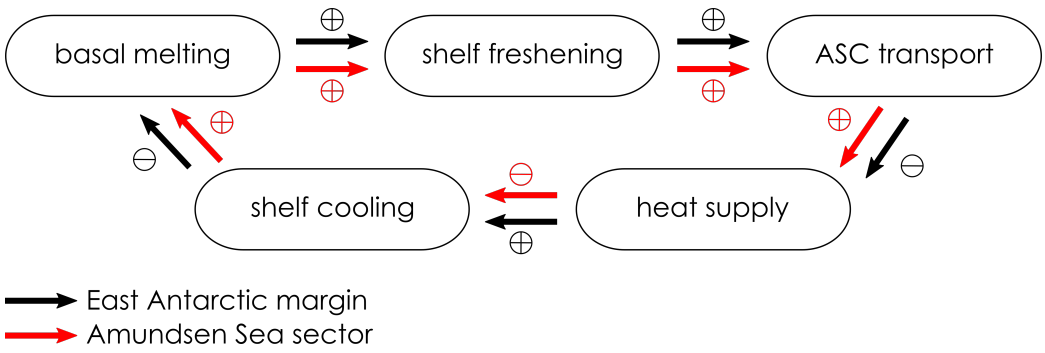

Figure 4.11: Schematic showing a negative feedback (black arrows) and a positive feedback (red arrows) as a response to increased basal melting.

A strong caveat of the model is its inability to simulate the observed (Walker et al., 2013) and modelled (Nakayama et al., 2014b) eastward-flowing undercurrent in the Amundsen Sea. This poses a problem, because the interaction of the undercurrent with the topography near the submarine troughs allows CDW to travel to the south and to steadily supply the continental shelf

with relatively warm water (Walker et al., 2013). The model thus shows a cold bias that can be linked to a lack of horizontal grid resolution (Nakayama et al., 2014b). While the model does not capture the full ocean dynamics, other aspects of the occurring dynamical changes in the model agree with previous studies. For example, a relation between the depth of the isotherm at the continental shelf break and basal melt rates has been established before (reviewed by Jenkins et al., 2016). Similarly, Nakayama et al. (2014a) support the finding that basal meltwater strengthens the ACoC and transports relatively warm shelf waters downstream which is then available for the basal melting process. The positive feedback mechanism serves as one explanation for the positive trend in basal melting in this region (Pritchard et al., 2012). However, long-term time series of the ocean temperature in the Amundsen Sea indicate a decadal variability which does not correlate with changes in basal melting (Figure 5 in Jenkins et al., 2016). More work needs to be done to understand the interaction of ocean temperature and basal melting on longer time scales, a problem which cannot be addressed with the present experimental setup.

The positive feedback discussed here differs from the positive feedback explored by Silvano et al. (2018), where meltwater from an upstream ice shelf reduces the activity of a polynya downstream which in turn prevents full-depth convection and ultimately results in warmer continental shelf waters at depth that drive ice shelf basal melting. The positive feedback loop discussed here is importance because the Amundsen Sea is susceptible to marine ice sheet instability with consequences for the global sea level (Bamber et al., 2009).

4.5 Concluding remarks

The Antarctic continental shelf sea response to a perturbed basal freshwater flux has been investigated using a coupled ocean/sea-ice/ice-shelf model with a circumpolar domain. The experiments comprise an unperturbed CONTROL run of the time period from 1992-2011 (the analysis focuses on the time-averaged last three years of model integration) and two perturbation experiments. The perturbation experiments have a doubled (2SSFLUX)

and a quadrupled (4SSFLUX) ice shelf basal freshwater flux. The two experiments exhibit a similar regional pattern, but they suggest a non-linear response of the system to the applied perturbation. The analysis primarily focused on the comparison between the stronger 4SSFLUX experiment and the CONTROL run. The perturbation is performed in the model code introduces an inconsistency in the melt rate parameterisation, however, the approach serves the purpose of this study as it allows to isolate the effect that increased ice shelf basal melting has on the Antarctic continental shelf sea. Additionally, the injection of the freshwater flux occurs at depth (as supposed to at the surface) and accounts for the spatial distribution of Antarctic ice shelves and with this of the freshwater discharge.

The effect of the increased basal freshwater flux is apparent on the Antarctic continental shelf and slope in all regions. Interestingly, the continental shelf waters freshen throughout the water column, as opposed to a confined surface signal which would stratify the water column. Consequently, full-depth convection is on average not reduced and neither is the associated vertical mixing of heat. Hence, the hypothesis of cooling surface waters and warming subsurface waters on the continental shelf as introduced in the Introduction 4.1 does not hold, and sea ice area (2.5% in 4SSFLUX and 1% in 2SSFLUX) and sea ice volume (4.5% in 4SSFLUX and 3.7% in 2SSFLUX) merely increase. The lower continental shelf salinity and with this density does, however, result in a larger cross-slope density gradient, which changes the frontal structure of the ASF and results in a larger along-slope transport of 22% (8%) in 4SSFLUX (2SSFLUX) compared to CONTROL. Two scenarios emerge from the increased freshwater (Figure 4.11):

- The strengthening of the ASF further protects the continental shelf sea from the warmer CDW that resides offshore. This results in a negative feedback as the colder continental shelf waters lead to reduced basal melting. The mechanism may counteract the, here neglected, continental shelf warming due to changes in the atmosphere and hence is a significant finding of the perturbation experiment.

- The stronger coastal currents advect heat from warm waters upstream and guide the heat onto the continental shelf and into the ice shelf

cavities. This drives more basal melting which again accelerates along-slope velocities and a positive feedback loop develops. This mechanism is at work in the Amundsen Sea/western Ross Sea sector and potentially also in Prydz Bay. Increasing basal melt rates in these areas therefore do not protect the ice shelves from further heat supply.

To conclude, the presented simulations have revealed insight as to how ice shelf basal freshwater affects the ocean dynamics on the Antarctic continental shelf, emphasising the role of ocean-ice interaction on shelf break system. The proper representation Antarctic ice shelf meltwater is therefore crucial for future climate simulations.

Chapter 5

Conclusion

The processes relevant to the Antarctic continental shelf break system, which consists of ice shelf cavities, the continental shelf, and the continental shelf break, are crucial for the stability of the Antarctic ice sheet and ultimately global sea level. Yet many processes are lacking a sufficient understanding, resulting in large uncertainties in the projection of the future evolution of the Antarctic ice sheet. This is in part due to the region's inaccessibility, but also the interaction of processes that have different temporal and spatial scales. This thesis contributes to this overall problem by investigating the dynamics of the ASF, which have been identified to have a major control on the heat supply required for basal melting of the Antarctic ice shelves. Two different numerical model configurations were used: the idealised channel domain, which allowed for the exploration of processes relevant to the stability of the ASF, and the circumpolar domain, which allowed to take into account regional variations.

The key conclusions of the thesis, which achieved the objectives set out in Chapter 1.4, are:

- A new idealised configuration of the Antarctic continental shelf break system has been developed. The major cornerstones are: the incorporation of thermodynamics at the base of static ice shelves; a grid resolution that resolves mesoscale ocean processes; terrain-following vertical coordinates; periodic boundary conditions which simulate the circumpolar character of the Antarctic continental shelf break; and a zonally symmetric bathymetry. The configuration complements existing model configurations that either use a different numerical model of ocean cir-

culation, a different geometry, and/or different boundary conditions.

- For fresh continental shelves, typical of East Antarctica, the ASF inhibits an intrinsic variability which is characterised by mixed barotropic-baroclinic instability events that occur every five to ten years and last for approximately half a year. The cross-shelf density gradient weakens during an instability event and allows warm CDW to move closer to the continental shelf. An important outcome is that the instability events are associated with a deep bottom mixed layer at the lower continental slope that develops due to offshore bottom Ekman transport of relatively buoyant continental shelf water. The process was explored in the idealised, zonally symmetric domain with periodic boundary conditions and this thesis informs the modelling community that the mechanism is a robust feature under such conditions.

- The isopycnal structure of the ASF was explored in an idealised domain as well as in the circumpolar domain developed by Naughten et al. (2018a). Sensitivity experiments performed on the idealised domain allowed thresholds to be defined between the different regimes as a function of the applied surface mechanical and buoyancy forcing. In steady state, three different regimes have been simulated. These are "no front", an "offshore single-sided front", and an "onshore single-sided front". The occurrence of the latter has not been suggested in the literature before, but it has been argued in the thesis that some of the observations (e.g., in the northwestern Weddell Sea) could be interpreted in favour of its existence.
  Conversely, the "double-sided front" has attained a lot of attention in the literature. New insights from this thesis suggest that it must be understood as a transient feature between a fresh and a dense continental shelf. This finding is based on transient experiments with a changing surface forcing over time, which translate to changing conditions when following the ASF along the coastline in the Lagrangian framework. Enduring dense shelf conditions will ultimately result in an onshore single-sided front.
  A geographical classification of the present day (2009-2011) ASF shape

was performed based on the modelled density field of the circumpolar configuration. The classification suffers under a grid resolution that is not fully eddy-resolving, but constitutes the first model-based circumpolar classification and complements the observation-based classification performed by Thompson et al. (2018).

- Basal freshwater affects the circulation over the entire continental shelf break system. Locally, it enhances the cavity circulation and drives higher basal melt rates. Non-locally, it freshens the continental shelf over the entire water column as opposed to freshening at the surface only which would increase the stratification. As a consequence, the cross-slope density gradient strengthens. The ASF frontal structure increasingly shows the signal of an offshore single-sided front and the along-slope transport increases (22% for a quadrupled basal freshwater flux and 8% for a doubled basal freshwater flux).
  A negative and a positive feedback mechanism between the ice shelf basal melting, the dynamics at the continental shelf break, and oceanic heat supply were presented. The negative feedback involves a reduction in the heat supply to the continental shelf by the strengthening of the ASF and the associated ASC that inhibit cross-slope heat exchange. This situation was observed around most of the coastline and studied in more detail along the East Antarctic margin. This negative feedback, which counteracts the warming the Antarctic continental shelf seas that is related to the changing atmosphere, ultimately acts to protect the ice shelf cavities.
  A positive feedback mechanism was also observed, e.g., in the Amundsen Sea. Here, increased along-slope transport results in the advection of heat from upstream, and warming of the continental shelf, increasing ice shelf basal melt rates. The observed dynamical changes favour the mass loss of the neighbouring ice shelves.

To conclude, two different configurations of ROMS have been used to advance the understanding of the dynamics of the ASF. While numerical models are challenged by the smallness of the Rossby radius of deformation, which requires a high grid resolution, they have again proven to be a use-

ful tool to study the high southern latitudes, which remain undersampled. The two different model configurations used in this thesis complement each other. The idealised channel configuration resolves mesoscale ocean features and the circumpolar configuration incorporates the interaction between different regions and variations in geometry. The approach taken in this thesis is exemplary of the need for a variety of tools to study the highly complex region that the Antarctic continental shelf break system is.

Outlook

Several objectives for future work, which would extend and build upon the findings of this thesis, are outlined below.

- Intrinsic variability of the ASF was found to be a robust feature in the idealised channel configuration. To investigate the evolution of the deep bottom mixed layer in a submesoscale regime stands out as a future priority.
  Due to the relatively low resolution of the circumpolar configuration, it was not possible to identify susceptible regions in the realistic domain. Regional configurations of continental shelves that are characterised by relatively buoyant shelf waters should be explored for the presence of this mechanism to assess if the instability persists when a more complex bathymetry (i.e. not zonally symmetric) is prescribed.

- The focus of this thesis was to investigate the role of surface forcing and of basal buoyancy forcing on the stability and frontal structure of the ASF. While some findings can be relevant to understand the dynamics of the ASF in regards to global warming, other modes of variability, such as the Southern Annular Mode, are also important. A valuable next step would be to analyse the relationship between large scale atmospheric patterns and the ASF.

- The ASF is sensitive to many different parameters, only a few of which were tested in this thesis. While the geometry of the continental shelf has been the focus of previous works, the role of tides has been neglected

thus far. Pioneering studies suggest tides play an important role in the overturning at the continental shelf break, and suggest that future model configurations should take the effect of tides into account.

- Lastly, this thesis looked at the Antarctic continental shelf break as it poses a barrier to cross-slope heat transport due the large topographic PV gradient. Likewise, the ice shelf front results in a change in water column thickness over a short distance. Even if modified CDW enters the continental shelf, it has to pass this second barrier in order to access the ice shelf cavity and drive basal melting. An important next step is therefore an investigation of this second dynamical barrier, the ice shelf front. An important aspect to consider is how the two barriers interact and which barrier has a stronger control on ocean heat supply on different timescales.

Appendix A

The process model

A.1 Process model parameter choices

The parameter choices for the process model of the Antarctic continental shelf break are given in Tables A.1 and A.2. The forcing and domain specific parameters are prescribed analytically. Tables A.3 and A.4 list all options that were used to perform the simulation, including the advection and mixing scheme. The Coriolis parameter that varies linearly on a $\beta-$plane is calculated as

$$f = f_0 + \beta(y(j) - 550000)$$

with

$$f_0 = -1.31 \cdot 10^{-4}\,\mathrm{s}^{-1}, \qquad \beta = 8.89 \cdot 10^{-12}\,\mathrm{m}^{-1}\mathrm{s}^{-1}, \qquad y(0) = 0\,\mathrm{m}.$$

The applied background vertical mixing coefficient for momentum is with 10^{-3} m^2 s^{-1} relatively large. A simulation with a smaller background value (10^{-5} m^2 s^{-1}) performed on a coarser grid resolution of 3 km revealed no changes in the occurrence or duration of the discussed intrinsic variability. The ice-shelf/ocean specific options of Table A.4 are not part of the standard ROMS distribution. Please, contact the corresponding author regarding code accessibility.

A.2 Grid resolution analysis

This study uses a horizontal resolution of 1 km and 30 vertical layers. To resolve the mesoscale in the study area poses a challenge not only to global

Table A.1: Parameter choice for the process model of the Antarctic continental shelf break, part 1.

Parameter	Value	Description
L_x	400 km	Domain length
L_y	550 km	Domain width
H	3000 m	Maximum depth
H_s	500 m	Continental shelf depth
L_{sl}	150 km	Continental slope width
L_{slc}	300 km	Centre continental slope
L_{ic}	100 km	Ice shelf draft width
L_{icf}	5 km	Ice shelf front width
H_{ic}	480 m	Maximum depth ice shelf draft
H_{icf}	200 m	Depth ice shelf front
L_τ	200 km	Linear decrease of zonal momentum stress
		Zero meridional momentum stress
f_0	$-1.31 \cdot 10^{-4}$ s^{-1}	Coriolis parameter, f-plane constant
β	$8.89 \cdot 10^{-12}$ s^{-1}m^{-1}	Coriolis parameter, beta-plane constant
Δ_t	120 s / 30 s	Baroclinic / barotropic time step
Δ_h	1 km	Horizontal grid spacing
N	30	Number of vertical layers
$V_{transform}$	2	Transformation equation (vertical S-coordinate)
$V_{stretching}$	1	Stretching function
$\theta_{s,b}$	4 / 1	Surface / bottom stretching parameter
T_{cline}	20 m	Minimum water column thickness

Table A.2: Parameter choice for the process model of the Antarctic continental shelf break, part 2.

Parameter	Value	Description
ρ_0	1027 kg m^3	Reference density for Boussinesq approximation
τ_{zon}	-0.05 m^2 s^{-2}	Zonal surface momentum stress minimum
τ_{mer}	0.025 m^2 s^{-2}	Meridional surface momentum stress maximum
T_{sf}	-1.85°C	Surface relaxation temperature
T_{br}	-1.8°C	Maximum surface temperature to allow salt flux
S_{sf}	34.45	Surface relaxation salinity
t_{sf}	60 d	Relaxation time scale surface tracer flux
t_{nb}	1 d	Relaxation time scale northern boundary
tnu_2	3 m^2 s^{-1}	Horizontal harmonic mixing coefficient for tracer
$visc_2$	40 m^2 s^{-1}	Horizontal harmonic mixing coefficient for momentum
Akt_{bak}	$5 \cdot 10^{-5}$ m^2 s^{-1}	Background vertical mixing coefficient for tracer
Akv_{bak}	10^{-3} m^2 s^{-1}	Background vertical mixing coefficient for momentum
R_2	$3 \cdot 10^{-3}$	Quadratic bottom drag coefficient

Table A.3: Overview of the used standard ROMS CPP options.

Option	Description
UV_ADV	Advection terms in momentum equations
UV_COR	Coriolis term in momentum equations
UV_VIS2	Harmonic horizontal mixing in momentum equations
SPLINES_VVISC	Splines reconstruction of vertical mixing
UV_QGRAD	Quadratic bottom friction in momentum equations
TS_C4HADVECTION	4^{th}-order centred horizontal advection
TS_C4VADVECTION	4^{th}-order centred vertical advection
TS_DIF2	Harmonic horizontal mixing
SALINITY	Salinity
SPLINES_VDIFF	Splines reconstruction of vertical diffusion
DJ_GRADPS	Splines density Jacobian (Shchepetkin, 2000)
SOLVE3D	Solving 3D primitive equations
NONLIN_EOS	Nonlinear equation of state
AVERAGES	Writing out time-averaged data
MIX_GEO_UV	Horizontal mixing of momentum on geopotential (constant z)
MIX_GEO_TS	Horizontal mixing of tracer on geopotential (constant z)
LMD_MIXING	Large et al. (2000) interior closure
LMD_CONVEC	Convection mixing due to shear instability
LMD_DDMIX	Double-diffusive mixing
LMD_RMIX	Diffusivity due to shear instability
LMD_SKPP	Surface boundary layer KPP mixing
ANA_GRID	Analytical model grid setup
ANA_INITIAL	Analytical initial conditions
ANA_SMFLUX	Analytical surface momentum stress
ANA_TOBC	Analytical tracers boundary conditions

Table A.4: Overview of the used CPP options unique to the ice-shelf/ocean ROMS version.

Option	Description
ICESHELF	Include ice shelf cavities
ICESHELF_3EQN_VBC	3-equation ice/ocean thermodynamics
ANA_SEAICE	Simple open ocean sea ice model
SEAICE_WINTER	Prescribe constant winter surface fluxes

circulation models, but also regional models because of the small Rossby deformation radius at high latitudes. Previous studies suggested that a horizontal resolution in the order of 1 km is required (Nøst et al., 2011; Dinniman et al., 2012; St-Laurent et al., 2013; Hattermann et al., 2014; Stewart and

Thompson, 2015). To test the resolution dependency in our idealised setup we use a 20 year mean (10 year mean for the 500 m run) of the net melt rate and EKE as control variables (Figure A.1). Six simulations were run with grid resolutions of 0.5 km, 1 km, 2 km, 3 km, 4 km and 5 km, the coarsest being comparable to what is considered to be a relatively high resolution global model (1/10°).

The net melt rate converges at 1 km horizontal resolution (Figure A.1a). Note that the net melt rate for all simulations is very small, because of cold ice shelf cavity temperatures. The lack of lateral boundaries in the model change the cavity circulation which reduces the exchange with the continental shelf and keeps the cavity water cold (Figure 2.3c and 2.3d). The EKE converges towards 1 km and then jumps towards a value about twice as large for 500 m horizontal resolution (Figure A.1b). This simulation starts to resolve submesoscale turbulence as seen from a sudden increase in the Rossby number

$$\mathrm{Ro} = \frac{\zeta}{f}, \tag{A.1}$$

where

$$\zeta = \frac{\partial u}{\partial y} - \frac{\partial v}{\partial x} \tag{A.2}$$

is the vertical component of the relative vorticity (Figure A.1c).

A limited number of test simulations with double vertical resolution for 1 km and 2 km horizontal resolution show a similar behaviour to the 500 m run (not shown). However, doubling the vertical resolution leads to large pressure gradient errors, especially at the ice shelf front, which is why they are not used for the analysis. Pressure gradient errors at steep bathymetry are a known issue for models with terrain-following vertical coordinate systems (Haney, 1991). Even for the vertical grid with 30 layers, the spurious velocities that occur at the ice shelf front are 8.5 cm s^{-1}. Along the continental slope which is the primary region of interest in this study, however, they reduce to reasonable values of less than 0.2 cm s^{-1} (0.7% of modelled ASC).

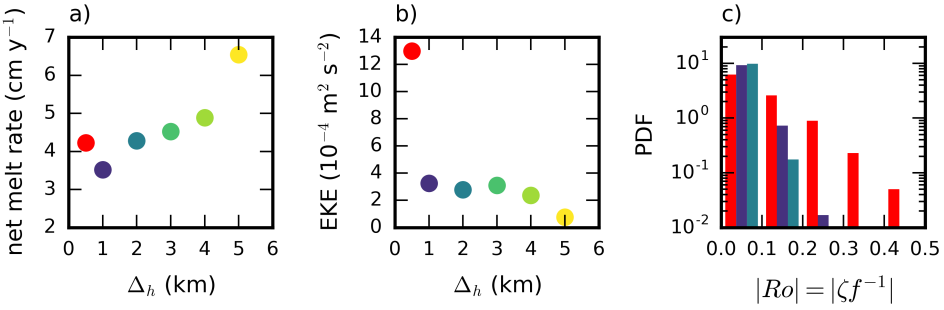

Figure A.1: Comparison of different horizontal grid resolutions Δ_h, each given a separate colour. a) Net melt rate (excluding melting at the ice shelf front), b) mean EKE on the continental slope (between blue and green line in Figure 2.3c and 2.3d) normalised histogram of Rossby number Ro at the third layer from the bottom on the continental slope for the three highest grid resolutions.

A.3 Surface restoring

The ocean surface is restored and an analytical expression is used to calculate the surface tracer flux F_{sf}. For a surface grid cell with height H_z, the tracer flux is given by the difference between the prescribed tracer value T_{sf} and the tracer value T prior to the relaxation, relative to a relaxation time scale t_{sf}:

$$F_{sf} = H_z \cdot \frac{1}{t_{sf}}(T_{sf} - T) \tag{A.3}$$

The chosen relaxation values for temperature and salinity match the density at 500 m depth of the northern boundary profile. This introduces convection to roughly that depth in the southern part of the domain where the influence of the northern boundary decreases. Note a constraint that is added for the salt flux. Only if surface temperatures prior to relaxation are close to surface freezing point (colder than T_{br} =-1.8°C), the salt flux will be non-zero. The resulting salt flux on the continental shelf is on average $7 \cdot 10^{-8}$ psu m s^{-1}. This indirectly implies the effect of brine rejection during sea ice formation. T_{br} is warmer than the surface freezing point temperature to increase the temperature range that permits a salt flux that represents sea ice growth.

Appendix B

Additional Figures (Chapter 4)

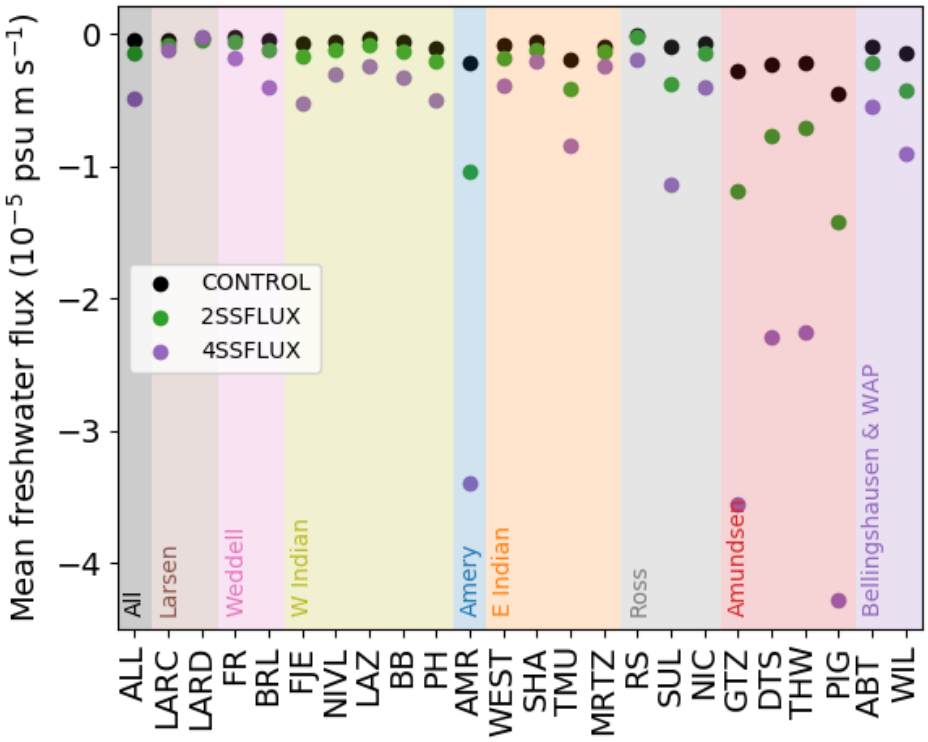

Figure B.1: Average basal freshwater flux per ice shelf for each simulation. Labels indicate the individual ice shelves: ALL indicates all Ice Shelves, LARC indicates Larsen C Ice Shelf, LARD indicates Larsen D Ice Shelf, FR indicates Filchner-Ronne Ice Shelf, BRL indicates Brunt & Riiser-Larsen ice shelves, FJE indicates Fimbul & Jelbart & Ekstrom ice shelves, NIVL indicates Nivel Ice Shelf, LAZ indicates Lazarev Ice Shelf, BB indicates Baudouin & Borchgrevink ice shelves, PH indicates Prince Harald Ice Shelf, AMR indicates Amery Ice Shelf, WEST indicates West Ice Shelf, SHA indicates Shackelton Ice Shelf, TMU indicates Totten & Moscow University ice shelves, MRTZ indicates Mertz Ice Shelf, RS indicates Ross Ice Shelf, SUL indicates Sulzberger Ice Shelf, NIC indicates Nickerson Ice Shelf, GTZ indicates Getz Ice Shelf, DTS indicates Dotsen Ice Shelf, THW indicates Thwaites Ice Shelf, PIG indicates Pine Island Ice Shelf, ABT indicates Abbot Ice Shelf, and WIL indicates Wilkins & George VI & Stange ice shelves.

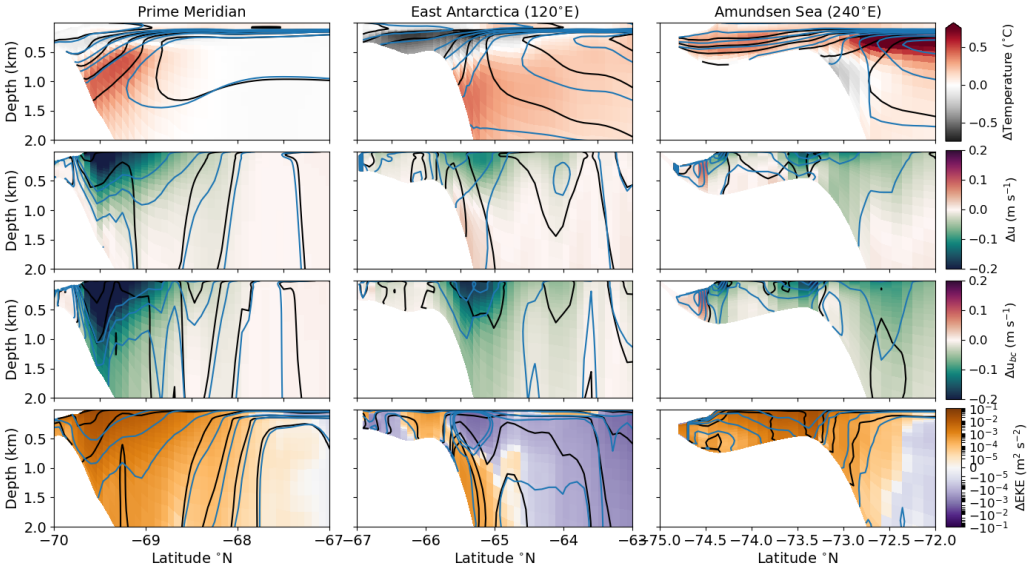

Figure B.2: Cross-slope sections showing in shading the difference between the perturbation experiment 4SSFLUX and the CONTROL run for a) temperature, b) zonal velocity, c) baroclinic component of the zonal velocity (calculated as zonal velocity minus depth-averaged zonal velocity), and d) eddy kinetic energy. The black contours correspond to the full field of the CONTROL run and the blue contours to that of the perturbation experiment 4SSFLUX.

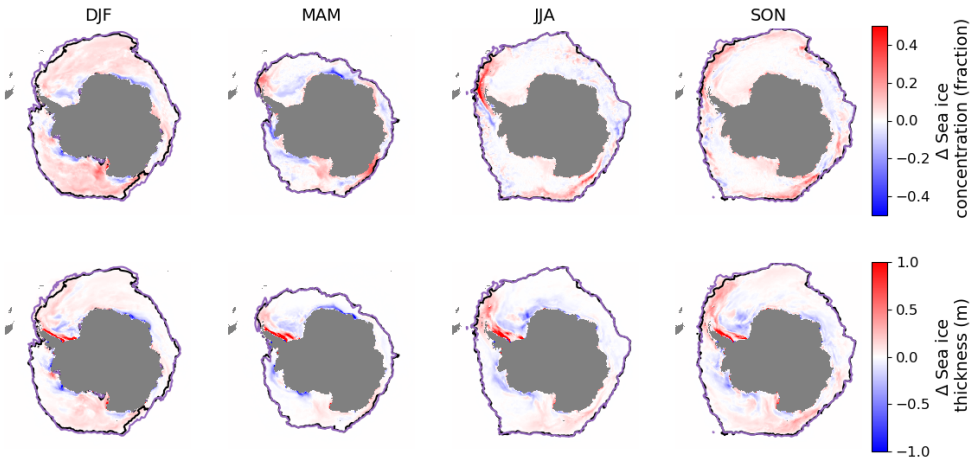

Figure B.3: Changes between the perturbation experiment 4SSFLUX and CONTROL for sea ice area (top) and sea ice thickness (bottom) per season (DJF: December, January, February; MAM: March, April, May; JJA: June, July, August; SON: September, October, November). The contour shows the maximum sea ice extent for CONTROL (black) and 4SSFLUX (purple). The plotted area goes further north than in Figure 4.8 in order to display the full sea ice extent.

REFERENCES

Amblas, D. and Dowdeswell, J. A. (2018). Physiographic influences on dense shelf-water cascading down the Antarctic continental slope. *Earth-Science Reviews*, 185:887–900.

Aoki, S., Sasai, Y., Sasaki, H., Mitsudera, H., and Williams, G. D. (2010). The cyclonic circulation in the Australian-Antarctic basin simulated by an eddy-resolving general circulation model. *Ocean Dynamics*, 60:743–757.

Armitage, T. W., Kwok, R., Thompson, A. F., and Cunningham, G. (2018). Dynamic topography and sea level anomalies of the Southern Ocean: Variability and teleconnections. *Journal of Geophysical Research: Oceans*, 123:613–630.

Asay-Davis, X. S., Jourdain, N. C., Nakayama, Y., and Jourdain, N. C. (2017). Developments in simulating and parameterizing interactions between the Southern Ocean and the Antarctic ice sheet. *Current Climate Change Reports*, 3:316–329.

Azaneu, M. V. C., Heywood, K. J., Queste, B. Y., and Thompson, A. F. (2017). Variability of the Antarctic Slope Current system in the northwestern Weddell Sea. *Journal of Physical Oceanography*, 47:2977–2997.

Baines, P. G. and Condie, S. (1998). Observations and modelling of Antarctic downslope flows: A review. *Antarctic Research Series*, 75:29–49.

Bamber, J., Riva, R., and Vermeersen, B. (2009). Reassessment of the potential contribution to sea level from a collapse of the West Antarctic Ice Sheet. *IOP Conference Series: Earth and Environmental Science*, 6:012004.

Bindoff, N. L., Rosenberg, M. A., and Warner, M. J. (2000). On the circulation and water masses over the Antarctic continental slope and rise between 80 and 150 E. *Deep-Sea Research Part II: Topical Studies in Oceanography*, 47:2299–2326.

Bintanja, R., Van Oldenborgh, G. J., Drijfhout, S. S., Wouters, B., and Katsman, C. A. (2013). Important role for ocean warming and increased ice-shelf melt in Antarctic sea-ice expansion. *Nature Geoscience*, 6:376–379.

Bintanja, R., Van Oldenborgh, G. J., and Katsman, C. A. (2015). The effect of increased fresh water from Antarctic ice shelves on future trends in Antarctic sea ice. *Annals of Glaciology*, 56:120–126.

REFERENCES

Bronselaer, B., Winton, M., Griffies, S. M., Hurlin, W. J., Rodgers, K. B., Sergienko, O. V., Stouffer, R. J., and Russell, J. L. (2018). Change in future climate due to Antarctic meltwater. *Nature*, 564:53–58.

Cerovečki, I., Talley, L. D., and Mazloff, M. R. (2011). A comparison of southern ocean air-sea buoyancy flux from an ocean state estimate with five other products. *Journal of Climate*, 24(24):6283–6306.

Chavanne, C. P., Heywood, K. J., Nicholls, K. W., and Fer, I. (2010). Observations of the Antarctic Slope undercurrent in the southeastern Weddell Sea. *Geophysical Research Letters*, 37:3–7.

Church, J., Clark, P., Cazenave, A., Gregory, J., Jevrejeva, S., Levermann, A., Merrifield, M., Milne, G., Nerem, R., Nunn, P., Payne, A., Pfeffer, W., Stammer, D., and Unnikrishnan, A. (2013). Sea level change. *Climate Change 2013: The Physical Science Basis. Contribution of Working Group I to the Fifth Assessment Report of the Intergovernmental Panel on Climate Change*, pages 1137–1216.

Cole, S. T., Timmermans, M.-L., Toole, J. M., Krishfield, R. A., and Thwaites, F. T. (2014). Ekman veering, internal waves, and turbulence observed under Arctic sea ice. *Journal of Physical Oceanography*, 44:1306–1328.

Connolley, W. M., Gregory, J. M., Hunke, E. C., and Mclaren, A. J. (2004). On the consistent scaling of terms in the sea-ice dynamics equation. *Journal of Physical Oceanography*, 34:1776–1780.

Cougnon, E. A., Galton-Fenzi, B. K., Meijers, A. J. S., and Legrésy, B. (2013). Modeling interannual dense shelf water export in the region of the Mertz Glacier Tongue (1992-2007). *Journal of Geophysical Research: Oceans*, 118:5858–5872.

Cushman-Roisin, B. and Beckers, J.-M. (2011). *Introduction to Geophysical Fluid Dynamics - Physical and Numerical Aspects*. Academic Press.

Daae, K., Hattermann, T., Darelius, E., and Fer, I. (2017). On the effect of topography and wind on warm water inflow - An idealized study of the southern Weddell Sea continental shelf system. *Journal of Geophysical Research: Oceans*, 122:2622–2641.

De Rydt, J., Holland, P. R., Dutrieux, P., and Jenkins, A. (2014). Geometric and oceanographic controls on melting beneath Pine Island Glacier. *Journal of Geophysical Research: Oceans*, 119:2420–2438.

Debernard, J. B., Kristensen, N. M., Maartensson, S., Wang, K., and Waagbo, G. A. (2017). metno/metroms: Intermediate release.

REFERENCES

Dee, D. P., Uppala, S. M., Simmons, A. J., Berrisford, P., Poli, P., Kobayashi, S., Andrae, U., Balmaseda, M. A., Balsamo, G., Bauer, P., Bechtold, P., Beljaars, A. C., van de Berg, L., Bidlot, J., Bormann, N., Delsol, C., Dragani, R., Fuentes, M., Geer, A. J., Haimberger, L., Healy, S. B., Hersbach, H., Hólm, E. V., Isaksen, L., Kållberg, P., Köhler, M., Matricardi, M., Mcnally, A. P., Monge-Sanz, B. M., Morcrette, J. J., Park, B. K., Peubey, C., de Rosnay, P., Tavolato, C., Thépaut, J. N., and Vitart, F. (2011). The ERA-Interim reanalysis: Configuration and performance of the data assimilation system. *Quarterly Journal of the Royal Meteorological Society*, 137:553–597.

Depoorter, M. A., Bamber, J. L., Griggs, J. A., Lenaerts, J. T. M., Ligtenberg, S. R. M., van den Broeke, M. R., and Moholdt, G. (2013). Calving fluxes and basal melt rates of Antarctic ice shelves. *Nature*, 502:89–92.

Dinniman, M. S., Asay-Davis, X. S., Galton-Fenzi, B. K., Holland, P. R., Jenkins, A., and Timmermann, R. (2016). Modeling ice shelf/ocean interaction in Antarctica: A review. *Oceanography*, 29:144–153.

Dinniman, M. S., Klinck, J. M., and Hofmann, E. E. (2012). Sensitivity of Circumpolar Deep Water transport and ice shelf basal melt along the West Antarctic Peninsula to changes in the winds. *Journal of Climate*, 25:4799–4816.

Dinniman, M. S., Klinck, J. M., and Smith, W. O. (2011). A model study of Circumpolar Deep Water on the West Antarctic Peninsula and Ross Sea continental shelves. *Deep Sea Research Part II: Topical Studies in Oceanography*, 58:1508–1523.

Dowdeswell, J. A. (2006). The Greenland Ice Sheet and Global Sea-Level Rise. *Science*, 311:963–965.

Dupont, T. K. and Alley, R. B. (2005). Assessment of the importance of ice-shelf buttressing to ice-sheet flow. *Geophysical Research Letters*, 32:1–4.

Dutrieux, P. (2014). Strong Sensitivity of Pine Island Ice-Shelf. *Science*, 343:174–179.

Fer, I., Darelius, E., and Daae, K. B. (2016). Observations of energetic turbulence on the Weddell Sea continental slope. *Geophysical Research Letters*, 43:760–766.

Flexas, M. D. M., Schodlok, M. P., Padman, L., Menemenlis, D., and Orsi, A. H. (2015). Role of tides on the formation of the Antarctic Slope Front at the Weddell-Scotia Confluence. *Journal of Geophysical Research: Oceans*, 120:3658–3680.

Fogwill, C. J., Phipps, S. J., Turney, C. S., and Golledge, N. R. (2015). Sensitivity of the Southern Ocean to enhanced regional Antarctic ice sheet meltwater input. *Earth's Future*, 3:317–329.

Foldvik, A., Gammelsrod, T., Osterhus, S., Fahrbach, E., Rohardt, G., Schroeder, M., Nicholls, K. W., Padman, L., and Woodgate, R. A. (2004). Ice shelf water overflow and bottom water formation in the southern Weddell Sea. *Journal of Geophysical Research*, 109:C02015.

Fretwell, P., Pritchard, H. D., Vaughan, D. G., Bamber, J. L., Barrand, N. E., Bell, R., Bianchi, C., Bingham, R. G., Blankenship, D. D., Casassa, G., Catania, G., Callens, D., Conway, H., Cook, A. J., Corr, H. F. J., Damaske, D., Damm, V., Ferraccioli, F., Forsberg, R., Fujita, S., Gim, Y., Gogineni, P., Griggs, J. A., Hindmarsh, R. C. A., Holmlund, P., Holt, J. W., Jacobel, R. W., Jenkins, A., Jokat, W., Jordan, T., King, E. C., Kohler, J., Krabill, W., Riger-Kusk, M., Langley, K. A., Leitchenkov, G., Leuschen, C., Luyendyk, B. P., Matsuoka, K., Mouginot, J., Nitsche, F. O., Nogi, Y., Nost, O. A., Popov, S. V., Rignot, E., Rippin, D. M., Rivera, A., Roberts, J., Ross, N., Siegert, M. J., Smith, A. M., Steinhage, D., Studinger, M., Sun, B., Tinto, B. K., Welch, B. C., Wilson, D., Young, D. A., Xiangbin, C., and Zirizzotti, A. (2013). Bedmap2: improved ice bed, surface and thickness datasets for Antarctica. *The Cryosphere*, 28:63–86.

Galton-Fenzi, B. K. (2009). *Modelling ice-shelf/ocean interaction.* PhD thesis, University of Tasmania.

Galton-Fenzi, B. K., Hunter, J. R., Coleman, R., Marsland, S. J., and Warner, R. C. (2012). Modeling the basal melting and marine ice accretion of the Amery Ice Shelf. *Journal of Geophysical Research: Oceans*, 117:C09031.

Garabato, A. C. N., Forryan, A., Dutrieux, P., Brannigan, L., Biddle, L. C., Heywood, K. J., Jenkins, A., Firing, Y. L., and Kimura, S. (2017). Vigorous lateral export of the meltwater outflow from beneath an Antarctic ice shelf. *Nature*, 542(7640):219–222.

Gill, A. E. (1973). Circulation and bottom water production in the Weddell Sea. *Deep-Sea Research*, 20:111–140.

Goddard, P. B., Dufour, C. O., Yin, J., Griffies, S. M., and Winton, M. (2017). CO2-Induced Ocean Warming of the Antarctic Continental Shelf in an Eddying Global Climate Model. *Journal of Geophysical Research: Oceans*, 122:8079–8101.

Graham, J. A., Dinniman, M. S., and Klinck, J. M. (2016). Impact of model resolution for on-shelf heat transport along the West Antarctic Peninsula. *Journal of Geophysical Research: Oceans*, 121:7880–7897.

Greenbaum, J. S., Blankenship, D. D., Young, D. A., Richter, T. G., Roberts, J. L., Aitken, A. R. A., Legresy, B., Schroeder, D. M., Warner, R. C., van Ommen, T. D., and Siegert, M. J. (2015). Ocean access to a cavity beneath Totten Glacier in East Antarctica. *Nature Geoscience*, 8:294–298.

Gwyther, D. E., Galton-Fenzi, B. K., Hunter, J. R., and Roberts, J. L. (2014). Simulated melt rates for the Totten and Dalton ice shelves. *Ocean Science*, 10:267–279.

Hallberg, R. (2013). Using a resolution function to regulate parameterizations of oceanic mesoscale eddy effects. *Ocean Modelling*, 72:92–103.

Haney, R. L. (1991). On the pressure gradient force over steep topography in sigma coordinate ocean models. *Journal of Physical Oceanography*, 21:610–619.

Hattermann, T. (2018). Antarctic thermocline dynamics along a narrow shelf with easterly winds. *Journal of Physical Oceanography*, 48:2419–2443.

Hattermann, T., Nost, O. A., Lilly, J. M., and Smedsrud, L. H. (2012). Two years of oceanic observations below the Fimbul Ice Shelf, Antarctica. *Geophysical Research Letters*, 39:1–6.

Hattermann, T., Smedsrud, L. H., Nøst, O. A., Lilly, J. M., and Galton-Fenzi, B. K. (2014). Eddy-resolving simulations of the Fimbul Ice Shelf cavity circulation: Basal melting and exchange with open ocean. *Ocean Modelling*, 82:28–44.

Hellmer, H. H. (2004). Impact of Antarctic ice shelf basal melting on sea ice and deep ocean properties. *Geophysical Research Letters*, 31:1–4.

Hellmer, H. H., Kauker, F., Timmermann, R., Determann, J., and Rae, J. (2012). Twenty-first-century warming of a large Antarctic ice-shelf cavity by a redirected coastal current. *Nature*, 485:225–228.

Hellmer, H. H. and Olbers, D. (1989). A two-dimensional model for the thermohaline circulation under an ice shelf. *Antarctic Science*, 1:325–336.

Heywood, K. J. and King, B. A. (2002). Water masses and baroclinic transports in the South Atlantic and Southern oceans. *Journal of Marine Research*, 60:639–676.

Heywood, K. J., Locarnini, R. A., Frew, R. D., Dennis, P. F., and King, B. A. (1998). Transport and water masses of the Antarctic Slope Front system in the eastern Weddell Sea. *Ocean, Ice and Atmosphere: Interactions at the Antarctic Continental Margin, Antarctic Research Series*, 75:203–214.

Heywood, K. J., Naveira Garabato, A. C., Stevens, D. P., and Muench, R. D. (2004). On the fate of the Antarctic Slope Front and the origin of the Weddell Front. *Journal of Geophysical Research: Oceans*, 109:C06021.

Heywood, K. J., Schmidtko, S., Heuzé, C., Kaiser, J., Jickells, T. D., Queste, B. Y., Stevens, D. P., Wadley, M., Thompson, A. F., Fielding, S., Guihen, D., Creed, E., Ridley, J. K., and Smith, W. (2014). Ocean processes at the Antarctic continental slope. *Philosophical Transactions of the Royal Society A*, 372:20130047.

Heywood, K. J., Sparrow, M. D., Brown, J., and Dickson, R. R. (1999). Frontal structure and Antarctic Bottom Water flow through the Princess Elizabeth Trough, Antarctica. *Deep-Sea Research Part I: Oceanographic Research Papers*, 46:1181–1200.

Holland, D. M. and Jenkins, A. (1999). Modeling thermodynamic iceocean interactions at the base of an ice shelf. *Journal of Physical Oceanography*, 29:1787–1800.

Hunke, E. C., Lipscomb, W. H., Turner, A. K., Jeffery, N., and Elliott, S. (2015). CICE: the Los Alamos sea ice model documentation and software user's manual. *Tech. rep., Los Alamos National Laboratory.*

Isachsen, P. E. (2011). Baroclinic instability and eddy tracer transport across sloping bottom topography: How well does a modified Eady model do in primitive equation simulations? *Ocean Modelling*, 39:183–199.

Jacob, R., Larson, J., and Ong, E. (2005). M x N communication and parallel interpolation in community climate system model version 3 using the model coupling toolkit. *International Journal of High Performance Computing Applications*, 19:293–307.

Jacobs, S., Helmer, H., Doake, C. S. M., Jenkins, A., and Frolich, R. M. (1992). Melting of ice shelves and the mass balance of Antarctica. *Journal of Glaciology*, 38:375–387.

Jacobs, S. S. (1991). On the nature and significance of the Antarctic Slope Front. *Marine Chemistry*, 35:9–24.

Jenkins, A. (1999). The impact of melting ice on ocean waters. *Journal of Physical Oceanography*, 29:2370–2381.

Jenkins, A., Dutrieux, P., Jacobs, S., Steig, E., Gudmundsson, H., Smith, J., and Heywood, K. (2016). Decadal Ocean Forcing and Antarctic Ice Sheet Response: Lessons from the Amundsen Sea. *Oceanography*, 29:106–117.

Jourdain, N. C., Mathiot, P., Merino, N., Durand, G., Le Sommer, J., Spence, P., Dutrieux, P., and Madec, G. (2017). Ocean circulation and sea-ice thinning induced by melting ice shelves in the Amundsen Sea. *Journal of Geophysical Research: Oceans*, 122.

Kimura, S., Candy, A. S., Holland, P. R., Piggott, M. D., and Jenkins, A. (2013). Adaptation of an unstructured-mesh, finite-element ocean model to the simulation of ocean circulation beneath ice shelves. *Ocean Modelling*, 67:39–51.

Kimura, S., Jenkins, A., Regan, H., Holland, P. R., Assmann, K. M., Whitt, D. B., van Wessem, M., van de Berg, W. J., Reijmer, C. H., and Dutrieux, P. (2017). Oceanographic Controls on the Variability of Ice-Shelf Basal Melting and Circulation of Glacial Meltwater in the Amundsen Sea Embayment, Antarctica. *Journal of Geophysical Research: Oceans*, 122:131–155.

King, J. (2014). A resolution of the Antarctic paradox. *Nature*, 505:491–492.

Klinck, J. M. and Dinniman, M. S. (2010). Exchange across the shelf break at high southern latitudes. *Ocean Science*, 6:513–524.

Kusahara, K. and Hasumi, H. (2014). Pathways of basal meltwater from Antarctic ice shelves: A model study. *Journal of Geophysical Research: Oceans*, 119:5690–5704.

Kusahara, K. and Ohshima, K. I. (2014). Kelvin Waves around Antarctica. *Journal of Physical Oceanography*, 44:2909–2920.

Large, W. G., McWilliams, J. C., and Doney, S. C. (1994). Oceanic vertical mixing - a review and a model with a nonlocal boundary-layer parameterization. *Reviews of Geophysics*, 32:363–403.

Large, W. G. and Yeager, S. G. (2009). The global climatology of an interannually varying air-sea flux data set. *Climate Dynamics*, 33:341–364.

Larson, J., Jacob, R., and Ong, E. (2005). The model coupling toolkit: A new Fortran90 toolkit for building multiphysics parallel coupled models. *International Journal of High Performance Computing Applications*, 19:277–292.

Lu, P., Li, Z., Cheng, B., and Leppäranta, M. (2011). A parameterization of the ice-ocean drag coefficient. *Journal of Geophysical Research: Oceans*, 116:C07019.

Lüpkes, C. and Birnbaum, G. (2005). Surface drag in the Arctic marginal sea-ice zone: a comparison of different parameterisation concepts. *Boundary-Layer Meteorology*, 117:179–211.

Manucharyan, G. E. and Thompson, A. F. (2017). Submesoscale sea ice-ocean interactions in marginal ice zones. *Journal of Geophysical Research: Oceans*, 122:9455–9475.

Marshall, J. and Speer, K. (2012). Closure of the meridional overturning circulation through Southern Ocean upwelling. *Nature Geoscience*, 5:171–180.

Martin, T. and Adcroft, A. (2010). Parameterizing the fresh-water flux from land ice to ocean with interactive icebergs in a coupled climate model. *Ocean Modelling*, 34:111–124.

Mathiot, P., Goosse, H., Fichefet, T., Barnier, B., and Gallée, H. (2011). Modelling the seasonal variability of the Antarctic Slope Current. *Ocean Science*, 7:455–470.

McKee, D. C., Martinson, D. G., and Schofield, O. (2019). Origin and Attenuation of Mesoscale Structure in Circumpolar Deep Water Intrusions to an Antarctic Shelf. *Journal of Physical Oceanography*, 49:1293–1318.

Meier, W. N., Peng, G., Schott, D. J., and Savoie, M. H. (2013). NOAA/NSIDC cliamte data record of passive microwave sea-ice concentration climate record. *Polar Research*, 33:21004.

Meijers, A. J. S., Klocker, A., Bindoff, N. L., Williams, G. D., and Marsland, S. J. (2010). The circulation and water masses of the Antarctic shelf and continental slope between 30 and 80 E. *Deep Sea Research Part II: Topical Studies in Oceanography*, 57:723–737.

Menemenlis, D., Campin, J. M., Heimbach, P., Hill, C., Lee, T., Nguyen, A., Schodlok, M., and Zhang, H. (2008). ECCO2: High resolution global ocean and sea ice data synthesis. *Mercator Ocean Quaterly Newsletter*, 31:13–21.

Merino, N., Jourdain, N. C., Le Sommer, J., Goosse, H., Mathiot, P., and Durand, G. (2018). Impact of increasing antarctic glacial freshwater release on regional sea-ice cover in the Southern Ocean. *Ocean Modelling*, 121:76–89.

Millero, F. J. (1978). Annex 6: Freezing point of seawater. Eighth report of the joint panel of oceanographic tables and standards. *UNESCO technical Paper Marine Sciences*, 28:29–31.

Moffat, C., Owens, B., and Beardsley, R. C. (2009). On the characteristics of Circumpolar Deep Water intrusions to the west Antarctic Peninsula continental shelf. *Journal of Geophysical Research: Oceans*, 114:C05017.

Mueller, R. D., Hattermann, T., Howard, S. L., and Padman, L. (2018). Tidal influences on a future evolution of the Filchner-Ronne Ice Shelf cavity in the Weddell Sea, Antarctica. *Cryosphere*, 12:453–476.

Nakayama, Y., Timmermann, R., Rodehacke, C. B., Schröder, M., and Hellmer, H. H. (2014a). Modeling the spreading of glacial meltwater from the Amundsen and Bellingshausen Seas. *Geophysical Research Letters*, 41:7942–7949.

Nakayama, Y., Timmermann, R., Schröder, M., and Hellmer, H. H. (2014b). On the difficulty of modeling Circumpolar Deep Water intrusions onto the Amundsen Sea continental shelf. *Ocean Modelling*, 84:26–34.

Naughten, K. A., Galton-Fenzi, B. K., Meissner, K. J., England, M. H., Brassington, G. B., Colberg, F., Hattermann, T., and Debernard, J. B. (2017). Spurious sea ice formation caused by oscillatory ocean tracer advection schemes. *Ocean Modelling*, 116:108–117.

Naughten, K. A., Meissner, K. J., Galton-Fenzi, B. K., and England, M. H. (2018a). Intercomparison of Antarctic ice-shelf, ocean, and sea-ice interactions simulated by MetROMS-iceshelf and FESOM 1.4. *Geoscientific Model Development*, 11:1257–1292.

Naughten, K. A., Meissner, K. J., Galton-Fenzi, B. K., England, M. H., Timmermann, R., and Hellmer, H. H. (2018b). Future projections of Antarctic ice shelf melting based on CMIP5 scenarios. *Journal of Climate*, 31:5243–5261.

Naveira Garabato, A. C., Frajka-Williams, E. E., Spingys, C. P., Legg, S., Polzin, K. L., Forryan, A., Povl Abrahamsen, E., Buckingham, C. E., Griffies, S. M., McPhail, S. D., Nicholls, K. W., Thomas, L. N., and Meredith, M. P. (2019). Rapid mixing and exchange of deep-ocean waters in an abyssal boundary current. *Proceedings of the National Academy of Sciences of the United States of America*, 116:13233–13238.

Nitsche, F. O., Porter, D., Williams, G., Cougnon, E. A., Fraser, A. D., Correia, R., and Guerrero, R. (2017). Bathymetric control of warm ocean water access along the East Antarctic Margin. *Geophysical Research Letters*, 44:8936–8944.

Nøst, O. A., Biuw, M., Tverberg, V., Lydersen, C., Hattermann, T., Zhou, Q., Smedsrud, L. H., and Kovacs, K. M. (2011). Eddy overturning of the Antarctic Slope Front controls glacial melting in the Eastern Weddell Sea. *Journal of Geophysical Research: Oceans*, 116:C11014.

Núñez-Riboni, I. and Fahrbach, E. (2009). Seasonal variability of the Antarctic Coastal Current and its driving mechanisms in the Weddell Sea. *Deep-Sea Research Part I: Oceanographic Research Papers*, 56:1927–1941.

Orsi, A. H. and Whitworth, T. (2005). *Hydrographic Atlas of the World Ocean Circulation Experiment (WOCE) Volume 1: Southern Ocean*. Southampton, UK: WOCE International Project Office.

Padman, L., Howard, S. L., Orsi, A. H., and Muench, R. D. (2009). Tides of the northwestern Ross Sea and their impact on dense outflows of Antarctic Bottom Water. *Deep Sea Research Part II: Topical Studies in Oceanography*, 56:818–834.

Padman, L., Siegfried, M. R., and Fricker, H. A. (2018). Ocean Tide Influences on the Antarctic and Greenland Ice Sheets. *Reviews of Geophysics*, 56:142–184.

Paolo, F. S., Fricker, H. A., and Padman, L. (2015). Volume loss from Antarctic ice shelves is accelerating. *Science*, 348:327–331.

Pauling, A. G., Bitz, C. M., Smith, I. J., and Langhorne, P. J. (2016). The response of the Southern Ocean and Antarctic sea ice to freshwater from ice shelves in an earth system model. *Journal of Climate*, 29:1655–1672.

Pauling, A. G., Smith, I. J., Langhorne, P. J., and Bitz, C. M. (2017). Time-dependent freshwater input from ice shelves: Impacts on Antarctic sea ice and the Southern Ocean in an earth system model. *Geophysical Research Letters*, 44:10,454–10,461.

Peña-Molino, B., McCartney, M. S., and Rintoul, S. R. (2016). Direct observations of the Antarctic Slope Current transport at 113E. *Journal of Geophysical Research: Oceans*, 121:7390–7407.

Pennel, R., Stegner, A., and Béranger, K. (2012). Shelf impact on buoyant coastal current instabilities. *Journal of Physical Oceanography*, 42:39–61.

Petty, A. A., Feltham, D. L., and Holland, P. R. (2013). Impact of atmospheric forcing on Antarctic continental shelf water masses. *Journal of Physical Oceanography*, 43:920–940.

Phipps, S. J., Fogwill, C. J., and Turney, C. S. (2016). Impacts of marine instability across the East Antarctic Ice Sheet on Southern Ocean dynamics. *Cryosphere*, 10:2317–2328.

Pritchard, H. D., Ligtenberg, S. R. M., Fricker, H. A., Vaughan, D. G., van den Broeke, M. R., and Padman, L. (2012). Antarctic ice-sheet loss driven by basal melting of ice shelves. *Nature*, 484:502–505.

Rignot, E., Jacobs, S., Mouginot, J., and Scheuchl, B. (2013). Ice-shelf melting around Antarctica. *Science*, 341:266–270.

Rignot, E., Mouginot, J., Morlighem, M., Seroussi, H., and Scheuchl, B. (2014). Widespread, rapid grounding line retreat of Pine Island, Thwaites, Smith, and Kohler glaciers, West Antarctica, from 1992 to 2011. *Geophysical Research Letters*, 41:3502–3509.

Rignot, E., Mouginot, J., Scheuchl, B., van den Broeke, M., van Wessem, M. J., and Morlighem, M. (2019). Four decades of Antarctic Ice Sheet mass balance from. *Proceedings of the National Academy of Science*, 116:1095–1103.

Rintoul, S. R., Silvano, A., Pena-Molino, B., van Wijk, E., Rosenberg, M., Greenbaum, J. S., and Blankenship, D. D. (2016). Ocean heat drives rapid basal melt of the Totten Ice Shelf. *Science Advances*, 2:e1601610.

Ruan, X., Thompson, A. F., Flexas, M. M., and Sprintall, J. (2017). Contribution of topographically generated submesoscale turbulence to Southern Ocean overturning. *Nature Geoscience*, 10:840–845.

Ryan, S., Hattermann, T., Darelius, E., and Schröder, M. (2017). Seasonal cycle of hydrography on the eastern shelf of the Filchner Trough, Weddell Sea, Antarctica. *Journal of Geophysical Research: Oceans*, 122:6437–6453.

Schmidtko, S., Heywood, K. J., Thompson, A. F., and Aoki, S. (2014). Multidecadal warming of Antarctic waters. *Science*, 346:1227–1231.

Schodlok, M. P., Menemenlis, D., Rignot, E., and Studinger, M. (2012). Sensitivity of the ice-shelf/ocean system to the sub-ice-shelf cavity shape measured by

NASA IceBridge in Pine Island Glacier, West Antarctica. *Annals of Glaciology*, 53:156–162.

Schoof, C. (2007). Ice sheet grounding line dynamics: steady states, stability, and hysteresis. *Journal of Geophysical Research*, 112:F03S28.

Shchepetkin, A. F. and McWilliams, J. C. (2005). The regional oceanic modeling system (ROMS): A split-explicit, free-surface, topography-following-coordinate oceanic model. *Ocean Modelling*, 9:347–404.

Silvano, A., Rintoul, S. R., and Herraiz-Borreguero, L. (2016). Ocean-ice shelf interaction in East Antarctica. *Oceanography*, 29:130–143.

Silvano, A., Rintoul, S. R., Peña-Molino, B., Hobbs, W. R., van Wijk, E., Aoki, S., Tamura, T., and Williams, G. D. (2018). Freshening by glacial meltwater enhances melting of ice shelves and reduces formation of Antarctic Bottom Water. *Science Advances*, 4:eaap9467.

Spence, P., Holmes, R. M., Hogg, A. M., Griffies, S. M., Stewart, K. D., and England, M. H. (2017). Localized rapid warming of West Antarctic subsurface waters by remote winds. *Nature Climate Change*, 7:595–603.

St-Laurent, P., Klinck, J. M., and Dinniman, M. S. (2013). On the role of coastal troughs in the circulation of warm Circumpolar Deep Water on Antarctic shelves. *Journal of Physical Oceanography*, 43:51–64.

Stern, A., Nadeau, L.-P., and Holland, D. (2015). Instability and Mixing of Zonal Jets along an Idealized Continental Shelf Break. *Journal of Physical Oceanography*, 45:2315–2338.

Stewart, A. L., Klocker, A., and Menemenlis, D. (2018). Circum-Antarctic shoreward heat transport derived from an eddy- and tide-resolving simulation. *Geophysical Research Letters*, 45.

Stewart, A. L. and Thompson, A. F. (2013). Connecting Antarctic cross-slope exchange with Southern Ocean overturning. *Journal of Physical Oceanography*, 43:1453–1471.

Stewart, A. L. and Thompson, A. F. (2015). Eddy-mediated transport of warm Circumpolar Deep Water across the Antarctic shelf break. *Geophysical Research Letters*, 42:432–440.

Stewart, A. L. and Thompson, A. F. (2016). Eddy generation and jet formation via dense water outflows across the Antarctic continental slope. *Journal of Physical Oceanography*, 46:3729–3750.

Swart, N. C. and Fyfe, J. C. (2013). The influence of recent Antarctic ice sheet retreat on simulated sea ice area trends. *Geophysical Research Letters*, 40:4328–4332.

Thoma, M., Jenkins, A., Holland, D., and Jacobs, S. (2008). Modelling Circumpolar Deep Water intrusions on the Amundsen Sea continental shelf, Antarctica. *Geophysical Research Letters*, 35:L18602.

Thompson, A. F. and Heywood, K. J. (2008). Frontal structure and transport in the northwestern Weddell Sea. *Deep-Sea Research Part I: Oceanographic Research Papers*, 55:1229–1251.

Thompson, A. F., Heywood, K. J., Schmidtko, S., and Stewart, A. L. (2014). Eddy transport as a key component of the Antarctic overturning circulation. *Nature Geoscience*, 7:879–884.

Thompson, A. F., Stewart, A. L., Spence, P., and Heywood, K. J. (2018). The Antarctic Slope Current in a changing climate. *Reviews of Geophysics*, 56.

Timmermann, R. and Beckmann, A. (2004). Parameterization of vertical mixing in the Weddell Sea. *Ocean Modelling*, 6:83–100.

Timmermann, R., Le Brocq, A., Deen, T., Domack, E., Dutrieux, P., Galton-Fenzi, B., Hellmer, H., Humbert, A., Jansen, D., Jenkins, A., Lambrecht, A., Makinson, K., Niederjasper, F., Nitsche, F., Nøst, O. A., Smedsrud, L. H., and Smith, W. H. F. (2010). A consistent dataset of Antarctic ice sheet topography, cavity geometry, and global bathymetry. *Earth System Science Data Discussions*, 3:231–257.

Wåhlin, A. K., Yuan, X., Björk, G., and Nohr, C. (2010). Inflow of Warm Circumpolar Deep Water in the Central Amundsen Shelf. *Journal of Physical Oceanography*, 40:1427–1434.

Walker, D. P., Jenkins, A., Assmann, K. M., Shoosmith, D. R., and Brandon, M. A. (2013). Oceanographic observations at the shelf break of the Amundsen Sea, Antarctica. *Journal of Geophysical Research: Oceans*, 118(6):2906–2918.

Webb, D. J., Holmes, R. M., Spence, P., and England, M. H. (2019). Barotropic Kelvin Wave-Induced Bottom Boundary Layer Warming Along the West Antarctic Peninsula. *Journal of Geophysical Research: Oceans*, 124:1595–1615.

Weertman, J. (1974). Stability of the Junction of an Ice Sheet and an Ice Shelf. *Journal of Glaciology*, 13:3–11.

Whitworth, T., Orsi, A. H., Kim, S. J., Nowlin, W. D., and Locarnini, R. A. (1998). Water masses and mixing near the Antarctic Slope Front. *Ocean, Ice and Atmosphere: Interactions at the Antarctic Continental Margin, Antarctic Research Series*, 75:1–27.

Williams, G. D., Meijers, A. J. S., Poole, A., Mathiot, P., Tamura, T., and Klocker, A. (2011). Late winter oceanography off the Sabrina and BANZARE coast (117-128 E), East Antarctica. *Deep-Sea Research Part II: Topical Studies in Oceanography*, 58:1194–1210.

Williams, P. D., Read, P. L., and Haine, T. W. (2010). Testing the limits of quasi-geostrophic theory: Application to observed laboratory flows outside the quasi-geostrophic regime. *Journal of Fluid Mechanics*, 649:187–203.

Wunsch, C., Heimbach, P., Ponte, R. M., and Fukumori, I. (2009). Global general circulation of the ocean estimated by the ECCO-consortium. *Oceanography*, 22:88–103.

Youngs, M. K., Thompson, A. F., Lazar, A., and Richards, K. J. (2017). ACC Meanders, Energy Transfer, and Mixed BarotropicBaroclinic Instability. *Journal of Physical Oceanography*, 47:1291–1305.

Zhang, J. (2007). Increasing Antarctic sea ice under warming atmospheric and oceanic conditions. *Journal of Climate*, 20:2515–2529.